

UNIVERSITY COLLEGE LONDON

---

Faculty of Mathematics and Physical Sciences

Department of Physics & Astronomy

CORE-COLLAPSE SUPERNOVA  
DUST MASSES FROM  
LINE PROFILE MODELS

Thesis submitted for the Degree of Doctor of  
Philosophy of the University of London

by

ANTONIA BEVAN

Supervisors:

Prof. Michael J. Barlow  
Dr Jeremy A. Yates

Examiners:

Prof. Examiner 1  
Dr Examiner 2

---

September 16, 2015



I, Antonia Bevan, confirm that the work presented in this thesis is my own. Where information has been derived from other sources, I confirm that this has been indicated in the thesis.

## **Abstract**

---

FIRST PARAGRAPH MUST BE IN HERE.

OTHER PARAGRAPHS FOLLOW.

## Acknowledgements

---

FIRST PARAGRAPH MUST BE IN HERE.

OTHER PARAGRAPHS FOLLOW.

*Gather out of star-dust  
Earth-dust,  
Cloud-dust,  
Storm-dust,  
And splinters of hail,  
One handful of dream-dust  
Not for sale.*

- Langston Hughes

*Dream Dust*

# Contents

---

<b>Table of Contents</b>	<b>7</b>
<b>List of Figures</b>	<b>11</b>
<b>List of Tables</b>	<b>13</b>
<b>List of Acronyms</b>	<b>15</b>
<b>1 Introduction</b>	<b>17</b>
1.1 A Handful of Dust . . . . .	18
1.1.1 A Brief History . . . . .	18
1.1.2 The Roles of Dust in the Universe . . . . .	19
1.1.3 The Medium of Dust . . . . .	20
1.2 Core-Collapse Supernovae as Dust Factories . . . . .	21
1.2.1 Types of Supernovae . . . . .	21
1.2.2 From Massive Stars to Remnants . . . . .	22
1.2.3 Dust Formation in CCSNe . . . . .	23
1.2.4 The Three Signatures of Dust . . . . .	24
1.2.5 The Dust Mass Debate . . . . .	24
1.2.6 Motivation - call something else . . . . .	25
1.3 Dust-Affected Line Profiles . . . . .	26
1.3.1 Observing . . . . .	26
1.3.2 Previous Work on Line Profiles . . . . .	27
1.3.3 Modelling . . . . .	27
1.3.4 Mie Theory . . . . .	27

---

1.4 This Thesis . . . . .	27
<b>2 Details of the Monte Carlo Code</b>	<b>29</b>
2.1 Monte Carlo Methods . . . . .	29
2.2 Radiative Transfer and the Monte Carlo Method . . . . .	30
2.2.1 Energy Packets . . . . .	32
2.2.2 Initialisation and the Grid . . . . .	34
2.2.3 Properties of the Dusty Medium . . . . .	35
2.2.4 Emission and Propagation . . . . .	36
2.2.5 Doppler shifting . . . . .	39
2.2.6 Electron Scattering . . . . .	41
2.2.7 Doublets . . . . .	43
2.2.8 Comparing the Model with Observations . . . . .	44
2.3 The Structure of Damocles . . . . .	44
2.3.1 Computational Architecture and Processes . . . . .	45
2.3.2 OpenMP Parallelisation . . . . .	54
2.3.3 Input . . . . .	55
2.3.4 Output, Post-Processing and Visualisation . . . . .	62
2.4 Further Developments . . . . .	64
<b>3 Benchmarking and Testing</b>	<b>67</b>
3.1 Theoretical line profiles from first principles . . . . .	67
3.2 The line profile models of ? . . . . .	71
3.3 Testing the electron scattering mechanism . . . . .	71
3.4 Clumped models in smooth limits . . . . .	71
<b>4 Parameter Sensitivity</b>	<b>73</b>
4.1 The maximum line velocity, $V_{max}$ . . . . .	74
4.2 The ejecta radius ratio, $R_{in}/R_{out}$ . . . . .	74
4.3 The dust optical depth, $\tau$ . . . . .	75
4.3.1 The detached shell case . . . . .	75
4.3.2 The complete nebula case . . . . .	77
4.4 The dust albedo, $\omega$ . . . . .	77
4.5 The dust density profile, $\rho \propto r^{-2\beta}$ . . . . .	78

4.6	Inferring properties of the dust from the models . . . . .	81
4.7	Observable signatures of dust in line profiles . . . . .	81
4.8	The effect of a grain size distribution . . . . .	85
4.9	The effect of different species . . . . .	87
4.10	The velocity distribution . . . . .	88
<b>5</b>	<b>SN 1987A</b>	<b>89</b>
5.1	Spectral Observations of SN 1987A . . . . .	89
5.2	Modelling SN 1987A . . . . .	91
5.2.1	Smooth Density Models for SN 1987A . . . . .	94
5.2.2	Clumped Models for SN 1987A . . . . .	96
5.2.3	Grain size distributions and species conversions... . . . . .	98
5.2.4	Contamination of the the H $\alpha$ profiles at days 714 and 806 . . . . .	100
5.2.5	The red shoulder in the H $\alpha$ line profile at day 806 . . . . .	100
5.2.6	Potential challenges at later epochs: days 1862, 2875 and 3604 . . . . .	102
5.3	The evolution of dust formation in SN 1987A . . . . .	102
5.3.1	Dust masses from other line profile models . . . . .	103
5.3.2	Dust masses and properties from SED models . . . . .	104
<b>6</b>	<b>SN 2010jl and Other Supernovae</b>	<b>109</b>
<b>7</b>	<b>Conclusions and Future Work</b>	<b>111</b>
	<b>Bibliography</b>	<b>113</b>

This page was intentionally left blank

# List of Figures

---

1.1	The dark globule Barnard 68, LDN 57. ESO press release 30 April 1999. . .	19
1.2	A flowchart summarising the supernova classification scheme . . . . .	22
2.1	A flowchart representing the sequence of processes that take place in the Damocles code. The modules involved at each stage are given in parentheses.	33
2.2	3D representations of the grid generated by Damocles. A smooth distribution is shown on the left and a clumped distribution on the right. . . . .	36
2.3	A flowchart representing the hierarchy of modules and subroutines in the Damocles code. Ellipses represent modules and rectangles represent subroutines (the red rectangle is a recursive subroutine). Green arrows indicate the dependence on module or subroutine on previous modules or subroutines. Purple arrows indicate the flow of the code. . . . .	47
2.4	A flowchart representing the processes that occur in the <i>propagate</i> subroutine	52
2.5	Schematic representing which packets are collected when the line of sight environment is switched on. Packets that contribute to the emergent line profile are those that escape the nebula within a cone with vertical angle $\pi/6$ . . . . .	61
3.1	<i>Red:</i> Benchmark models for optically thin ( $\tau = 0$ ) line profiles with fractional velocity $v \propto r$ . Left to right: initial emissivity profiles $i(r) \propto r^{-2\beta}$ with $\beta = 0.0$ , $\beta = 1.0$ and $\beta = 2.0$ . Cases with $R_{in}/R_{out} = 0.2$ are on the top and $R_{in}/R_{out} = 0.0$ on the bottom. The presence of a plateau in the upper plots is due to the finite inner radius (detached shell). <i>Blue:</i> The analytical case with $i(u) \sim 1 - u^{2(1-\beta)}$ except in the case of $\beta = 1$ where $i(u) \sim -\log u$ . . . . .	68

---

3.2	Benchmark models for line profiles with $v \propto r$ , $i(r) \propto$ constant and a filled sphere with $R_{in}/R_{out} = 0$ . Pure dust absorption models ( $\omega = 0$ ) are presented in the top plot, whilst partially scattering models are presented at the bottom ( $\omega = 0.6$ ) as per ? Models II and III. All resulting profiles have been scaled to unity flux at their peaks. . . . .	69
4.1	Set of models with $i(r) \propto r^{-2\beta}$ for $\beta = 1.0$ (left), $\beta = 1.5$ (middle) or $\beta = 2.0$ (right), $\omega = 0$ , $R_{in}/R_{out} = 0.2$ , $v(r) \propto r$ and $v_{max} = 1$ illustrating the effects of varying $\tau$ . Peak fluxes are scaled to unity. . . . .	76
4.2	Set of models with $i(r) \propto r^{-4}$ (i.e. $\beta = 2.0$ ), $R_{in}/R_{out} = 0.2$ , $v(r) \propto r$ and $v_{max} = 1$ illustrating the effects of varying $\tau$ and $\omega$ . Peak fluxes are scaled to unity. . . . .	77
4.3	Variation of extinction efficiency ( $Q_{ext}$ ) with grain size for amorphous carbon and silicates using Mie theory at $\lambda = 658\mu\text{m}$ . Optical constants are from Zubko et al. (1996) and Draine & Lee (1984). A linear scale is presented on the top and a log scale on the bottom. . . . .	79
4.4	Variation of albedo with grain size for amorphous carbon and silicates using Mie theory at $\lambda = 658\mu\text{m}$ . Optical constants are from Zubko et al. (1996) and Draine & Lee (1984). A linear scale is presented on the top and a log scale on the bottom. . . . .	80
4.5	Model line profiles for H $\alpha$ (6563Å in red), H $\beta$ (4861Å in yellow) and Pa $\delta$ (10049Å in blue) for optically thin and optically thick cases on the left-hand side and right-hand side respectively. All models adopted density profile $\rho(r) \propto r^{-4}$ (i.e. $\beta = 2$ ), velocity profiles $v(r) \propto r$ and radii ratio $R_{in}/R_{out} = 0.2$ . The grain radii used were $a = 0.001 \mu\text{m}$ (top), $a = 0.1 \mu\text{m}$ (middle) and $a = 1.0 \mu\text{m}$ (bottom). All the above models used amorphous carbon. . . . .	82
4.6	The variation of amorphous carbon dust absorption efficiency with grain size. The grain radii plotted are $a = 0.001 \mu\text{m}$ (top), $a = 0.1 \mu\text{m}$ (middle) and $a = 1.0 \mu\text{m}$ (bottom). The vertical lines mark the wavelengths of H $\alpha$ (6563Å in red), H $\beta$ (4861Å in yellow) and Pa $\delta$ (10049Å in blue). . . . .	83

---

5.1	Conservative dust mass fit to the day 714 H $\alpha$ line of SN 1987A illustrating the underestimation of the red scattering wing for small grain sizes. Model parameters are the same as the conservative fit to day 714 except for the grain size distribution and dust mass: $V_{max} = 3250 \text{ km s}^{-1}$ , $R_{in}/R_{out}=0.25$ , $\beta = 1.2$ , $M_{dust} = 8.0 \times 10^{-6} M_{\odot}$ , $a_{min} = 0.005 \mu\text{m}$ , $a_{max} = 0.25 \mu\text{m}$ and $n(a) \propto a^{-3.5}$ . . . . .	91
5.2	Best smooth fit to the day 714 H $\alpha$ line (left) and [O I] $\lambda 6300, 6363 \text{ \AA}$ doublet (right) as per parameters detailed in Table 5.2. . . . .	92
5.3	Best smooth fit to the day 806 H $\alpha$ line (left) and the [O I] $\lambda 6300, 6363 \text{ \AA}$ doublet (right) as per parameters detailed in Table 5.2. . . . .	93
5.4	Best smooth fit to the H $\alpha$ line at days 1862, 2875 and 3604 as per parameters detailed in Table 5.2. . . . .	95
5.5	Best clumped fit to the day 714 H $\alpha$ line and [O I] $\lambda 6300, 6363 \text{ \AA}$ doublet as per parameters detailed in Table 5.3. . . . .	98
5.6	Best clumped fit to the day 806 H $\alpha$ line and [O I] $\lambda 6300, 6363 \text{ \AA}$ doublet as per parameters detailed in Table 5.3. . . . .	99
5.7	Best clumped fit to the H $\alpha$ line at days 1862, 2875 and 3604 as per parameters detailed in Table 5.3 with $a = 0.6 \mu\text{m}$ . . . . .	101
5.8	Best clumped fit to the H $\alpha$ line at days 1862, 2875 and 3604 as per parameters detailed in Table 5.4 with $a = 3.5 \mu\text{m}$ . . . . .	101
5.9	<i>Purple and yellow triangles</i> - Maximum ( $a = 3.5 \mu\text{m}$ ) and minimum ( $a = 0.6 \mu\text{m}$ ) dust masses respectively. Values are from the later epoch ( $t > 1862$ days) clumped models of H $\alpha$ . <i>Pink crosses</i> - Predicted dust masses (clumped models of the [O I] $\lambda 6300, 6363 \text{ \AA}$ doublet with grain size $a = 0.6 \mu\text{m}$ ). <i>Turquoise stars</i> - Predicted dust masses calculated as a log average of the maximum and minimum values. <i>Green</i> - Sigmoid fit to our predicted dust masses. <i>Blue</i> - dust masses derived by W15 in their photometric modelling of SN 1987A. <i>Red</i> - sigmoid fit to the W15 values. . . . .	105



## List of Tables

---

2.1	Values of $q_{H\alpha}(T)$ at three different temperatures as used by Damocles. . . . .	41
2.2	The input variables read in from the input file and example values . . . . .	55
2.3	List of all outputs and example values produced by the Damocles code. . . . .	63
4.1	Equivalent dust masses for the day 714 clumped models using grain size distributions and 100% amorphous carbon. $f$ is factor of increase from the dust mass for the single size model ( $M = 7 \times 10^{-5} M_\odot$ with $a = 0.6\mu\text{m}$ ) and $p$ is the exponent of the grain size distribution $n(a) \propto a^{-p}$ . . . . .	88
5.1	Details of the archival data for SN 1987A . . . . .	90
5.2	Details of the parameters used for the best fitting smooth models with grain radius $a = 0.35\mu\text{m}$ . . . . .	90
5.3	Details of the parameters used for the best fitting clumped models with $a = 0.6\mu\text{m}$ . . . . .	95
5.4	Details of the parameters used for the best fitting clumped models with $a = 3.5\mu\text{m}$ . . . . .	97
5.5	Equivalent dust masses for the day 714 clumped models using grain size distributions and 100% amorphous carbon. $f$ is factor of increase from the dust mass for the single size model ( $M = 7 \times 10^{-5} M_\odot$ with $a = 0.6\mu\text{m}$ ) and $p$ is the exponent of the grain size distribution $n(a) \propto a^{-p}$ . . . . .	100

## **List of Acronyms**

---

AAT - Anglo-Australian Telescope

API - Application Program Interface

CTIO - Cerro Tololo Inter-American Observatory

HST - Hubble Space Telescope

(M/N)IR - (Mid/Near) Infra-Red

ISM - Inter-Stellar Medium

SED - Spectral Energy Distribution

(CC)SN(e) - (Core-Collapse) Supernova(e)

UV - Ultra-Violet

VLT - Very Large Telescope

# Chapter 1

---

## Introduction

Should you choose to seek out one of my friends and ask them about my whereabouts in recent months, they would likely stare at you blankly. Upon further interrogation they would probably yield the information that I was preoccupied writing about dust, a fact which I imagine they find bemusing and possibly somewhat concerning. Blissful as they are in their ignorance of dust (astronomers find no such peace), they do not know the importance of this all-pervading substance.

The universe is an extremely dusty place. The ubiquity of dust throughout almost all epochs and environments demands a comprehensive understanding of its formation and evolution, properties and effects. It plays numerous roles in a variety of scenes; it is a building block of all solid bodies, a birthing place for molecules, a crucial ingredient in star formation and an extreme annoyance for cosmologists. It is both a product of physical processes and an agent of chemical ones.

It is perhaps confusing therefore that there is comparatively little consensus regarding the formation processes and natal environments that result in the evolution of certain atoms and molecules into the grains we call dust. Over the years since the first discovery of dust in the very early universe, a growing population of astronomers and astrophysicists have turned their attention to the study of dust formation in core-collapse supernovae (CCSNe), in the hope that these objects might prove to be the missing piece of the puzzle. Recent observations of a number of core-collapse supernovae and remnants have lent weight to this theory, with models and analyses of spectral energy distributions (SEDs) suggesting

---

the presence of large reservoirs of cool, ejecta-condensed dust.

I have sought to make my own small contribution to this field by exploiting a different observational signature, that of blue-shifted line asymmetries observed in the spectra of many CCSNe and attributed to the formation of dust in the ejecta. By quantitatively modelling characteristically asymmetric spectral line profiles using a novel code, DAMOCLES, I have attempted to determine the rate of dust formation in CCSNe and the expected order of magnitude of the eventual dust masses produced.

Throughout the remainder of this chapter I will attempt to elucidate the above synopsis in more detail. A brief discussion of the roles that dust plays in the universe will be followed by a summary of our current understanding of dust formation in CCSNe. I will conclude this chapter with a short justification of the approach that I have adopted for this work and an outline of the structure of this thesis.

## 1.1 A Handful of Dust

### 1.1.1 A Brief History

The presence of dust in the universe was first theorised when astronomers observed dark patches of sky in the Milky Way where all of the stars had been “erased” (see Figure 1.1). Whilst some claimed that these black regions were in fact a true absence of stars resulting from some anomaly in the stellar distribution, others felt that it was more likely that an obscuring cloud of material was blocking the light from the stars behind. In 1930, Donald Trumpler confirmed this latter theory by considering the apparent magnitudes and colours of stars located at different angles to the galactic plane, discovering that those closer to the plane appeared redder than their more distant counterparts. This was the first evidence of interstellar reddening and the beginnings of our understanding of dust as a scatterer, absorber and emitter of radiation.

For the next few decades, dust was thought to be largely an irritating obstacle to observing and comprehending more interesting facets of the universe. We now have a much fuller understanding of the variety and importance of the roles that dust plays throughout astrophysics.

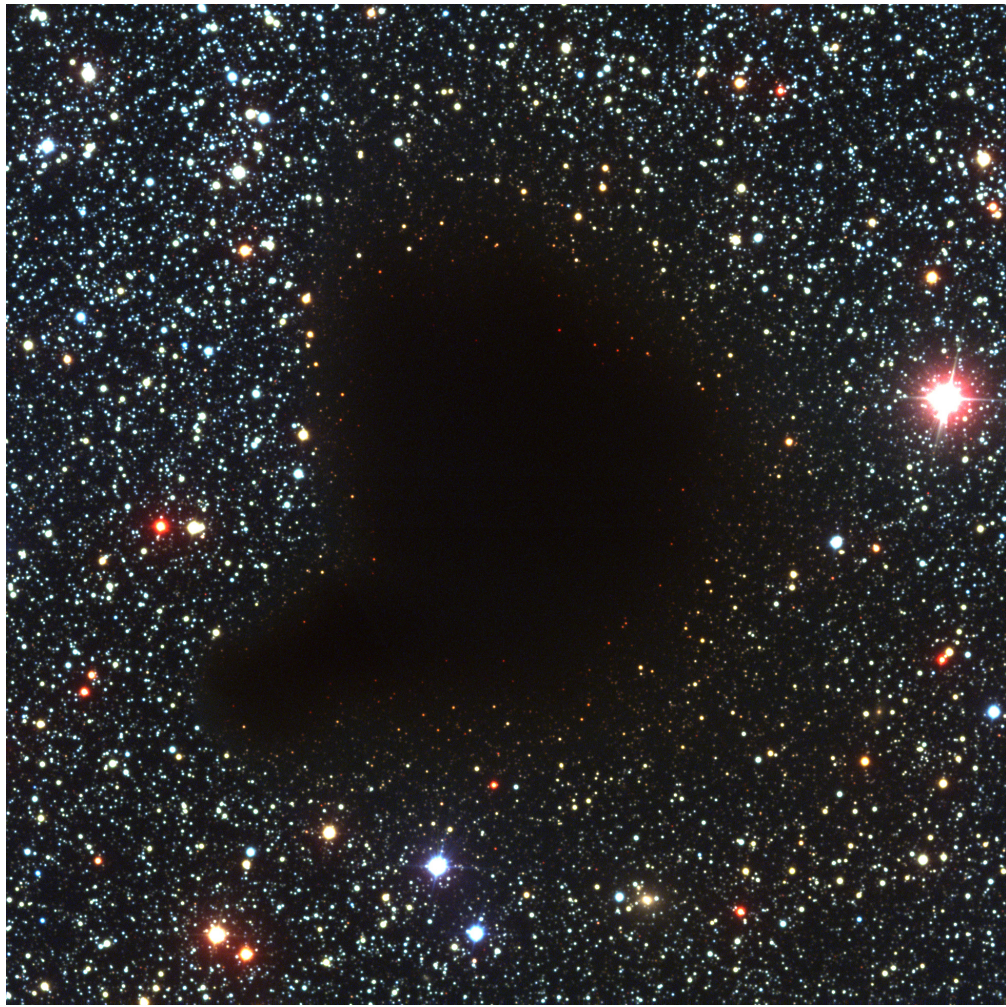


**Figure 1.1.** The dark globule Barnard 68, LDN 57. ESO press release 30 April 1999.

### 1.1.2 The Roles of Dust in the Universe

Despite comprising only  $\sim 1\%$  of the mass of the interstellar medium (ISM), dust grains account for as much as 30% of the total galactic luminosity via their emission in the infrared (IR) (Li & Greenberg 2003). In the cycle of matter from the ISM to condensing clouds to stars and back again, dust is far more than a passive passenger along for the ride. Whilst residing in the ISM, dust is important in determining its thermodynamics. It acts both as a heating agent via the emission of photoelectrons in regions of strong ultra-violet (UV) radiation and a coolant in dense regions via the emission of IR radiation. In this role as a coolant, dust is also crucial to the process of star-formation, helping to remove gravitational energy and allowing the natal cloud to collapse. Dust also contributes to the star formation process by shielding the gas from ionising radiation, helping to speed up

the construction of the protostellar core.

In addition to the above physical functions, dust plays an essential part in chemical processes. Heavy elements in the local medium are depleted through their inclusion in dust grains. These grains attract gaseous atoms to their surfaces and catalyse the formation of molecules which are then released back into the surrounding medium.

Dust does not reside solely in the ISM however. It is present in large quantities in the circumnuclear tori found around active galactic nuclei. Dust is also found between planets, around stars and in protoplanetary discs, where dust grains are often the smallest unit of the building blocks that will go on to form planetesimals and planets. These grains may even be responsible for the origins of life.

The more detailed our understanding of dust as an astrophysical community, the more accurate we can make our inferences across an entire range of fields. There is arguably no other topic that has such wide-ranging effects.

### 1.1.3 The Medium of Dust

An increasingly detailed knowledge of the nature and properties of dust has developed over the last few decades. Dust grains have their terrestrial analogue in soot or very fine sand rather than in the dust bunnies that one may find behind the sofa. When found in the ISM they are generally small, between  $0.05\mu\text{m}$  and  $0.25\mu\text{m}$  in radius, and are normally predominantly composed of carbon or silicates. Carbonaceous grains may take many forms ranging from structured solids such as diamond and graphite to amorphous molecules and aromatics. They are generally found to be strongly attenuating. Silicates tend to be more glassy and contain silicon and oxygen potentially with the dirtying addition of magnesium, iron or other heavier elements. Condensates of more complex molecules such as olivine ( $\text{MgFeSiO}_4$ ) and pyroxene ( $\text{MgSiO}_3$ ) make up these grains.

Whilst an increasingly strong picture of the composition and properties of dust is becoming apparent, there are still a number of largely unresolved issues regarding the early stages of the life cycle of dust grains. Dust grains in the ISM are found to follow a grain radius distribution  $n(a) \propto a^{-3.5}$  as described by Mathis, Rumpl & Nordsieck in 1977. After their formation, however, grains are subject to numerous forces that can result in their destruction, sputtering or evaporation that mean that the grain radius distribution of newly-formed dust is not necessarily that observed in the ISM. The grain size distribution and relative abundances of species of newly-formed grains are still topics in dispute and

are issues that I attempt to address in my models.

## 1.2 Core-Collapse Supernovae as Dust Factories

In an effort to explicate the motivations behind studying dust, I have so far mostly limited my discussion to the evolution and properties of dust after the initial stages of its formation once it has entered the ISM. The most current and contentious debate, however, is over the natal environment of dust grains.

Supernovae are the violent explosions that are the death of stars. They evolve very quickly and create extreme conditions. Focus on supernovae as a possible source of dust in the universe has been motivated by the physical conditions that they produce shortly after their outbreak and by the presence of large quantities of heavy elements that constitute the integrant ingredients of dust grains.

### 1.2.1 Types of Supernovae

Supernovae may be classified into a number of different types depending on the properties of their light curves and optical spectra. They are bisected initially into Types I and II according respectively to the absence or presence of hydrogen in their spectra. Further sub-classifications depend on the evolution of the supernova's light curve after maximum light and the features in its spectrum. A summary of the supernova classification scheme is presented in Figure 1.2.

The initial classification of Type I or Type II is based on very early spectra, as are all further classifications of Type I supernovae. Type II supernovae are more complex in their categorisation. The further subdivisions of the Type II supernovae depend on the dominance of hydrogen or helium in later spectra, with helium dominant supernovae being classified as Type IIn. The classification of Type II supernovae that exhibit strong hydrogen lines is then dependent on the evolution of the light curve after maximum light, with a linearly decaying light curve being classified as Type IIL and a plateauing light curve classifying the supernova as Type IIP. Type IIn supernovae are omitted from the summary presented in Figure 1.2 as they cannot be classified straightforwardly via a bifurcating process. Type IIn supernovae will generally have strong emission lines, particularly hydrogen lines, often with complex profiles. Crucially, the spectra of Type IIn supernovae do not exhibit the broad absorption features frequently seen in other types and instead

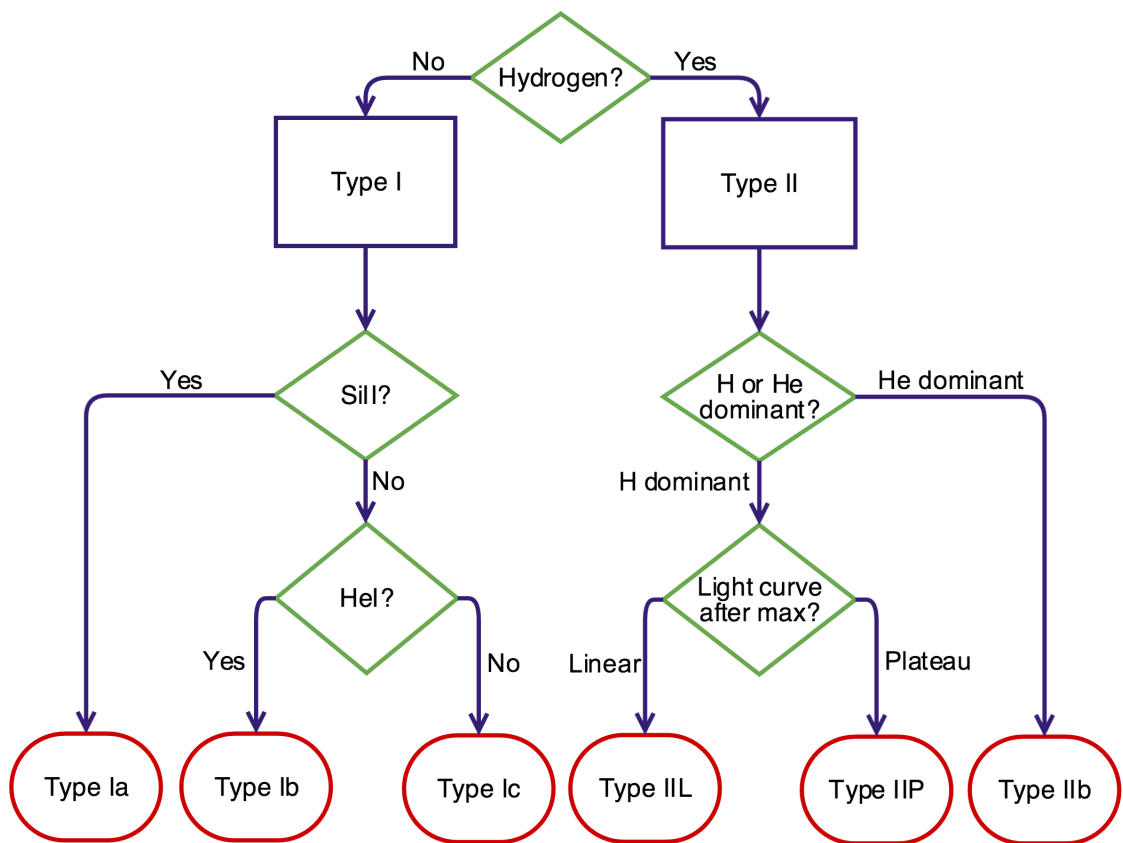


**Figure 1.2.** A flowchart summarising the supernova classification scheme

contain narrow lines (hence Type IIn).

### 1.2.2 From Massive Stars to Remnants

It is generally accepted that the progenitors of Type Ia supernovae are white dwarfs that exist in a binary system with another star. The accretion of material from one star to another results in a thermonuclear explosion. This explosion mechanism is unique to Type Ia supernovae with Type Ib/c and Type II supernovae thought to explode via the core-collapse mechanism. Broadly, this process is initiated when the massive star ( $\geq 8M_{\odot}$ ) starts to fuse heavier elements. The fusion of ever heavier elements generates less and less energy whilst also causing the mass of the core to increase. Eventually, radiation pressure drops sufficiently that the core can no longer support itself against its own self-gravity and begins to collapse rapidly. Within milliseconds, the core reaches extremely high densities and, when it can no longer condense further, “bounces” off itself causing both an immense shockwave to propagate outwards and a vast quantity of energy to be released

via the expulsion of neutrinos. Much of this complex process is still poorly understood and interesting work is currently being done modelling these very early stages. Though the explosion mechanisms of CCSNe are largely beyond the scope of my work, some attention will be paid to these models later in this thesis since instabilities that arise in these early stages can influence the structure of the ejecta at later stages of its evolution.

For several hundred years after the explosion, the supernova (now a remnant) is in the free-expansion phase. During this phase, the mass and velocity of the expanding supernova massively exceed those of the surrounding medium and the behaviour of the remnant may be analysed as if it were expanding into a vacuum. The shock radius during this phase may be simply calculated as  $R_s = v_s t$ . As the shockwave propagates through the ISM, interstellar material that has been compressed by the forward shock begins to accumulate. At the same time a reverse shock wave begins to propagate back through the ejecta. It is during this phase, which arises very soon after the initial explosion and lasts for a few hundred years, that the physical conditions in the ejecta are thought to be optimal for dust formation.

### 1.2.3 Dust Formation in CCSNe

Superficially, the formation of dust grains requires densities high enough for interaction between particles to take place, but temperatures that are cool enough to allow the grains to survive. The theory that the ejecta of a CCSN in its free-expansion phase could provide these conditions was first hypothesised by Cernuschi, Marsicano & Codina in 1967 and they have now long been thought to be potential dust factories (Hoyle & Wickramasinghe 1970; Kozasa, Hasegawa & Nomoto 1991; Todini & Ferrara 2001).

The formation of dust was originally thought to result from the stochastic process of classical nucleation whereby particles coalesce to form the seeds of dust grains. These seeds become the nucleation sites from which grains are ultimately born through the aggregation of further particles. Various models of dust formation in the ejecta of CCSNe have used this approach (Kozasa, Hasegawa & Nomoto 1989; Todini & Ferrara 2001; Nozawa et al. 2003; Schneider, Ferrara & Salvaterra 2004).

More recently, several models of dust formation in CCSNe that consider the effects of chemistry on the growth of dust grains have been published. These models consider the chemical composition of the gas and include chemical reaction rates thereby considering the manner in which molecular evolution influences dust grain formation and growth rates

(Cherchneff & Dwek 2009, 2010; Sarangi & Cherchneff 2013; Sarangi & Cherchneff 2015).

Models using both methods have predicted dust masses of the order of  $0.1\text{-}1 M_{\odot}$  of dust forming within the ejecta of CCSNe of progenitor masses between  $12\text{-}40 M_{\odot}$  within the first few years after the initial explosion.

### **1.2.4 The Three Signatures of Dust**

The presence of dust in the ejecta of CCSNe can be indicated by three main signatures:

#### **A decrease in the light curve**

As the dust begins to form in the ejecta, UV and optical light is absorbed by the dust causing a decrease in the light curve at these wavelengths.

#### **Excess IR emission**

An increase in emission in the IR occurs contemporaneously with the decrease in the UV-optical light curve. A thermal MIR excess is caused by warm dust and an excess in the far-IR and sub-mm is the result of cold dust. The increase in emission in these wavelength can be caused by newly-formed dust condensing in the ejecta but can also be a result of the illumination of pre-existing dust

#### **Blue-shifted line profiles**

Finally, the onset of the formation of dust can cause an asymmetry in line profiles in the optical and IR. The absorption and scattering of optical or near-IR radiation by newly-formed dust within the ejecta can result in an asymmetry between the red and blue shifted components, with redwards emission from the far side of the ejecta undergoing greater absorption and resulting an overall shift of the profile to the blue.

All three of these signatures have been discussed in detail over the timeline of this subject but the focus has been on using the excess IR emission seen in the SED of CCSNe to determine quantitatively dust masses in these objects. This approach has resulted in a lively debate regarding the quantities of dust that CCSNe are capable of producing.

### 1.2.5 The Dust Mass Debate

Over the past two decades, several high redshift galaxies have been found to contain significant masses of dust (Omont et al. 2001; Bertoldi et al. 2003; Watson et al. 2015). CCSNe are one of the few potential sources that could contribute large quantities of dust at early epochs. However, observations over the last decade at mid-infrared (MIR) wavelengths of warm dust emission from CCSNe has suggested that the quantities of ejecta-condensed dust produced during the first 1000 days were typically  $\leq 10^{-3} M_{\odot}$  (Sugerman et al. 2006; Meikle et al. 2007; Kotak et al. 2009; Andrews et al. 2010; Fabbri et al. 2011). This is much less than the 0.1-1.0  $M_{\odot}$  of dust per CCSN estimated to be needed in order to account for the masses observed (Morgan & Edmunds 2003; Dwek, Galliano & Jones 2007). These observations would indicate that other early-time sources of dust must be found.

However, recent *Herschel* far-IR and sub-mm observations of several young supernova remnants have revealed cold dust masses as high as  $0.2\text{--}0.8 M_{\odot}$ , resulting in a re-evaluation of the rate of dust production by CCSNe and a renewed focus on these objects as sources of dust (Barlow et al. 2010; Matsuura et al. 2011; Gomez et al. 2012).

#### SN 1987A

Critical to this field has been the study of SN 1987A. This supernova is one of the most studied objects in the history of astronomy and has been observed almost continuously since it exploded 28 years ago. The reason for this is its proximity. At only Xpc away, it has allowed for some exceptionally well-resolved spectral and photometric observations. Neutrinos from its explosion were even detected by scientists at Y. As such, it has yielded results and insight that would not have been possible otherwise and is a key to understanding the formation and evolution of dust in CCSNe.

It is of no surprise therefore that this object has been central to the debate. Lucy et al. (1989) was the first to suggest the presence of dust in SN 1987A. *Herschel* observations of SN 1987A were the first to suggest the presence of cold dust in any supernova.

### 1.2.6 Motivation - call something else

It is seems increasingly likely that CCSNe do indeed produce significant quantities of dust. However, there remain a large number of outstanding challenges to consider. Firstly, there

are still only a very small number of supernovae that have been observed to have sizeable masses of dust present in their ejecta. If further CCSNe were also shown to have formed large quantities of dust then the already shifting opinion might start to become consensus. Other points to consider regarding dust formation and evolution in CCSNe include the nature of the dust (composition, grain size, grain shape etc.) which is still largely unclear, as is the extent to which it is destroyed or sputtered after its initial formation. Related to this is the uncertainty of the dust formation rate in the ejecta and the issue of where this formation takes place. These are all interesting questions that call out for answers.

The *Hershel* dust mass estimates were based on fitting dust SEDs that peaked at far-IR wavelengths. Unfortunately, following the end of the *Herschel* mission in 2013, there is likely to be a long wait for far-IR facilities with comparable or better sensitivities than *Herschel* to become available. Without data, this methodology is temporarily ineffectual. This provided an incentive to make use of alternative methods to estimate the dust masses that form in supernova ejecta.

## 1.3 Dust-Affected Line Profiles

The purpose of my work has been to develop a new approach to determining dust masses in supernovae, with the aim of providing an alternative to SED fitting for the future and of providing corroborating or contradicting evidence of past results. I looked to exploit the third signature of dust formation in supernovae, namely the red-clue line asymmetry observed in optical and IR line profiles. Though this feature has been discussed at length by numerous authors (REFERENCES) it has very rarely been quantitatively measured or modelled.

I have sought to construct a Monte Carlo based code that numerically models this feature in the spectra of SNe in order to quantitatively determine dust masses formed at a variety of epochs post-explosion, additionally seeking to place constraints of the composition and grain size distributions of the newly-formed dust.

### 1.3.1 Observing

Numerous telescopes have recorded spectra of CCSNe in the optical and IR, some with extremely high resolution. The Anglo-Australian Telescope (AAT), the Cerro Tololo Inter-American Observatory (CTIO), the Hubble Space Telescope (HST) and the Very Large

Telescope (VLT) have all observed several supernovae in the optical including SN 1987A. Other telescopes such as the two Gemini Multi-Object Spectrographs (GMOS) have also taken spectra of numerous CCSNe.

Advances in digital storage have allowed for spectral and photometric observations to be made easily available online. Many observatories now publish their recent observations online in archives and are working to upload observations that pre-date file sharing services. Much of the data used in this thesis was obtained from these archives.

### 1.3.2 Previous Work on Line Profiles

LUCY LUCY LUCY!!! Also some of the other stuff - gerasimovic, some of the other theoretical papers, maybe also the electron scattering stuff

EXAMPLES OF RBLA WORK

### 1.3.3 Modelling

Need to think about what i actually need to consider in this section.

- dust absorption, scattering and reemission in the IR - radiative transfer and independence of optical properties and temp meaning do not need to fully solve rad tran problem
- mie theory deets? how is it solved and what is the theory? - assumptions of isotropy? scattering matrices?

### 1.3.4 Mie Theory

In order to truly understand observations that are a product of dust, we must first understand those facets of a dusty medium that determine its interaction with incident radiation. Dust grain radii are often of a similar order of magnitude to the wavelength of that incident radiation and so may be analysed from an optical perspective using Mie Theory. Mie Theory is a mathematical solution to Maxwell's equation that describe how light is scattered off a small particle. In combination with the optical properties of the medium, this allows for a precise determination of the extinction and scattering efficiencies of a given environment. Conveniently, this allows for the straightforward modelling of a dusty medium and it is this calculation that I exploit in my models. Mie Theory assumes particles to be spherical, an assumption which is a potential issue since grains may be crystalline, fluffy or extremely amorphous. This issue is addressed later in this thesis.

## **1.4 This Thesis**

And relate to your current work - give an overview of the work and what you did as well as the structure of the thesis - see Jo's for example.

# Chapter 2

---

## Details of the Monte Carlo Code

### 2.1 Monte Carlo Methods

The name 'Monte Carlo' describes a class of modelling techniques that employ a stochastic approach to simulating mathematical and physical situations that are otherwise difficult or impossible to solve. By repeatedly sampling random numbers from a probability distribution, numerical results to non-analytic problems may be obtained. The approach was first used by researchers at Los Alamos in the late 1940s who adopted the method to model the transport of neutrons. It is from the code name for this project, 'Monte Carlo', that the methods derive their name.

As the available computing power increased over the following decades, Monte Carlo methods became more and more useful as a means of solving complex problems and are now used widely across numerous fields including mathematics, statistics, engineering, finance, the physical sciences and many others. The nature of the approach means that they are particularly well-suited to problems with multiple degrees of freedom, and especially when any of these degrees are coupled. By using random numbers to represent quantities that parametrise a physical problem, a model may be generated that simulates a solution to the problem using a pseudo-random number generator. It must be the case that the quantities that characterize the problem may be represented by a continuous distribution in the range  $[0,1]$  in order that randomly generated numbers may be translated into physical properties.

For each randomly-generated input, the model of interest is applied and an output -

a 'possible outcome' - is obtained. By iterating this process many times with randomly-generated inputs each time, many possible outcomes are generated and a probability distribution may be built up. The interpretation of the outputted probability distribution is dependent on the manner of utilisation of the Monte Carlo method. For example, the iterative procedure may be used to determine best-fitting parameters of a model or may be used to find the mean-free path of a photon. In the former case, the multi-dimensional probability distribution may be analysed to determine the most representative model or models whereas in the latter case the probability distribution is equivalent to an energy distribution.

Clearly, Monte Carlo simulations are limited by their finite nature and will never produce a perfect solution. However, this does not mean that Monte Carlo simulations are lacking in rigour. It may be shown that the error in a Monte Carlo model is approximately  $\sim \frac{1}{\sqrt{n}}$  for large  $n$ , where  $n$  is the number of quanta used in the simulation. The error may therefore be made as small as required by increasing the number of quanta used in the simulation subject to the restrictions of computing time and expense.

In the next section, I discuss the use of Monte Carlo methods as applied to radiative transfer problems and specifically to DAMOCLES. I discuss the computational aspects of my work and the architecture of the code in section 2.3 before finally discussing the limitations of the code and its potential for future developments in section 2.4.

## **2.2 Radiative Transfer and the Monte Carlo Method**

The application of Monte Carlo codes to radiative transfer problems in astrophysics has a strong history. Numerous codes that utilise this stochastic methodology have been written in the past few decades in order to model the transport of photon packets through various media. The energy to be transported throughout the region of interest is discretised into packets and the path of each packet is calculated according to the properties of the environments that it passes through during its lifetime. Collating the escaped packets at the end of the simulation produces an energy distribution.

There exist several Monte Carlo radiative transfer codes that use this technique in order to model the transfer of line emission through a nebula to produce a synthetic spectrum. There also exist a number of codes that treat the continuous emission and absorption of energy in dusty environments in order to produce and fit a spectral energy

---

distribution (SED). Models of supernovae have been produced using both approaches and well-fitting spectra and SEDs have been generated but never, according to the best of my knowledge, has the mechanism been employed to produce sophisticated models of line profiles in expanding dusty regions. In this new code, we seek to apply the technique to an expanding dusty medium in order to consider the effects on a single emitted line profile.

Previous work by Leon Lucy has considered the problem of dust-induced asymmetric line profiles in the ejecta of supernovae and he has published results derived both analytically and using simple Monte Carlo simulations. These simulations appear to be the only published instances of a numerical approach to studying this spectral feature. The DAMOCLES code adopts the same technique as the original modelling by Leon Lucy but allows for a considerably more complex treatment of the composition, geometry and motion of the dusty medium.

Radiative transfer methods as applied to supernovae generally treat a wide wavelength range and seek to conserve the total energy. In the case of SED modelling, this is often achieved by dividing the total energy into packets of equal weight and energy, and iteratively determining the temperature and ionization structure. In this work, the approach we adopt is somewhat simpler as only a very narrow wavelength range need be considered. Rather than seeking to conserve the total energy, we assume that any packet absorbed by dust would be re-emitted outside the wavelength range of interest and thus no longer contributes to the resulting line profile. Any absorbed packet is therefore removed from circulation. In addition to this, the absorption and scattering of radiation by dust is independent of temperature and there is therefore no need to calculate temperatures throughout the nebula. Similarly, in the case of radiative modelling of synthetic spectra of the ejecta of supernovae, approximations such as the Sobolev approximation are often employed to handle the blending of lines more efficiently. This is unnecessary here as only a single line or doublet is ever treated and a comparatively narrow wavelength range considered.

The subtleties of the problem we consider here lie in the treatment of an atmosphere expanding as fast as 10% of the speed of light. Lorentz transforms must be carefully applied in order that packets experience the appropriate degree of frequency shifting at emission and at each subsequent scattering event. In this respect, the code is analogous to Monte Carlo radiative transfer models of electron scattering published by ???. Indeed, similar features are observed in the outputs of both.

Throughout this section, I will describe the principles, assumptions and techniques adopted in the production of DAMOCLES (see Figure 2.1) before I move on to address the mechanics and architecture of the code itself. Damocles stands for **D**ust-**A**ffected **M**odels **O**f **C**haracteristic **L**ine **E**mission in **S**upernovae.

### 2.2.1 Energy Packets

The fundamental principle underlying the transport of radiation throughout a dusty nebula is that the radiation be discretised into packets. Each of these packets is then propagated throughout the nebula and ultimately contributes a fraction of the final energy distribution. At the start of the simulation, each packet is assumed to consist of  $n$  photons of frequency  $\nu_0$ , the rest frequency of the line to be modelled. All packets therefore begin life with initial energy

$$E_0 = nh\nu_0 \quad (2.1)$$

where  $h$  is Planck's constant. As the packets move through the ejecta, they are scattered off high-velocity dust grains and after each scattering event, the frequency of the packet is altered. In Monte Carlo simulations that model non-moving atmospheres, packets are usually taken to be of constant energy. When the frequency of a packet is altered after an event, the energy of that packet is kept constant and the number of real photons contained within it assumed to change. However, in the case of dust scattering, the number of real photons is conserved and thus the energy of the packet is altered. This is most easily achieved by weighting each packet over all scattering events as

$$w = \prod_{scat} \frac{\nu'}{\nu} \quad (2.2)$$

where  $w$  is the weight of the packet. The final energy of each packet is then  $E = wE_0$ , where  $E_0$  is the initial energy of the packet. The final dust-affected line profile is compiled by adding the total energy of all packets in a specific frequency bin in order to produce a histogram.

In these models, unlike fully self-consistent SED radiative transfer models, there is

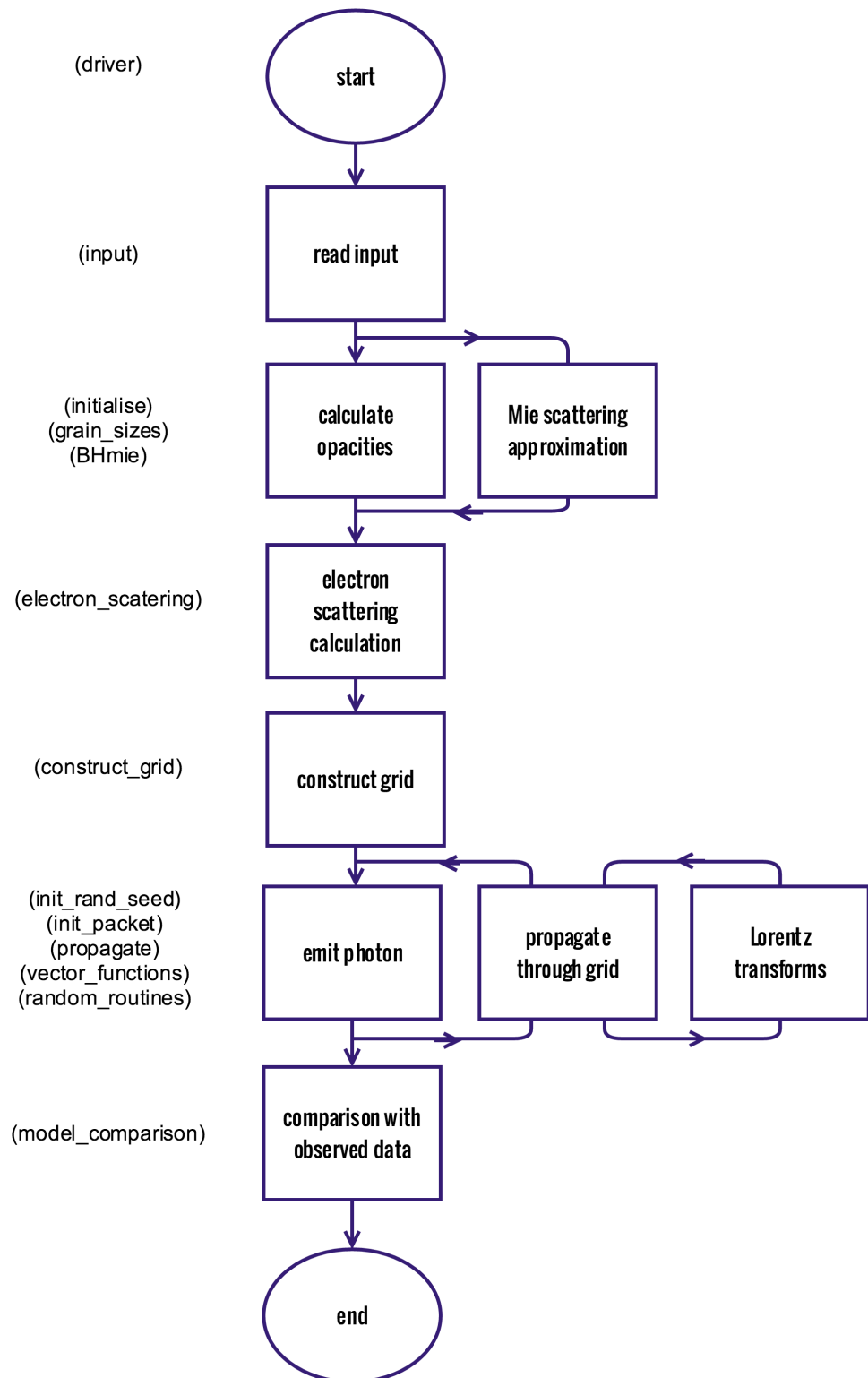


**Figure 2.1.** A flowchart representing the sequence of processes that take place in the Damocles code. The modules involved at each stage are given in parentheses.

no requirement that the total energy be conserved. We drop this traditional requirement since radiation that is absorbed by dust is re-emitted outside of the wavelength range of interest and thus no longer contributes any flux to the resulting line profile. Packets that are absorbed may be safely removed from the simulation.

### 2.2.2 Initialisation and the Grid

The supernova ejecta is approximated by a three-dimensional cartesian grid, each cell of which is assumed to have uniform density and composition. By default, the ejecta occupies a shell between inner radius  $R_{in}$  and outer radius  $R_{out}$ . The grid extends from  $-R_{out}$  to  $+R_{out}$  in each of the three axes. Each side is split into the same number of divisions and thus each cell is a cube of volume  $R_{out}^3/n_{div}^3$  where  $n_{div}$  is the number of divisions along each axis and is specified by the user. For the remainder of this thesis, a spherically symmetric situation is assumed and in all modelling and testing the grid is constructed in this manner. However, there are no assumptions of symmetry in the code and a cartesian grid was adopted in order to allow for arbitrary geometries to be modelled in the future e.g. ellipsoidal or toroidal ejecta distributions.

Both gas and dust are by default assumed to have a power-law distribution declared as  $\rho(r) \propto r^{-\beta}$  between  $R_{in}$  and  $R_{out}$ . The distribution of gas determines the emissivity distribution and thus the starting positions of the packets in the simulation (see section 2.2.4). However, after the initial emission of energy packets, the gas plays no further role in the simulation as only interactions with dust grains are of interest here. By default, the dust is coupled to the gas and thus follows the same smooth power-law distribution previously described with exponent  $-\beta$ . The dust density in each cell is therefore calculated as

$$\rho(r) = \frac{M_{tot}(3 - \beta)}{4\pi(R_{out}^{3-\beta} - R_{in}^{3-\beta})} \quad (2.3)$$

where  $r$  is the radial distance from the centre of the cell to the origin and  $M_{tot}$  is the total desired dust mass to model. Any cell whose centre falls outside of the bounds of the supernova ejecta has dust density set to zero. If the dust and gas are decoupled then the user must specify distinct profiles for the gas and the dust; that is, separate power laws must be declared and independent inner and outer radii specified. This allows for

more sophisticated modelling of, for example, circumstellar shells or dense cores of dust formation surrounded by more diffuse gas.

It is known from SED modelling that clumped environments produce very different results to environments assumed to have a smooth distribution of dust and gas. Generally, in comparison to smooth models, clumped models tend to require more dust in order to reproduce a similar level of emission or absorption. The capacity for modelling a clumped dusty medium is therefore included in the code. The fraction of the dust mass that is in clumps is declared ( $m_{frac}$ ) and the total volume filling factor of the clumps ( $f$ ) is also specified. Dust that is not located in clumps is distributed according to a smooth radial profile. The clumps occupy a single grid cell and their size can therefore be varied by altering the number of divisions in the grid. They are distributed stochastically with probability of a given cell being a clump proportional to the smooth density profile (i.e.  $p(r) \propto r^{-\beta}$ ). The density of all clumps is constant and is calculated as

$$\rho_{clump} = \frac{M_{clumps}}{V_{clumps}} = \frac{m_{frac} M_{tot}}{\frac{4}{3} f \pi (R_{out}^3 - R_{in}^3)} \quad (2.4)$$

where  $M_{tot}$  is the total dust mass,  $M_{clumps}$  is the total dust mass in clumps and  $V_{clumps}$  is the total volume occupied by clumps.  $m_{frac}$  and  $f$  are defined as above.

A grid of cubic cells of varying dust and gas densities is thus produced in readiness for packets to be transported through it. Examples of a smooth and clumped distributions of dust generated by Damocles are presented in Figure 2.2. A frequency grid is also established centred on the rest-frame frequency of the line to be modelled.

### 2.2.3 Properties of the Dusty Medium

Dust of any composition may be used for which optical data is available. The relative abundances of the species must be declared in an input file accompanied by a grain size distribution for each species. Files detailing the optical data ( $n$  and  $\kappa$  values) for the chosen dust species are also declared at the start of the code. For each frequency and grain size pair, a Mie scattering routine is employed to calculate the  $Q_{abs}(\nu)$  and  $Q_{sca}(\nu)$  values from the components of the refractive index  $n + i\kappa$  for every combination of wavelength, grain size and species. By summing over the weighted grain sizes and species, overall extinction values are calculated. These values are then used in the calculation of the opacity of each

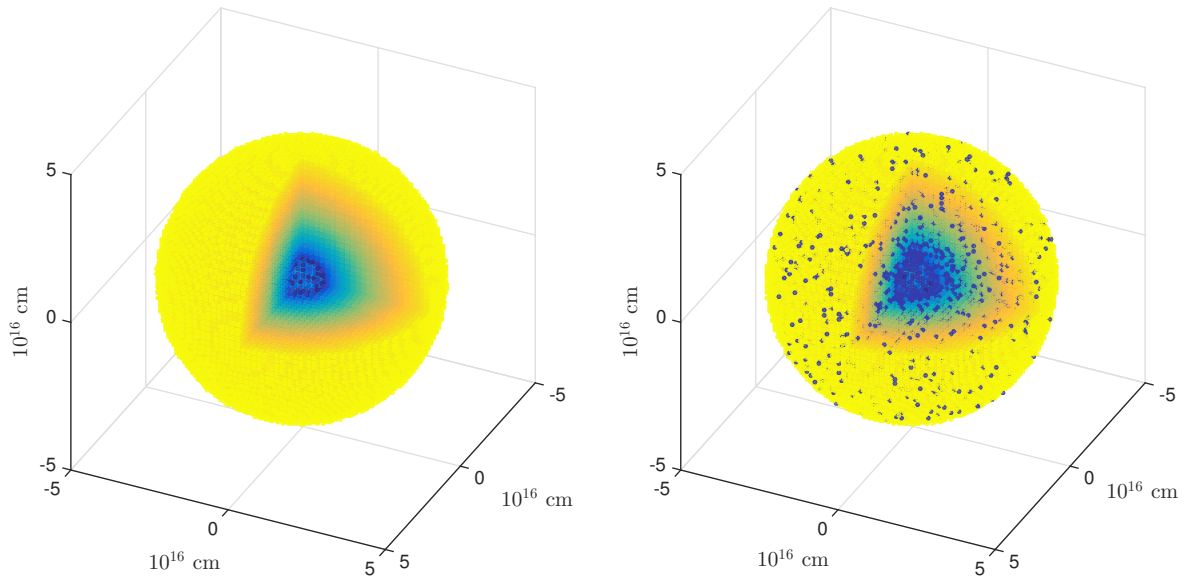


**Figure 2.2.** 3D representations of the grid generated by Damocles. A smooth distribution is shown on the left and a clumped distribution on the right.

grid cell, which determines the fate of any packets passing through it.

The Mie solution to Maxwell's equations may be approximated under certain conditions to allow for a computationally simple calculation of extinction, scattering and absorption efficiencies. In particular, this approximation is appropriate in the regime where the wavelength of the incident radiation is of a similar order of magnitude to the diameter of a spherical scatterer. It is therefore a helpful and suitable approximation to employ in Damocles where we assume dust grains to be approximately spherical and of the order of  $\sim 0.1\mu\text{m}$  in radius. Further understanding of the properties of newly-formed dust in the ejecta of supernovae might be obtained by considering alternative approximations for these calculations in future, for example by considering a continuous distribution of ellipsoids in preference to solely spherical grains.

#### 2.2.4 Emission and Propagation

The initial radiation field is inherently tied to the distribution of gas throughout the supernova ejecta. The relationship between the emissivity and the gas density may vary under different regimes and therefore the emissivity distribution is also specified as a power law with  $i(\rho) \propto \rho^k$ . In general, however, this is taken to be  $i(r) \propto r^{-2\beta}$  since the majority of lines modelled are recombination lines and therefore  $i(\rho) \propto \rho^2$ . The

supernova ejecta is divided into shells between  $R_{in}$  and  $R_{out}$  and the number of packets to be emitted in each shell calculated according to the specified distributions. For each packet a location within the appropriate shell is determined by randomly sampling from an isotropic distribution. Three random numbers in the range [0,1) are sampled and these are translated into spherical coordinates as

$$\phi = 2\pi\eta \quad (2.5)$$

$$\theta = \arccos(2\xi - 1) \quad (2.6)$$

$$r = R_i + \zeta(R_{i+1} - R_i) \quad (2.7)$$

where  $\eta$ ,  $\xi$  and  $\zeta$  are random numbers,  $\phi$  is the azimuthal angle,  $\cos \theta$  is the radial direction cosine and  $R_i$  is the inner boundary of the  $i^{\text{th}}$  shell. At emission and at every subsequent scattering event, the packet is propelled with a new direction vector which is sample from an isotropic distribution. I do not include forward-scattering matrices in the code since the effects of forward scattering by dust are so small as to be negligible and it is simpler and more efficient simply to assume isotropic scattering. Having calculated an emission location, an initial propagation direction vector  $(\theta, \phi)$  must be obtained. This is calculated in exactly the same manner as described in equation 2.7 but for two newly generated random numbers.

Once a packet has been emitted into the nebula, it must be propagated through the grid until it escapes the outer bound of the ejecta  $R_{out}$ . If it is not absorbed, its trajectory must be calculated and its weighting updated as it undergoes repeated scatterings. In each cell that a packet passes through, a test is performed to determine whether the packet passes through that cell and into the next or whether it experiences an event, either scattering or absorption. I calculate this by considering the probability that the packet travels a distance  $l$  without interacting as

$$p(l) = e^{-n\sigma_\nu l} = e^{-\tau_\nu} \quad (2.8)$$

where  $n$  is the number density,  $\sigma_\nu$  is the cross-section of interaction at frequency  $\nu$  and

$$\tau_\nu = n\sigma_\nu l = \rho\kappa_\nu l \quad (2.9)$$

for constant  $n$  and  $\sigma_\nu$  (as in a grid cell). The probability that a packet *does* interact within a distance  $l$  is therefore  $1 - e^{-\tau_\nu}$ . We may sample from the cumulative probability distribution to give:

$$\xi = 1 - e^{-\tau_\nu} \quad (2.10)$$

$$\implies \tau_\nu = -\log(1 - \xi) \quad (2.11)$$

where  $\xi \in [0, 1]$  is a sampled random number equivalent to the value of the optical depth for that packet in that cell. The frequency of the photon packet and the mass density of the cell are then used to calculate the opacity of that cell and, using the fact that  $n\sigma_\nu = \kappa_\nu\rho$ , the distance  $l$  that the packet travels before its next interaction is calculated. If this value is greater than the distance from its position to the edge of the cell then the packet is moved along its current trajectory  $(\theta, \phi)$  to the cell boundary and the process is repeated. Alternatively, if the displacement is not sufficient for the packet to escape the cell then an event occurs. The packet is either scattered or absorbed with probability of scattering equal to the albedo of the cell

$$\omega = \frac{\sigma_{sca}}{\sigma_{sca} + \sigma_{abs}} \quad (2.12)$$

If the packet is absorbed then it is simply removed from the simulation as discussed above. If the packet is scattered then a new trajectory is sampled from an isotropic distribution in the comoving frame of the dust grain and the frequency of the packet recalculated using Lorentz transforms as described in the next section. This process is repeated until the packet has either escaped the outer bound of the supernova ejecta or been absorbed. Escaped packets are added to frequency bins weighted by  $w$  in order to produce an overall emergent line profile.

### 2.2.5 Doppler shifting

At emission and at each scattering event the frequency of the packet is recalculated according to a radial velocity field

$$v(r) = v_{max} \frac{r^\alpha}{R_{out}^\alpha} \quad (2.13)$$

where the maximum velocity,  $v_{max}$ , at the outer edge of the ejecta and the exponent of the velocity profile,  $\alpha$ , are declared in the input file.

It is worth noting that if a constant mass loss rate is required, the exponent of the velocity profile and the exponent of the density profile are not independent. A constant mass loss rate implies that  $4\pi\rho v R^2 \propto k$ , where  $k$  is a constant, and thus for  $v \propto r^\alpha$  and  $\rho \propto r^{-\beta}$ , we require that  $\beta - \alpha = 2$ . However, it is possible that the supernova event may have induced a mass-flow rate that is not constant with radius and thus both exponents may be declared independently. It is also worth noting that for supernovae in their free expansion phase, as the majority are by the time of the onset of dust formation, the ejecta are expanding with a  $v \propto r$  Hubble law expansion.

The outflow velocities in supernovae are extremely high of the order of 10% of the speed of light. Escaping radiation is therefore subject to significant, relativistic Doppler shifting. At emission and at each scattering event, the frequency of a packet must be recalculated according to the velocity of the scattering or emitting grain. When the packet is initially emitted, it has a frequency and a trajectory in the rest frame of the emitter. Both of these must be transformed to the observer's frame in order for the packet to be propagated through the grid. The new direction and frequency in the observer's frame may be simply found by transforming the momentum 4-vector  $\mathbf{P}$  which is defined as

$$\mathbf{P} = \begin{pmatrix} E \\ p_x \\ p_y \\ p_z \end{pmatrix} = \begin{pmatrix} h\nu \\ h\nu x \\ h\nu y \\ h\nu z \end{pmatrix} \quad (2.14)$$

We may then derive  $\mathbf{P}'$ , the momentum 4-vector in the observer's frame using the relation

$$\mathbf{P}' = \Lambda \mathbf{P} \quad (2.15)$$

where

$$\Lambda = \begin{pmatrix} \gamma & -\gamma\beta_x & -\gamma\beta_y & -\gamma\beta_z \\ -\gamma\beta_x & 1 + (\gamma - 1)\frac{\beta_x^2}{\beta^2} & (\gamma - 1)\frac{\beta_x\beta_y}{\beta^2} & (\gamma - 1)\frac{\beta_x\beta_z}{\beta^2} \\ -\gamma\beta_y & (\gamma - 1)\frac{\beta_y\beta_x}{\beta^2} & 1 + (\gamma - 1)\frac{\beta_y^2}{\beta^2} & (\gamma - 1)\frac{\beta_y\beta_z}{\beta^2} \\ -\gamma\beta_z & (\gamma - 1)\frac{\beta_z\beta_x}{\beta^2} & (\gamma - 1)\frac{\beta_z\beta_y}{\beta^2} & 1 + (\gamma - 1)\frac{\beta_z^2}{\beta^2} \end{pmatrix} \quad (2.16)$$

and  $\boldsymbol{\beta} = \frac{\mathbf{v}}{c} = (\beta_x, \beta_y, \beta_z)$ ,  $\beta = |\boldsymbol{\beta}|$  and  $\gamma = \frac{1}{\sqrt{1-\beta^2}}$ .

In practice, the velocities considered are low enough that it is unnecessary to consider terms of order  $O(\frac{v^2}{c^2})$  and thus  $\Lambda$  may be reduced to

$$\Lambda = \begin{pmatrix} 1 & -\beta_x & -\beta_y & -\beta_z \\ -\beta_x & 1 & 0 & 0 \\ -\beta_y & 0 & 1 & 0 \\ -\beta_z & 0 & 0 & 1 \end{pmatrix} \quad (2.17)$$

The new direction of travel and frequency in the observer's frame are therefore given by

$$\nu' = \nu(1 - x\beta_x - y\beta_y - z\beta_z) \quad (2.18)$$

$$x' = \frac{\nu}{\nu'}(x - \beta_x)$$

$$y' = \frac{\nu}{\nu'}(y - \beta_y)$$

$$z' = \frac{\nu}{\nu'}(z - \beta_z)$$

For each scattering event, the packet must be transformed both into and out of the comoving frame. The reverse transform is applied by using the inverse Lorentz matrix  $\Lambda^{-1}$  which is obtained by reversing the sign of  $\mathbf{v}$ . Positive  $\mathbf{v}$  is defined for frames moving

away from each other and thus  $\mathbf{v}$  is defined to be negative in the direction of the observer.

**Table 2.1.** Values of  $q_{H\alpha}(T)$  at three different temperatures as used by Damocles.

	Temperature (K)		
	5,000	10,000	20,000
$q_{H\alpha}$ (erg cm <sup>3</sup> s <sup>-1</sup> )	$6.71 \times 10^{-25}$	$3.56 \times 10^{-25}$	$1.83 \times 10^{-24}$

### 2.2.6 Electron Scattering

As will be discussed in detail in chapter three, the effects of scattering on the shapes of line profiles can be quite pronounced and it is therefore important to consider the potential effects of electron scattering as well as those of dust scattering. A simple treatment of electron scattering calculates electron densities using an estimated average temperature of either 5,000K, 10,000K or 20,000K. An observed luminosity of  $H_\alpha$  is then used to calculate the optical depth to electrons. The overall optical depth within each cell is calculated as  $\tau = \tau_{dust} + \tau_e$ , with  $\tau_e = 0$  if electron scattering is not activated. The electron scattering optical depth,  $\tau_e$ , in a given cell (with constant properties therein) is calculated as

$$\tau_e = n_e \sigma_t l \quad (2.19)$$

where  $n_e$  is the electron density in that cell,  $\sigma_t$  is the Thomson cross-section of interaction for an electron and  $l$  is the distance travelled.

In order to calculate this value, the electron density in each cell must be known. We assume that the electron density is the same as the proton density and that both are distributed according to the gas density distribution such that

$$n_e(r) = kr^{-\beta} \quad (2.20)$$

where  $k$  is a constant. The value of  $k$  must be determined from the total  $H\alpha$  luminosity.

The total H $\alpha$  luminosity ( $L_{H\alpha}$ ) is given by

$$L_{H\alpha} = \int_0^\infty n_p(r) n_e(r) E_{H\alpha} \alpha_{H\alpha}^{eff}(T) 4\pi r^2 dr \quad (2.21)$$

$$= \int_{R_{in}}^{R_{out}} n_p(r) n_e(r) q_{H\alpha}(T) 4\pi r^2 dr \quad (2.22)$$

where  $n_p(r)$  is the proton density at radius  $r$ ,  $n_e(r)$  is the electron density at radius  $r$ ,  $T$  is the temperature,  $\alpha_{H\alpha}^{eff}(T)$  is the temperature-dependent effective recombination coefficient for H $\alpha$ ,  $E_{H\alpha}$  is the energy of a single H $\alpha$  photon and

$$q_{H\alpha} = E_{H\alpha} \alpha_{H\alpha}^{eff} = \frac{4\pi j_{H\alpha}}{n_e n_p} \quad (2.23)$$

where  $j_{H\alpha}$  is the temperature-dependent emission coefficient for H $\alpha$  (i.e. the energy emitted per unit volume per unit time per unit solid angle). Substituting equation 2.20 into equation 2.22 gives the following

$$\frac{L_{H\alpha}}{4\pi q_{H\alpha}} = k^2 \int_{R_{in}}^{R_{out}} r^{2(1-\beta)} dr \quad (2.24)$$

which in the case  $\beta \neq \frac{3}{2}$  may be solved as

$$k = \sqrt{\frac{L_{H\alpha}}{4\pi q_{H\alpha}} \frac{3 - 2\beta}{R_{out}^{3-2\beta} - R_{in}^{3-2\beta}}} \quad (2.25)$$

and for  $\beta = \frac{3}{2}$  is

$$k = \sqrt{\frac{L_{H\alpha}}{4\pi q_{H\alpha}} \frac{1}{\ln(R_{out}/R_{in})}} \quad (2.26)$$

Substituting  $k$  back into equation 2.20 gives the electron density for each cell. In the code, only three gas temperatures may be specified and three corresponding values of  $q_{H\alpha}(T)$  are included as per Table 2.1.

If, for a given packet, an event occurs, it is first calculated whether this is a dust event

or an electron scattering event by considering the ratio of the optical depths of each to the total optical depth. The process by which a packet is scattered by an electron is almost identical to the dust scattering process except for the adopted velocity of the scatterer. In the case of a dust grain, the velocity is simply the bulk velocity of the ejecta at that radius as determined from the specified velocity profile. For an electron, the assumed velocity must include a thermal component as well as the same bulk velocity as would be adopted for a dust grain at the same location. As per the electron scattering calculation of CITE HILLIER, the components ( $v_x, v_y, v_z$ ) of the thermal velocity  $\mathbf{v}_{therm}$  are assumed to follow a Maxwellian distribution with zero mean and standard deviation

$$\sigma = \sqrt{\frac{kT}{m_e}} \quad (2.27)$$

where  $k$  is Boltzman's constant and  $m_e$  is the mass of an electron. The components are then sampled from a normal distribution with specified mean and standard deviation using the Marsaglia polar method CITE MARSAGLIA. This method generates two random numbers from a uniform distribution in the interval [0,1) and uses a number of transformations to convert them to random numbers as generated from a standard normal distribution with zero mean and unity variance. They may then be scaled to the appropriate normal distribution. Finally, the overall velocity of the electron is then calculated as  $\mathbf{v}_e = \mathbf{v}_{bulk} + \mathbf{v}_{therm}$  and the Lorentz transforms are applied in the same manner as a dust scattering event.

In the majority of cases it seems that the electron densities are not high enough to discernibly effect the overall shape of the profile. However, there may be a few rare cases (the concept is discussed for SN 2010jl (Fransson et al. 2013)) where the electron densities are high enough to become significant in the observed profiles. Whilst the inclusion of electron scattering in the code is an approximation since it is not necessarily true that  $n_e = n_p$  and the exact gas temperature is unknown, it gives a good suggestion of the potential effects of electron scattering.

### 2.2.7 Doublets

One of the lines in supernovae emission spectra that is frequently seen to be blue shifted is the forbidden [OI] $\lambda 6300, 6363\text{\AA}$  doublet. DAMOCLES therefore has the capacity to treat

doublets as well as single lines. When a doublet is specified, both the initial wavelengths and the initial intensity ratio must be declared. The code will create a wider frequency array than for a single line in order to accommodate both lines. It will then model each line independently, adding the final fluxes of the lines to produce the desired doublet at the end of the modelling.

### 2.2.8 Comparing the Model with Observations

Damocles includes the capacity to read in observed line profile data for direct comparison with a modelled line profile. Once all packets have been processed through the nebula and collected into bins, a flux is calculated at each of the wavelength bins in the observed data by interpolating between modelled wavelength bins. A chi-squared calculation is then performed to compare the model with the data quantitatively, where

$$\chi^2 = \sum_i \frac{(f_{obs,i} - f_{mod,i})^2}{\epsilon_i^2} \quad (2.28)$$

and  $f_{obs,i}$  is the observed flux in the  $i^{\text{th}}$  frequency bin,  $f_{mod,i}$  is the modelled flux in the  $i^{\text{th}}$  frequency bin, and  $\epsilon_i$  is the normalised error on the  $i^{\text{th}}$  frequency bin. Minimising  $\chi^2$  minimises the error between the model and the observed line and therefore provides a quantitative measure of goodness of fit that may be used in addition to or instead of any qualitative assessment.

## 2.3 The Structure of Damocles

Damocles is written using Fortran 95. Since the major modernisation of Fortran 77 in 1990, the language includes a number of more modern elements that make it an ideal choice for this type of numerical computation. Firstly, a fast, high-level language is required that allows for dynamic memory allocation and deallocation. Whilst Damocles could have been written in a number of other languages, this is a critical feature that is only available in a few languages. Very large numbers of packets are required to achieve reasonable resolutions in Monte Carlo codes of this nature and therefore large arrays of data are required. The ability to maintain careful control of memory allocation is therefore very important.

Fortran 95 also has a number of other features that make it especially suitable for

this sort of code. Derived types group a number of variables of different intrinsic or other derived types. This allows different properties of a particular item (for example a packet or grid cell) to be grouped together and accessed via that item. Though not a necessary feature, derived types make the code clearer, faster and more legible. They also make it easier to write and therefore help to minimise the risk of errors. Similarly, the modular structure that was introduced to Fortran in 1990 allow the programmer to distribute their code over a number of modules and allow variables that are declared within a particular module to be accessible to others. This eliminates the need for common blocks of code and allows a large code to be segmented into logical divisions. Again, this allows for increased speed, clarity and ease of maintenance and development in the future.

The obvious alternative programming language to Fortran 95 is C or C++. Both of these languages have all of the features described above and are exceptionally fast. From a computation perspective, there is, arguably, little to separate them for this type of coding. I ultimately decided to write Damocles in Fortran 95 because of its heritage in astrophysics. A very large number of astrophysical codes have been written using current or previous versions of Fortran and writing the code in Fortran 95 allowed for easy compatibility.

Damocles is parallelised using OpenMP (see Section 2.3.2) which restricts its use to shared memory machines. It has been developed on and currently runs on a MacBook Pro 11.2 quad core with Intel Core i7 2.8GHz processors and 16GB of memory. A typical, medium resolution simulation takes approximately 10 seconds.

### 2.3.1 Computational Architecture and Processes

Damocles was written using a modular structure. The "parent" driver has numerous "children" in the form of subroutines and modules which are each responsible for a separate task or tasks. This architecture has a number of advantages. Firstly, it serves to clarify both the functionality and legibility of the code allowing for easier debugging and maintenance. It also allows for the implementation of features such as recursive subroutines which are ideally suited to a Monte Carlo methodology. Finally, it allows for the code to be developed further in the future simply by including additional modules and subroutines. A brief description of every module and subroutine in the code is presented in the following subsections. The descriptions are ordered according to the first time they or their contents are called by the driver (see Figure 2.3 for a flowchart of the modular hierarchy).

### The driver

The *driver* module is at the centre of Damocles. It is from here that all subroutines are called. The calls to construct the grid and calculate dust opacities, to emit and propagate packets and to compare the results with observational data are all made from here. The parallelisation process is also controlled from here (see section 2.3.2 for more details on the parallel function of Damocles). Having called the initialisation routines, the driver is responsible for dividing the ejecta into shells and calculating how many packets are emitted within each shell. Each shell is looped over and each packet is looped over within each shell. Emission and propagation routines are called inside this loop. At the end of each packet's lifetime, either once it has been absorbed or has escaped, the driver adds the weighted packet's energy to the appropriate frequency bin and stores this information before looping back to emit and propagate the next packet. It is here that a line of sight is applied if so desired. This is achieved by collecting only packets that have escaped within a cone of vertical angle  $\pi/6$ . Once all packets have been processed, the driver writes the relevant information to the output file and calls the model comparison module.

The driver is also the section of code responsible for processing doublets. The code treats doublets by processing two batches of packets with differing initial frequency through the same grid. Before they are collected in frequency bins, the flux ratio that is specified by the user is applied to one batch of the packets. All packets are then collected as per a single line.

Various statistics are also processed and output here including the fraction of packets that are absorbed and the estimated undepleted luminosity of the observed line.

### The input module

The *input* module is where the primary input file is read into the code and all global variables are declared and assigned. A number of logicals are assigned based on values declared in the input file and some simple calculations are performed that determine the inner and outer radii based on the maximum velocity specified and the epoch of consideration. A number of physical constants that are used throughout the code are also declared here as 'parameters', meaning that their value cannot be changed at any point in the simulation.

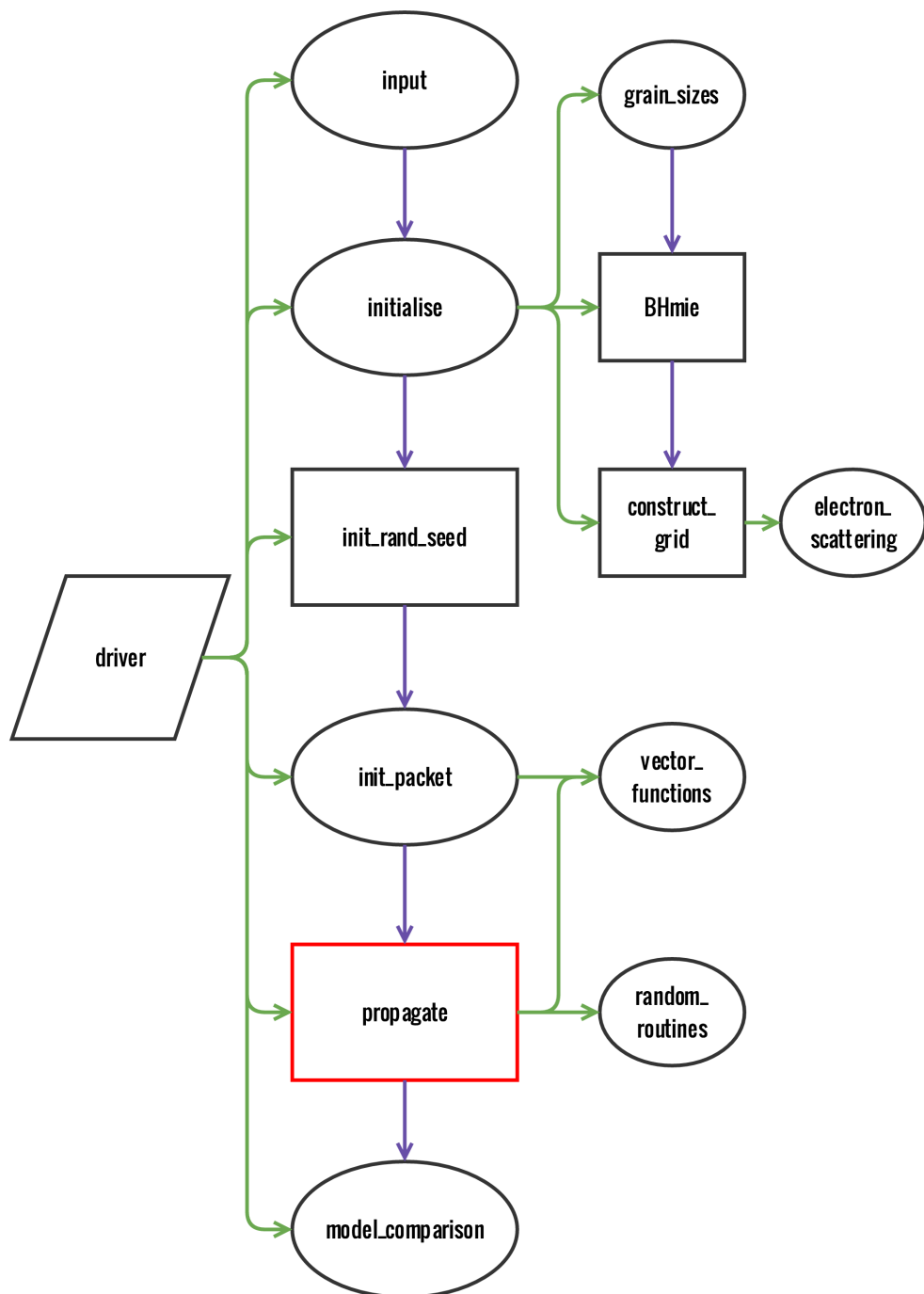


**Figure 2.3.** A flowchart representing the hierarchy of modules and subroutines in the Damocles code. Ellipses represent modules and rectangles represent subroutines (the red rectangle is a recursive subroutine). Green arrows indicate the dependence on module or subroutine on previous modules or subroutines. Purple arrows indicate the flow of the code.

### The initialisation module

The *initialise* module acts as a driver to run all of the subroutines associated with initialising the program. A number of dynamically allocatable arrays are declared allowing for a grid of densities to be calculated, a frequency grid to be stored and optical properties to be read in. Arrays to store the emergent spectrum are also declared. The calculation of dust opacities, which calls the *grain\_sizes* subroutine and the *BHmie* subroutine, is performed here. For each species, the wavelength-dependent optical properties,  $n$  and  $k$ , are read in and the Mie approximation applied to every pair of frequencies and grain sizes. The resulting extinction and scattering efficiencies are summed over all grain sizes for each wavelength, weighted appropriately, to calculate overall wavelength-dependent extinction and scattering opacities. These data are stored in an array that is accessed as a packet is processed through the grid.

The command to construct the grid is called before some basic statistics about the grid are calculated. The average optical depth from  $R_{in}$  to  $R_{out}$  in both the V band and the rest-frame wavelength of the line being modelled are calculated and sent to stdout. The average number density of grains in each cells is also computed and output. Finally, the frequency array that will divide the packets into bins is constructed.

This module is also where the *gridcell* derived type is declared. A *gridcell* type was specified as it allowed for easy and clear access to any of a grid cell's properties as a packet is passing through it. The type consists of a number of arrays of real, integer and logical variables. The properties recorded for each cell include the physical bounds of the cell in each axis, the mass and number dust densities, the electron density, an identifying number and a logical clumped property.

### The grain size module

The *grain\_sizes* module reads in the file that specifies the list of species to be used. This file is a list of species detailing for each one the name of the file containing the optical data for the species, the relative abundance of that species, the maximum and minimum grain sizes and the exponent of the power law of the grain size distribution. It also declares a grain size resolution. These properties are all read in by the *grain\_sizes* module and a relative weight calculated for each grain size for each species. The *species* is declared in this module. As for the *gridcell* type, using a derived type allowed for the easy storing

and accessing of a large number of properties of each species. Many multi-dimensional arrays and scalars were stored for the *species* type that included properties relating to the grain size distribution, the density of a dust grain, the extinction and scattering opacities and the relative abundance of the species amongst others. After processing of the optical data for a given species, all calculated quantities were stored in arrays as a component of the *species* type.

### The Mie approximation subroutine

The *BHmie* subroutine is a standard routine that was obtained from an online library of routines. It is a modified version of the Bohren and Huffman (1983) Mie scattering routine. It applies a complex algorithm to approximate the extinction and scattering efficiencies of a single size grain at a specified wavelength given its complex refractive index  $n + ik$ .

### The grid construction subroutine

The *construct\_grid* subroutine is called from within the initialisation module. The purpose of this subroutine is to populate the grid, which is an array of derived type *gridcell* and size  $n_{cells}$  where  $n_{cells}$  is the number of cells in the grid. The bounds of the grid are initialised and the radii of all cells from the centre of the grid to the centre of the cell calculated. The density of each cell is then calculated according to the smooth distribution and scaled so that the total dust mass is equal to that specified in the input file. If clumps are used then the total number of clumps is calculated and these are distributed throughout the grid stochastically according to the smooth density profile stipulated. This subroutine also calls the electron scattering subroutine contained within the *electron\_scattering* module so that the electron density of a cell may be stored at the same point as the dust density.

### The electron scattering module

The *electron\_scattering* subroutine is a simple subroutine that is used to calculate the value of  $k$  as described in equation 2.20. The total H $\alpha$  luminosity and the gas temperature are read in and the gas temperature used to determine the appropriate value of  $q_{H\alpha}$  from Table 2.1. These values are then used to calculate the value of  $k$  as described by equations 2.25 and 2.26. The variable is passed back to the *grid construction* subroutine where it is used to calculate the electron density in each cell. The electron densities will be used by the *propagate* subroutine to calculate the electron scattering optical depth in each cell.

### The random seed subroutine

The *init\_rand\_seed* is a short subroutine that calculates a seed for the standard Fortran pseudo-random number generator (*random\_number*). It uses the system clock to generate the random seed and thus varies with every implementation of the code. A seed is a number that is used as a 'starting point' for a pseudo-random number generator. Varying the random seed ensures that a different set of random numbers is generated every time the code is run, which can be useful to ensure that any peculiar or interesting features of the code are definitely a product of the physical processes and not as a result of random fluctuations in the simulation. The more packets are used however, the more the Monte Carlo noise in the emergent line profile is reduced and the contribution from any anomalous packets should be insignificant.

### The packet initialisation module

The *init\_packet* module is responsible for the creation and emission of packets at the start of the simulation. It is called from the driver for each packet. By generating an array of five random numbers, the position and emission direction vectors in the rest frame of the emitter are calculated according to the formulae described in equation 2.7. The scalar velocity of the emitter is calculated based on its radial position and this converted into a velocity vector by normalising the position vector and multiplying by the scalar velocity. The velocity vector is passed to the Lorentz transforms subroutine contained the *vector\_functions* module. The frequency of the packet is also passed to this subroutine. After the emission direction vector and frequency of the packet have been updated, the grid cell in which the packet starts its path is identified and the code passes back to the driver to propagate the packet through the nebula.

### The vector functions module

A number of vector functions are contained within the *vector\_functions* module and are accessed throughout the simulation. These include normalisation functions, conversions from spherical coordinates to cartesian and both forward and inverse Lorentz transforms. It is the latter of these that is most important for the physics of the code. The Lorentz functions are called for each packet at emission from the *driver* and at every subsequent scattering event from within the *propagate* routine. As well as performing the necessary frequency shift based on the velocity of the scatterer or emitter, they also transform into

and out of the rest frame of the particle thus ensuring that the packet is propagated through the nebula with a direction in the rest frame of the observer but that its new direction is sampled from an isotropic distribution in the rest frame of the influencing dust grain.

The  $\beta$  and  $\gamma$  values are calculated based on the input velocity vector. The momentum 4-vector is then multiplied by the Lorentz matrix using the Fortran function *matmul* to produce a new frequency and a new direction vector in the appropriate frame of reference. If a scattering event has occurred then the weight of the packet is also updated here. The new direction vector, frequency and weight are then passed back to the propagate routine and the process repeated. At each scattering event the inverse Lorentz matrix must first be applied to move from the observer's rest frame to the particle's. A new direction vector must then be sampled from an isotropic distribution before applying the forward Lorentz transform to move back from the rest frame of the dust grain to the observer's frame. The next step in the packet's trajectory may then be calculated in the *propagate* subroutine.

### **The propagate subroutine**

The *propagate* subroutine is at the heart of the Monte Carlo simulation. It is here that the trajectories and experiences of all packets in the simulation are determined. The *propagate* is a subprogram called a *recursive subroutine*. This allows the subroutine to call itself, at which point it will loop back to the start of the subroutine. It will continue this process until a condition is reached that instructs it to return to the driver. In this case a number of conditions will arrest the circulation of the packet. If the packet has escaped the outer radius of the ejecta or has been absorbed then the routine will pass this information along with the frequency and weight of the packet back to the driver. The routine would also stop recurring if a packet has undergone a maximum number of scattering events. At this point it is deemed that the weight of the packet is so small as to be negligible and it is classified as 'inactive'. This prevents the code from lagging by becoming stuck on a particular packet that has become trapped in a region of high density and albedo.

There are a number of processes that take place in this module in order to propagate a packet through the nebula accurately. A full pictorial representation of the procedures that are implemented in this module may be found in the flowchart in Figure 2.4. For each packet in each cell, the optical depth in that cell is calculated based on the opacity and density at the frequency of the packet. These are obtained by interpolating between

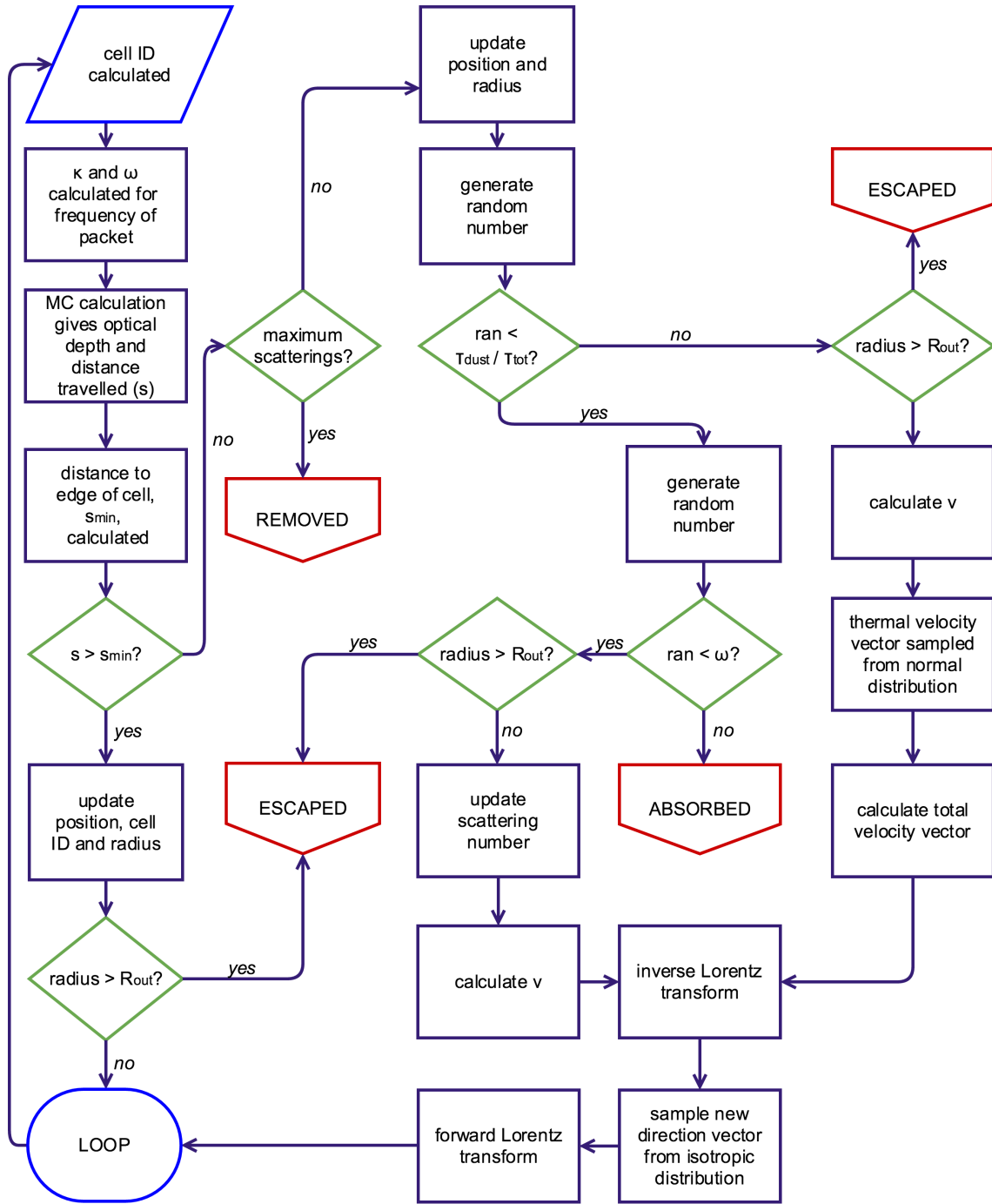


**Figure 2.4.** A flowchart representing the processes that occur in the *propagate* subroutine. The life of a packet passing through the grid may be determined by following the flowchart starting at the blue parallelogram. Purple ovals indicate a standard step in the evolution, green diamonds indicate that a determination must be made, red boxes mean that the packet's evolution has concluded as it has escaped, been absorbed or been removed and the blue rounded oval indicates a return to the start of the routine.

discrete opacities at points in the frequency array. This is the point at which the Monte Carlo technique is applied in order to determine the distance travelled by the packet. This displacement is then compared to the distance to the edges of the cell in order to ascertain whether or not the packet escapes the cell. If it does then the process is repeated until either an event occurs or the packet escapes the nebula. If an event occurs, a series of random numbers are sampled in order to determine whether or not the packet suffers electron scattering, dust scattering or absorption. If the packet is absorbed then it is removed from the simulation. If it is scattered then the velocity vector is calculated. In the case of electron scattering this involves considering the thermal velocity component as well as the bulk velocity at that radius. The Lorentz transforms are applied updating the frequency of the packet and a new direction of propagation sampled, and the routine is recalled to start afresh.

### The random routines module

The *random\_routines* module contains a single subroutine which is, like the *BHmie* routine, a standard routine obtained from an online library. It allows for a random velocity vector to be sampled from a normal distribution with specified mean and standard deviation. The standard deviation is calculated as per equation 2.27 and passed to the subroutine which samples a random 3-dimensional vector from the normal distribution with the specified standard distribution and zero mean. This is passed back to the propagate routine where it is added to the bulk velocity in order to determine the overall velocity of the scattering electron.

### The model comparison module

The *model\_comparison* module is responsible for post-processing the outputted line profile and comparing the model results with inputted observed data. The routine interpolates between two model frequency points to obtain a flux value at each frequency point of the observed line profile. Both profiles are then normalised such that the total flux is unity. A  $\chi^2$  calculation is then performed as per equation 2.28. The smaller the value of  $\chi^2$ , the better the fit is.

### 2.3.2 OpenMP Parallelisation

Monte Carlo simulations are exceptionally well-suited to parallelisation. The path of each packet through the nebula is unaffected by the transport of any other packet. It is therefore possible to run multiple instances of the *propagate* module at once by using several cores. Since the vast majority of the processing power of the simulation is driven from this module, it is theoretically possible to achieve a nearly linear speed-up; i.e. if the number of cores is doubled, the run time should be approximately halved.

Damocles was parallelised using OpenMP. OpenMP is an Application Program Interface (API) that allows for shared-memory parallel programming in Fortran and C/C++. OpenMP causes the code to be run serially on a single processor until a parallel region is reached. At this point the single master thread branches into multiple threads, and multiple instances of the same section of code are run on each. In Damocles, this splitting occurs at the start of the loop which controls the emission and propagation of packets from each shell. If, for example,  $10^7$  packets are emitted and 5 threads are used, then approximately  $2 \times 10^6$  packets will be independently processed on each thread. Practically however, the OpenMP keyword *dynamic* is declared ensuring that, as soon as each thread has finished processing a packet, it immediately moves onto the next one. If the *static* keyword were specified instead then the number of packets to be processed would be equally divided between the threads at the start of the loop. In this case, if, by random chance, one thread happened to have significantly more absorbed packets than another, then potentially utilisable processing power would be lost as the core waited for the others to finish.

At the start of the parallel region variables accessed within the shared region are specified as shared or private. Private variables are not seen by other threads and allow the value of a single named variable, for example 'frequency', to have different values on different threads. Shared variables have the same value regardless of the thread number, for example, 'grid cell density'. As each packet esacpes, its weighted energy must be added to the final energy array. It is important that two threads do not attempt to alter the value of this shared array at the same time as data may be lost or corrupted and this section of code is therefore enclosed inside a *critical* region. This instruction specifies that code in this block is to be executed by only one thread at a time. Extensive testing was performed to ensure that outcomes were not affected by the implementation of a parallel

environment.

For further information about the OpenMP API please refer to <https://www.openmp.org>.

### 2.3.3 Input

There are a significant number of parameters that may be varied in the code. Many of these are important variable parameters that will be the parameters of interest when modelling. However, there are also a sizeable number of variables that allow other properties of the model to be controlled. All parameters can, broadly, be divided into one of three categories: properties of the emitted rest-frame line or doublet, properties of the dust and gas in the ejecta and properties of the grid and code architecture. I list all the variables that are input in the primary input file in table 2.2 and will here describe the basic meaning and function of each one.

**Table 2.2.** The input variables read in from the input file and example values

Input Variable	Example Value	Input Variable	Example Value
lambda1_0	636.3	MD_tot	1.0e-4
L_tot	0.003	l	1.0
L_Halpha	0.005	q	1.3
doublet	1	b	2.0
lambda2_0	630.0	gas_shell	1
L_ratio	3.1	v_max_gas	8000
ES	1	Rrat_gas	0.05
ES_temp	10000	l_gas	1.0
LS	0	q_gas	1.5
VelShift	1	b_gas	2.0
MF	0.5	ncells	50
FF	0.1	n_packets	1e8
dayno	680	n_bins	1000
v_max	5000	n_shells	100
Rrat	0.2	dustfile	'species_file.in'

## Properties of the emitted rest-frame line or doublet

### **lambda1\_0**

This is a real number that specifies the initial rest-frame monochromatic wavelength at which packets are emitted in nanometres. If a doublet is to be modelled then this represents the wavelength of one of the singlets.

### **L\_tot**

$L_{tot}$  is the total luminosity of the line in units of  $10^{40}$  ergs s $^{-1}$ . The initial energy of each packet ( $E_0$ ) is therefore  $L_{tot}$  divided by the total number of packets used in the simulation. For lines which have accurate observed fluxes, this allows for the flux of the line to be modelled in addition to the shape. This variable is also used to estimate the undepleted luminosity of the observed line when it is initially emitted from the ejecta.

### **L\_Halpha**

Similar to  $L_{tot}$ ,  $L_{H\alpha}$  is the total luminosity of the H $\alpha$  line. In the case of H $\alpha$  modelling, this value should be the same as the value of  $L_{tot}$ . This variable is used in the calculation of the electron density and it is not necessary to specify it unless the electron scattering environment is switched on (see section 2.2.6 for further details).

### **doublet**

This is an integer of value 1 or 0 that indicates the use or otherwise of the doublet environment. If set to 1 it triggers the doublet logical in the code to be initialised to *true*. The code will then read in the values of  $\text{lambda2\_0}$  and  $L_{ratio}$  in order to initialise packets with two different starting monochromatic wavelengths. Packets are processed through the nebula as normal before being collated in bins weighted according to both their history and the weight of their parent singlet.

### **lambda2\_0**

This is a real number that specifies the initial rest-frame monochromatic wavelength of packets emitted from the second singlet in a doublet environment. The wavelength is specified in nanometres.

### **L\_ratio**

This real number gives the ratio between the respective luminosities of singlets in a doublet environment. The ratio should be declared as the flux at lambda1\_0 divided by the flux at lambda2\_0. It is expected that the doublet environment will generally be used to model forbidden lines, especially the [OI] $\lambda 6300, 6363\text{\AA}$  doublet, where the ratio between the singlets may be theoretically determined.

## **properties of the dust and gas in the ejecta**

### **ES**

This keyword is similar to the doublet keyword in that, by setting it equal to 1 or 0, it indicates the use or otherwise of the electron scattering environment. If it is set to 1 then it initialises the electron scattering logical in the code to *true*. If the electron scattering environment is switched on then this triggers the calculation of approximate electron densities for every cell in the grid. This density contributes to the total optical depth of a cell and, as packets are propagated through each cell, they will experience an electron scattering event with probability  $1 - e^{\tau_e}$ , where  $\tau_e$  is the electron scattering optical depth.

### **ES\_temp**

When the electron scattering environment is switched on, it is necessary to calculate the electron density of each cell in the grid. In order to do this an average gas temperature must be specified to allow for Q-values to be calculated. Damocles will not accept any value for this input variable; only 5000K, 10000K and 20000K will be accepted. These are thought to be a representative range of temperatures for the ejecta of supernovae at epochs where electron scattering still has potential to influence the profiles. These values were selected as they are the values for which Q-values are given in Osterbrock.

### **MF**

If this keyword (short for mass fraction) is set to 0 then a smooth density distribution of both gas and dust will be constructed. If it is not however, then this will automatically initialise the clumping logical present in the code to *true*. The value specified should be between 0 and 1 and gives the total fraction of the dust mass that should be located in

clumps. The remaining fraction will be smoothly distributed according to the profiles described in the input file.

## **FF**

If the clumping environment is switched on (using the **MF** keyword) then **FF** declares the total filling factor of the clumps. The filling factor is defined as the fraction of the total volume of the ejecta that is occupied by clumps. For a fixed clump size, this parameter effectively determines the number of clumps to be used. Once the number of clumps to be used has been determined, the mass fraction then determines the density of the clumps.

## **dayno**

This keyword represents the epoch being modelled. In combination with the declared maximum velocity, it is used to consistently calculate an outer radius as

$$R_{out} = 8.64 \times 10^{-6} \left( \frac{t}{\text{days}} \right) \left( \frac{v_{max}}{\text{km s}^{-1}} \right) \quad (2.29)$$

where  $R_{out}$  is in units of  $10^{15}\text{cm}$ .

## **v\_max**

This is the maximum velocity used in the code. It is assumed to be the velocity at the outer radius of the ejecta and is used to construct a velocity profile of the form

$$v = v_{max} \left( \frac{r}{R_{out}} \right)^l \quad (2.30)$$

where  $l$  is also declared in the input file and  $R_{out}$  is calculated based on the epoch and the maximum velocity.

## **Rrat**

This number is the ratio between the inner and outer radii. Once the outer radius has been calculated as per equation 2.29, this ratio is used to calculate the value of the inner radius.

**MD\_tot**

This real number specifies the total dust mass to be distributed throughout the grid in solar masses ( $M_{\odot}$ ).

**l**

$l$  is the exponent of the radial velocity law in the code as per equation 2.30.

**q**

$q$  describes the relationship between the radial dust density distribution and the emissivity distribution. It is the exponent of the emissivity distribution as a function of density such that  $i(\rho) \propto \rho^q$  where  $i(\rho)$  is the emissivity at a given density. Though this parameter may take any real value, it is frequently fixed to be  $i(\rho) \propto \rho^2$ , i.e. proportional to the product of the recombining proton and electron densities in the case of H $\alpha$  and to the product of the neutral oxygen and electron densities in the case of collisionally excited [O I] emission.

**b**

This parameter describes the value of the exponent of the dust density distribution in terms of radius such that  $\rho \propto r^{-b}$ .

**gas\_shell**

This flag may be set to 0 or 1 to indicate that dust and gas are coupled or decoupled respectively. If it is set to 1 then the 'decoupled' logical in the code is set to *true* then the gas follows a distribution that is independent of the distribution followed by the dust. The following five parameters specify the geometry of the emitting gas. It is worth noting that in the case where gas and dust are coupled to each other, the gas follows the same distributions as specified for dust by the parameters described above.

**v\_max\_gas**

This is the gas analogue of the v\_max parameter described above.

**Rrat\_gas**

This is the gas analogue of the Rrat parameter described above.

**l\_gas**

This is the gas analogue of the parameter l described above.

**q\_gas**

This is the gas analogue of the parameter q described above.

**b\_gas**

This is the gas analogue of the parameter b described above.

**Properties of the grid and code architecture****LS**

Whilst the initial distribution of gas and dust is symmetrical, it is not necessary to consider a single line of sight as all lines of sight will produce the same profile and it is therefore more efficient to collect all packets that escape regardless of their direction of flight. However, if alternative, axisymmetrical or non-symmetrical geometries are to be used it is important to be able to specify a line of sight. If this keyword is set to 1 then the 'line of sight logical' will be initialised as *true*. Only packets that escape within a cone of vertical angle  $\pi/6$  will be collected. Clearly, in practice, the angle would be very much smaller but it is prohibitively expensive to run enough packets through the simulation that enough are collected to achieve a reasonable resolution when a very small vertical angle is adopted.

A representation of this construction is presented in Figure ??.

**VelShift**

This is another environment flag. As a packet is transported through the nebula it may experience repeated scattering events that shifts its original frequency beyond that expected from the maximum theoretical velocity. It is discussed in depth in chapter three how this process of 'velocity shifting' may result in a profile that exhibits an extended red wing. It is useful for the purposes of comparison and investigation to be able to turn off this process of repeated scattering events so that the only frequency shift experienced by a packet is at emission.

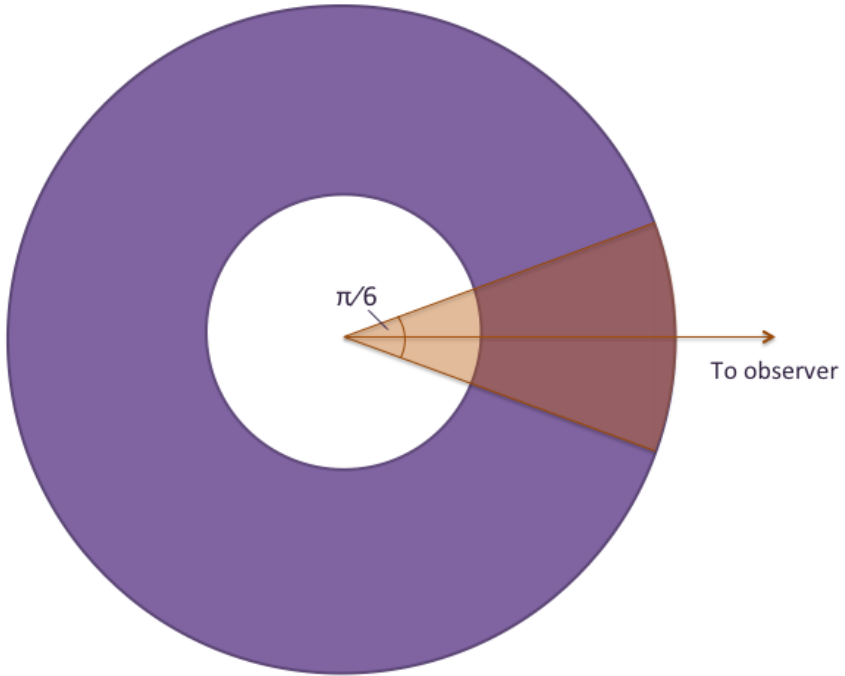


**Figure 2.5.** Schematic representing which packets are collected when the line of sight environment is switched on. Packets that contribute to the emergent line profile are those that escape the nebula within a cone with vertical angle  $\pi/6$ .

### ncells

The edges of the grid in each direction are given by  $\pm R_{out}$  and the number of cells in each axis to divide the grid into by ncells. The total number of cells in the grid is therefore  $ncells^3$ .

### n\_packets

This variable determines the number of packets to be emitted and processed through the grid. This parameter is particularly important for achieving a resolution that is high enough to give representative results. The larger the number of packets used, the less noise is present in the final profile. The Monte Carlo process introduces noise that can sometimes be construed as a result when it is in fact an artefact. Using a large number of packets reduces this risk and improves the output of the model. In general, the more dense an environment, the more packets it is necessary to use. This is because any packets which are absorbed are removed from the simulation and therefore reduce the desired resolution. Since the vast majority of the total processing power is used to propagate packets through

the grid, an increase in the number of packets results in a significant decrease in runtime. Low albedo, optically thick simulations have a significantly longer runtime than optically thin scenarios. When choosing this parameter, a careful balance must be found between the total runtime and the desired resolution.

### **n\_bins**

This value gives the total number of divisions in the frequency array and thus determines the overall frequency resolution. Since the resulting profile is in fact a histogram binned into a frequency array, it is important that these divisions are fine enough to provide a seemingly continuous line profile. Apparent jumps or discontinuities could be produced if too few bins are used.

### **n\_shells**

This parameter controls the total number of shells the ejecta is divided into. If a particularly steep radial profile is adopted for either the velocity profile or the density profile then the user may wish to increase the number of shells used to compensate. Increase the number of shells and the total number of frequency bins will have an effect on the overall runtime, but this will be insignificant in comparison to altering the number of packets. However, it must be determined that neither of these parameters are detrimentally affecting the results.

### **dustfile**

Finally, this string gives the name of the input file that itemises the list of species, their relative abundances and size distributions.

#### **2.3.4 Output, Post-Processing and Visualisation**

The primary output file contains details of the emergent line profile. Three columns are written out to the file at the end of the simulation. These are the wavelength, velocity and flux of the modelled line profile. Another output file is also produced by the *model\_comparison* module. This file prints both the inputted observed line profile and the outputted emergent line profile to one file in the same velocity bins. This allows for easy plotting. The columns printed in this file are wavelength, modelled flux and observed

**Table 2.3.** List of all outputs and example values produced by the Damocles code.

Output	Example Value
Total number of cells	125000
Number of grid cells inside ejecta	65544
Total volume of supernova ( $10^{42}$ cm $^3$ )	304523264
Volume of a grid cell / Volume of a clump ( $10^{42}$ cm $^3$ )	4668.52
Width of a grid cell (cm)	1.67e+15
Mass check (calculated as $\rho V$ )	6.03e-04
Average grain number density (cm $^{-3}$ )	1.96e-09
Extinction to rest-frame wavelength	2.94e-08
Scattering extinction to rest-frame wavelength	1.63e-08
Albedo for rest-frame wavelength	0.554
Average optical depth to rest-frame wavelength	2.062
Average optical depth in V band	4.12
Average electron density (cm $^{-3}$ )	71509.1
Average electron scattering optical depth	1.31e-02
Total number of packets	99999
Number of active (propagated) packets	99999
Number of inactive packets	0
Number of absorbed packets	82949
Percentage of absorbed packets out of all active packets	82.95
Number of packets in line of sight	17050
Percentage of escaped packets in line of sight	100.0
Estimated undepleted luminosity ( $10^{40}$ ergs s $^{-1}$ )	1.10e-05
Total (depleted) luminosity ( $10^{40}$ ergs s $^{-1}$ )	1.90e-06
Total energy absorbed ( $10^{40}$ ergs s $^{-1}$ )	1.57e-06
Energy per active packet ( $10^{40}$ ergs s $^{-1}$ )	1.90e-11
Chi-squared	0.3557

flux and the total flux is normalised to unity for both line profiles. Both of these files may be represented graphically in a straightforward fashion using any plotting package. In addition to these output files, a number of useful quantities are also calculated by Damocles and output to *stdout* throughout the course of the simulation. If desired, the user may direct the *stdout* to a file for a record of these quantities. A list of all quantities output by Damocles is given in Table 2.3.

Throughout my modelling, I use standard and custom routines written with MATLAB to plot line profiles, both modelled and observed. I also use MATLAB to process some of the data. For example, where I have observations with accurate observed fluxes, I scale the modelled profile to the observed profile so that fluxes remain to scale. This is initially performed by a custom MATLAB routine which smooths the modelled data to reduce any Monte Carlo noise before identifying the maximum flux value. Identifying the peak flux of the observed line profile allows the modelled profile to be automatically scaled. Any inaccuracies in the scaling may then be easily adjusted manually. I also use MATLAB for any other illustrative graphs or plots, for example, the plots in Figure 2.2 were generated in MATLAB using its 3D-scatter plotting function.

## 2.4 Further Developments

The modular structure of Damocles allows for easy implementation of additional functionality in the future. By simply adding extra modules, extra physics can be included in the code. There is potential for this code to be expanded in a number of directions. An immediately apparent development involves the dust itself. Treatment and understanding of the dust in the ejecta is crucial to understanding the shape of the line profile. The ability to place different species in different locations within the ejecta is not currently included. This would allow for stratified or asymmetrical distributions of dust species motivated by the potentially discrete locations of the parent elements. Similarly, streamlining the ability to model arbitrary density distributions and geometries would allow for more complex and accurate modelling of supernova ejecta. The ejecta of SN 1987A, for example, is known to have an asymmetric distribution which could potentially affect the contour of the line profile.

More widely, supernova explosions can sometimes result in radiation that is polarised. By including the capacity to model polarised radiation on the code, we may able to

glean further information about the distribution and nature of dust forming within the ejecta. It would also be theoretically possible to expand the code to become a fully self-consistent radiative transfer code or to include certain approximations (e.g. the Sobolev approximation) to allow for full spectral modelling throughout the optical and infrared.

This page was intentionally left blank

# Chapter 3

---

## Benchmarking and Testing

There is a general lack of published models in the literature that consider dust absorption-affected asymmetric line profiles. We therefore test the code by comparing the results to optically thin profiles that may be derived analytically. We then test the absorption and scattering components of the code by comparing our results in the case of an optically thick medium with those derived by ? in their Model II and Model III scenarios.

### 3.1 Theoretical line profiles from first principles

Analytical profiles may be calculated in the dust-free case. We ran a number of models based on the methods of Gerasimovic (1933) who derived equations for line profiles emitted from a transparent expanding shell.

Describing the fractional expansion velocity of the shell as  $v(r) = r^\alpha$  with  $\alpha \neq 0$  such that  $v(r) = \frac{V(r)}{V_{max}}$  where  $V(r)$  and  $V_{max}$  represent physical velocities and  $v_{max} = 1$ , the energy emitted by the nebula between radial velocities  $v$  and  $v + dv$  is proportional to

$$\int_\tau i(r) r \sin(\theta) r d\theta dr \tag{3.1}$$

where  $i(r)$  represents the emission per unit volume at radius  $r$  and  $\theta$  is the angle to the observer's line of sight. We adopt inner radius  $R = q$  and outer radius  $R = 1$ .

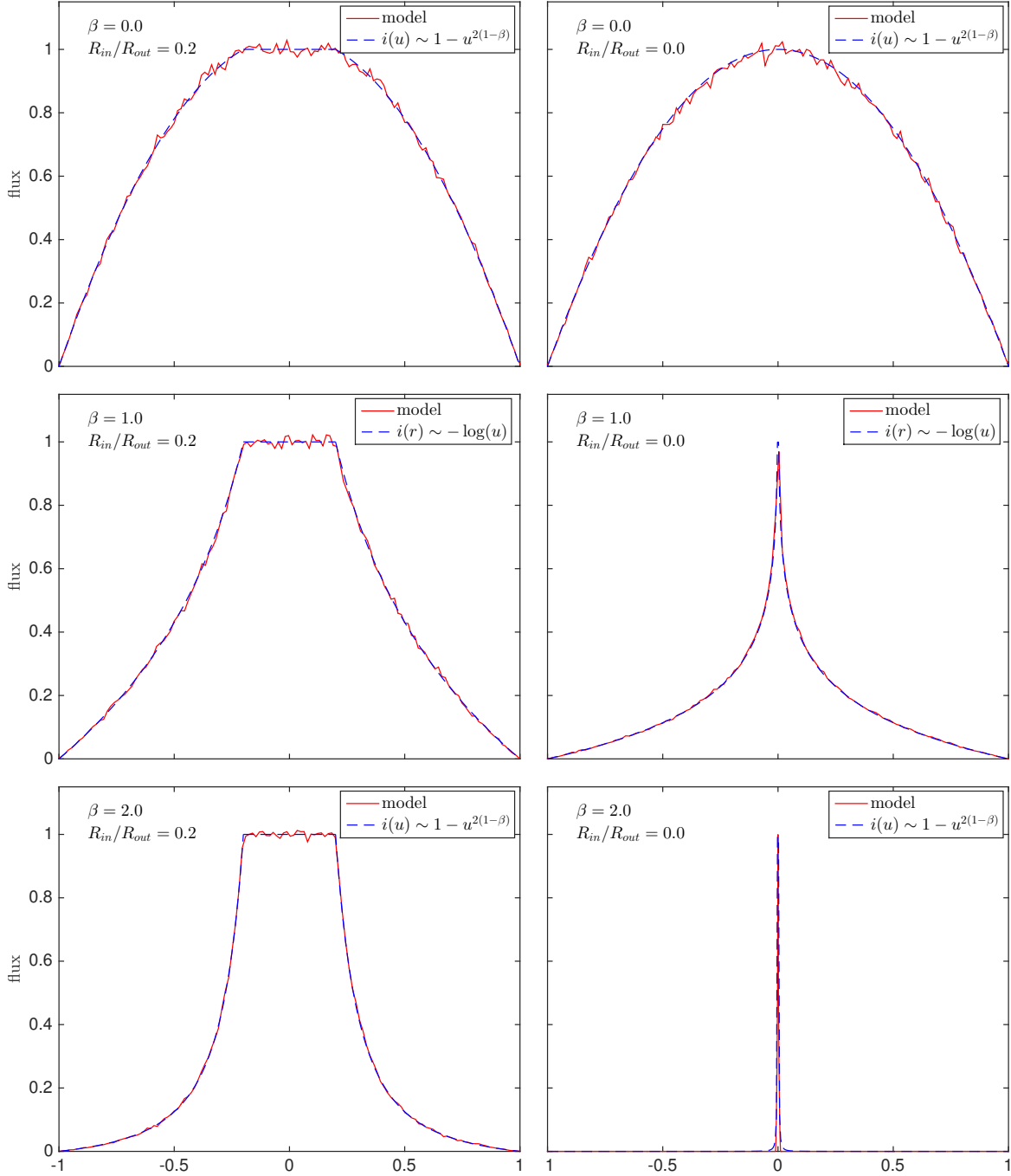


**Figure 3.1.** Red: Benchmark models for optically thin ( $\tau = 0$ ) line profiles with fractional velocity  $v \propto r$ . Left to right: initial emissivity profiles  $i(r) \propto r^{-2\beta}$  with  $\beta = 0.0$ ,  $\beta = 1.0$  and  $\beta = 2.0$ . Cases with  $R_{in}/R_{out} = 0.2$  are on the top and  $R_{in}/R_{out} = 0.0$  on the bottom. The presence of a plateau in the upper plots is due to the finite inner radius (detached shell). Blue: The analytical case with  $i(u) \sim 1 - u^{2(1-\beta)}$  except in the case of  $\beta = 1$  where  $i(u) \sim -\log u$ .

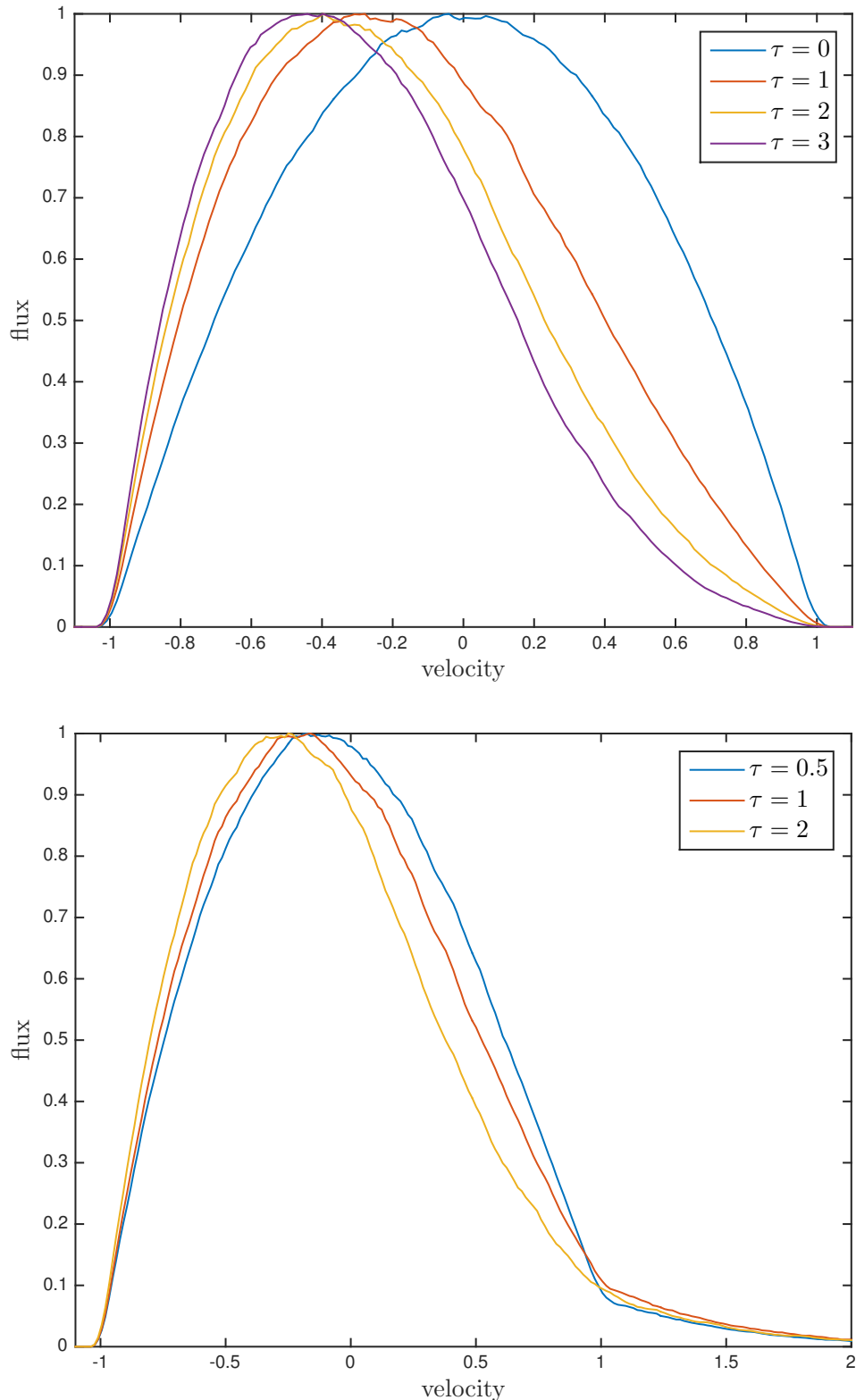


**Figure 3.2.** Benchmark models for line profiles with  $v \propto r$ ,  $i(r) \propto \text{constant}$  and a filled sphere with  $R_{in}/R_{out} = 0$ . Pure dust absorption models ( $\omega = 0$ ) are presented in the top plot, whilst partially scattering models are presented at the bottom ( $\omega = 0.6$ ) as per ? Models II and III. All resulting profiles have been scaled to unity flux at their peaks.

Setting  $i(r) \propto r^{-2\beta}$  (for a recombination or collisionally excited line emitted from a medium with an assumed density profile for the emitter  $\rho \propto r^{-\beta}$ ) then gives

$$\begin{aligned} i(v) dv &\sim \frac{dv}{\alpha v^{\frac{2\beta-3+\alpha}{\alpha}}} \int_{\theta_0}^{\theta_1} \cos^{\frac{2\beta-3}{\alpha}} \theta \sin \theta d\theta \\ &\sim \frac{dv}{v^{\frac{2\beta-3+\alpha}{\alpha}}} \left[ \frac{\cos^{\frac{2\beta-3+\alpha}{\alpha}} \theta}{2\beta - 3 + \alpha} \right]_{\theta_0}^{\theta_1} \end{aligned} \quad (3.2)$$

for  $\frac{2\beta-3}{\alpha} \neq -1$  where  $i(v) dv$  is the energy emitted in a volume element and  $\theta_0$  and  $\theta_1$  are the bounds of this element. The case  $\frac{2\beta-3}{\alpha} = -1$  results in a logarithmic relationship.

In the case of a “complete” nebula, i.e. one where the inner radius is vanishingly small in comparison to the outer radius, we obtain

$$i(v) dv \sim \pm \frac{du}{(2\beta - 3 + \alpha) v^{\frac{2\beta-1+\alpha}{\alpha}}} \left( 1 - v^{\frac{2\beta-3+\alpha}{\alpha}} \right) \quad (3.3)$$

If the nebula is not “complete”, that is to say, the inner radius is some fraction of the outer radius and the remnant is a detached shell, the above formula becomes valid only from  $v = 1$  to some critical value  $v' = q^\alpha$ . For  $v < v'$ , we obtain

$$i(v) dv \sim \pm \frac{dv}{(2\beta - 3 + \alpha)} \left( \frac{1}{q^\alpha} - 1 \right) \quad (3.4)$$

and therefore the top of the line is flat while the sides are sloping.

Crucially, the width of the flat section is determined by  $v' = q^\alpha$  or simply  $v' = q$  in the case where  $v \propto r$ , whilst the shape of the profile outside of the flattop is described by equation 3.3.

Profiles with a variety of shapes may be derived from these formulae depending on the relative values of  $\alpha$  and  $\beta$ . Here we consider three main families of curves:

1.  $i(v) \sim v^{-\gamma} - 1 \quad (\alpha > 0, 2\beta - 3 + \alpha > 0)$
2.  $i(v) \sim 1 - v^\gamma \quad (\alpha > 0, 2\beta - 3 + \alpha < 0)$
3.  $i(v) \sim -\log v \quad (\alpha > 0, 2\beta - 3 + \alpha = 0)$

where  $\gamma$  is defined as  $\gamma = |\frac{2\beta-3+\alpha}{\alpha}|$ .

Models are presented for each of these cases, both for a complete nebula and for a shell structure with  $R_{in}/R_{out} = 0.2$ . A velocity profile  $v \propto r$  appropriate for supernova ejecta in the free expansion phase is used throughout. Values of  $\beta = 0, 1$  and  $2$  are adopted. Figure 3.1 illustrates the excellent agreement between the analytical case and the models. All fluxes are scaled to unity at the peak.

## 3.2 The line profile models of ?

In addition to the tests for optically thin lines described above, we also compared our outputs to those derived by ? in order to assess the accuracy of the scattering and absorption aspects of the code. We consider two similar cases, equivalent to Models II and III of ?. In the first case, dust with zero albedo is uniformly distributed throughout a completely filled nebula with a velocity profile  $v \propto r$ . In the second case, the same scenario is considered but a medium of dust with albedo  $\omega = 0.6$  is considered.

In the first case, the profile may once again be derived analytically from the basic geometry using the fact that radiation will be attenuated by a factor  $e^{-2\tau_\nu v}$  between points with line of sight fractional velocities  $-v$  and  $+v$  where  $\tau_\nu$  is optical depth at frequency  $\nu$  from the centre to the outer edge of the ejecta. The line profile is therefore given by

$$\frac{I(v)}{I(-v)} = \exp(-2\tau_\nu v) \quad (3.5)$$

? presented several examples for both the analytical case of the perfect absorber and a Monte Carlo model for grains with  $\omega = 0.6$ . We present the same cases in Figure 3.2 and note that the resulting profiles exhibit the same features and shape. Of particular interest is the scattering wing that appears beyond the maximum velocity ( $v_{max} = 1$ ) on the red side of profiles in the case of the partial scatterer, as a result of the packets doing work on the expanding sphere. This was noted by ? as a potential diagnostic for the presence of dust in the ejecta of a supernova and we will discuss this further in Section ??.

## 3.3 Testing the electron scattering mechanism

## 3.4 Clumped models in smooth limits

This page was intentionally left blank

## Chapter 4

---

# Parameter Sensitivity

It is of general interest to establish potential diagnostic signatures in the line profiles of supernovae and their remnants in order to trace dust formation more effectively. The capacity to specify a number of parameters is included in Damocles. The variation of each parameter potentially affects the contour of the resulting line profile in a different way. By investigating each parameter separately over a range of values, it may be possible to identify certain characteristics of dust-affected line profiles that may be associated with a particular property of the dusty medium. This insight could help to explain unusual or interesting features of observed line profiles where dust is suspected to be an influential factor. In this chapter, I investigate and discuss the effects of the main parameters of interest, namely:

- the maximum velocity,  $V_{max}$
- the ejecta radius ratio,  $R_{in}/R_{out}$
- the dust optical depth,  $\tau$
- the dust albedo,  $\omega$
- the dust density profile exponent,  $\beta$ , where  $\rho \propto r^{-\beta}$

I also investigate the capacity of this type of model to infer properties of the dust itself, specifically the size of dust grains and any size distribution that may be discernible, and the composition of the dusty medium as made up of a number of species.

## 4.1 The maximum line velocity, $V_{max}$

The maximum velocity is defined as the velocity at the outer edge of the line emitting region for a given line. The maximum velocity may vary between different spectral lines or doublets due to different locations of species with differing ionization thresholds. Clearly, the larger the maximum velocity used the wider the profile becomes. To some extent therefore the steepness of the density profile and the maximum velocity can act to counter each other since a steeper density profile narrows the profile (see Section 4.5). The shape of the wings of the profiles, however, generally preclude much degeneracy in this aspect - the overall shape of the line profile can be used to determine the exponent of the density profile to within a relatively small range.

More important is the effect that the maximum velocity has on the overall optical depth. Since the overall volume of the ejecta is determined solely by the maximum velocity and the ratio of the inner and outer radii, the total optical depth to which the radiation is exposed can be greatly affected by even a relatively small change in the maximum velocity. Practically speaking, the maximum velocity can usually be fairly well determined from the observations (identified as the point where the flux vanishes on the blue side) and may be further constrained through modelling.

## 4.2 The ejecta radius ratio, $R_{in}/R_{out}$

As already discussed in Section 3.1, the width of the flat top is determined solely by the ratio of the inner and outer radii, the exponent of the velocity profile and the maximum velocity. Throughout my sensitivity analysis of parameter space, I assume that the velocity profile takes the form  $v \propto r$  despite it being a variable parameter in the code. This is the case for all supernovae from just a few months after the initial explosion (and therefore likely well before the epoch of the onset of dust formation) since the ejecta is in free expansion. This is discussed in further detail in Section 4.10. For this case,  $R_{in}/R_{out}$  is given by

$$\frac{R_{in}}{R_{out}} = \frac{V_{min}}{V_{max}} \tag{4.1}$$

where it is often possible to constrain  $V_{min}$  and  $V_{max}$  to a relatively narrow range simply

from the observed line profile by identifying the velocity at which the flux goes to zero on the blue side ( $V_{max}$ ) and the velocity at which the profile starts to flatten off, also on the blue side ( $V_{min}$ ).

The majority of spectral lines emitted from supernovae and supernova remnants are expected to have a flat top before dust attenuation effects since it is rare for these objects to form a completely filled nebula. However, even a very small amount of dust attenuation may result in the line profile appearing to be smoothed at its peak.

The effect of varying the ratio of the inner and outer radii is derived analytically in Chapter 2 and presented for a number of emissivity profiles in Figure 3.1. All profiles have been scaled to unity flux at their peaks.

### 4.3 The dust optical depth, $\tau$

The effects of dust optical depth on the line profile produced by Damocles are in essence the same in the case of both a detached shell and a complete nebula. However, due to the increased complexity of the original profile in the case of the detached shell, a number of slightly more interesting effects are observed in these models and we discuss these first. I then go on to discuss the case of a complete nebula where the effects observed are very similar to those seen in models with high dust optical depth in the detached shell case.

#### 4.3.1 The detached shell case

As expected, in cases of non-zero dust optical depth, greater attenuation of the original line profile on the red side is exhibited. This is illustrated in two panels of profiles in Figures 4.1 and 4.2. The profiles are most revealing at lower dust optical depths. The effects of the asymmetric absorption can be seen in different sections of the profiles. The region of the profile that is most clearly affected by dust absorption is the flat-topped region. A small amount of absorption in this region results in a skewed profile, with a fraction of the flat-topped section removed. The peak becomes blue-shifted as a result, but only to the original value of  $-V_{min}$ , the minimum velocity corresponding to  $R_{in}$ . In addition to the attenuation in this region, the red wing of the profile is also somewhat reduced, and the blue wing somewhat increased relative to their original symmetric positions. The result is a relatively “jagged” looking profile, often with sharp changes at  $\pm V_{min}$ . The profile is generally asymmetric, although the degree of absorption in the flat-topped region may

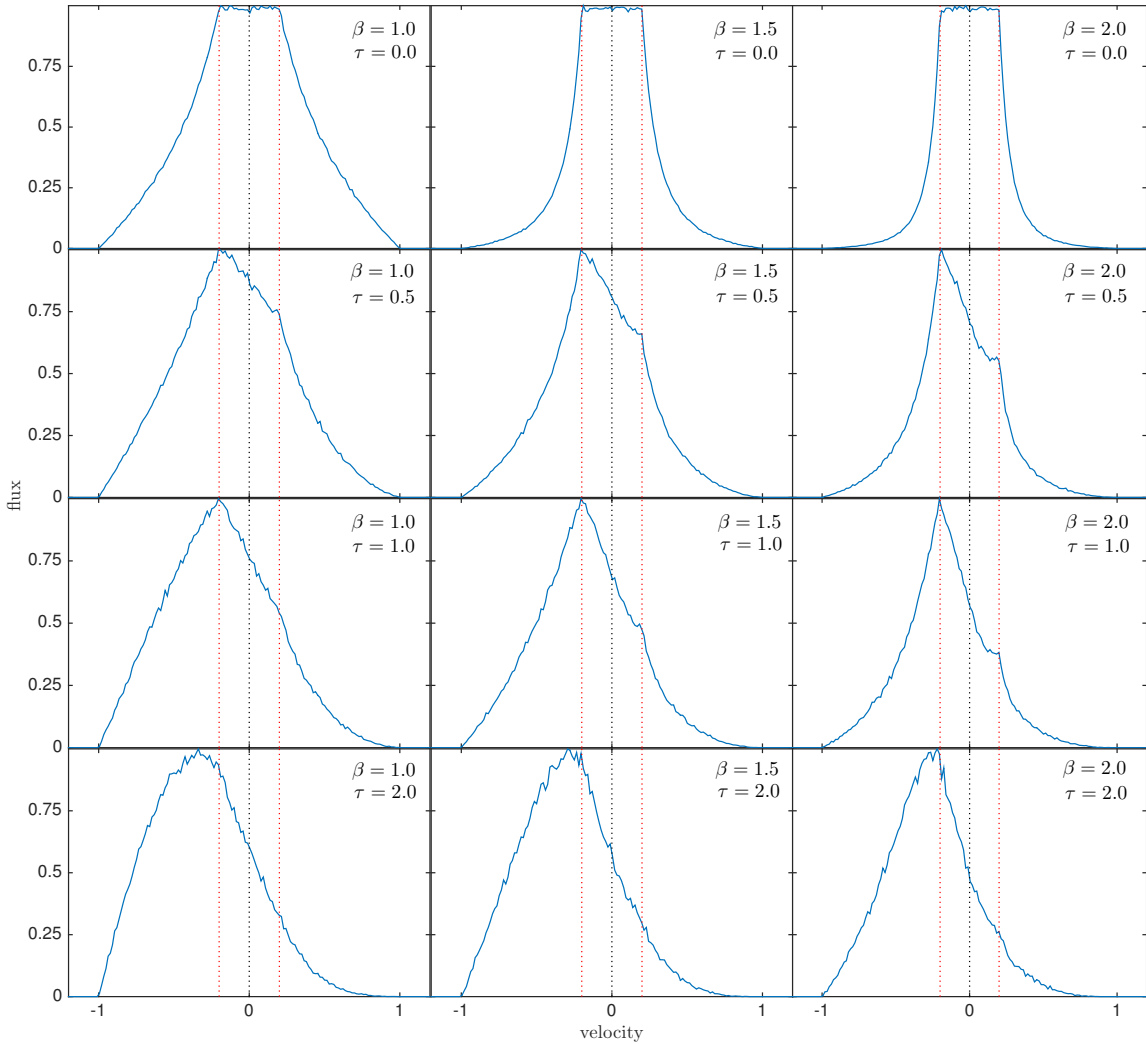


**Figure 4.1.** Set of models with  $i(r) \propto r^{-2\beta}$  for  $\beta = 1.0$  (left),  $\beta = 1.5$  (middle) or  $\beta = 2.0$  (right),  $\omega = 0$ ,  $R_{in}/R_{out} = 0.2$ ,  $v(r) \propto r$  and  $v_{max} = 1$  illustrating the effects of varying  $\tau$ . Peak fluxes are scaled to unity.

sometimes make it seem as though the profile is in fact symmetric and uniformly blue-shifted (see Section 4.7 for further discussion).

At high dust optical depths the entire profile is shifted to the blue and the peak moves beyond  $-V_{min}$  further into the blue. The profiles also become more smooth. A set of models showing the effects of varying optical depths for different density profiles and dust albedos are presented in Figures 4.1 and 4.2.

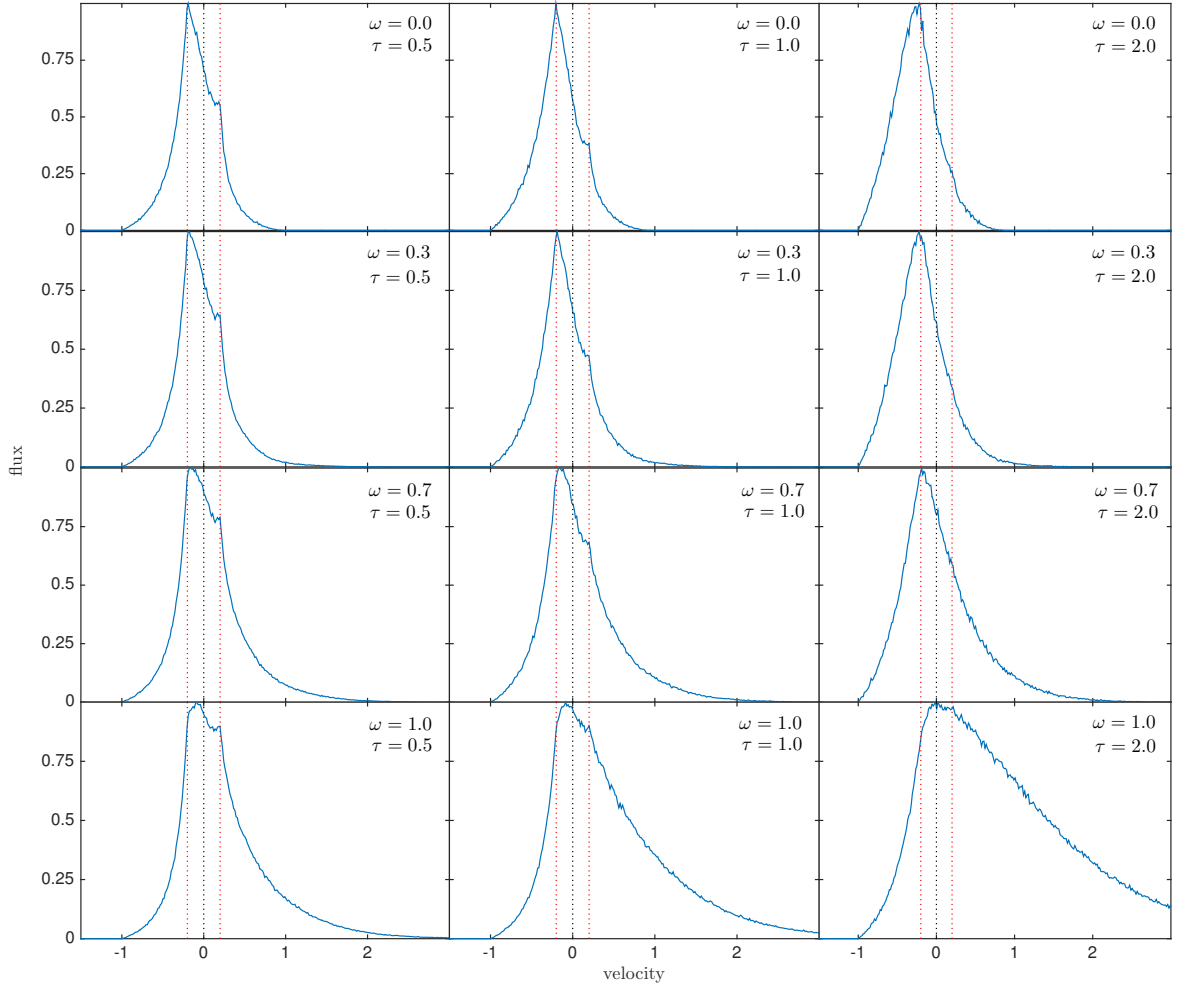


**Figure 4.2.** Set of models with  $i(r) \propto r^{-4}$  (i.e.  $\beta = 2.0$ ),  $R_{in}/R_{out} = 0.2$ ,  $v(r) \propto r$  and  $v_{max} = 1$  illustrating the effects of varying  $\tau$  and  $\omega$ . Peak fluxes are scaled to unity.

### 4.3.2 The complete nebula case

To reproduce similar characteristic dust-affected line profiles where the peak of the profile is shifted beyond  $-V_{min}$  into the blue is “easier” for smaller values of  $V_{min}$ . The complete nebula is therefore effectively analogous to cases of higher optical depths for a detached shell and the same effects that are illustrated in Figures 4.1 and 4.2 apply.

## 4.4 The dust albedo, $\omega$

In the past, there has largely been a focus on the effects of absorption by dust on the shapes of line profiles and less attention has been paid to the potential effects of scattering by dust. In fact, line profiles can be significantly affected by scattering of radiation. Not

only does repeated scattering of photons increase the number of potential opportunities for a given photon to be absorbed but it also results in continuous shifting of the frequency of the photon to the red. The photon must do work on the expanding shell of dust in order to escape and thus many of the photons are reprocessed beyond the theoretical maximum velocity on the red side of the profile. The result can be a substantial, extended wing on the red side of the line. In the case of strong dust scattering, this can result in an asymmetric profile that is the opposite of that normally expected with the majority of the emission on the *red* side. The peak however, remains blue-shifted (see the bottom right panel on Figure 4.2 as an example). For the line profile to exhibit this feature requires the dust to be a nearly perfect scatterer and it is therefore unlikely that profiles of this sort will be frequently observed. See Figure 4.2 for a fuller illustration of the variation with  $\omega$  and  $\tau$ .

The implications of this result in relation to the use of line profiles as a diagnostic for tracing dust formation in supernova ejecta are discussed further in Section 4.7.

## 4.5 The dust density profile, $\rho \propto r^{-2\beta}$

Whilst the density profile of the dust may have some effect on the resulting profiles, it is the initial emissivity profile (dependent on the dust density profile) that has greatest effect on the resulting shape of the line profile.

In general, the steeper the emissivity distribution, the narrower the line profile becomes. The sides of the line profile may become almost straight for a very steep distribution since the majority of the emission then comes from a very narrow velocity range. For a flat-topped profile of fixed width this approximates the square profile produced in the case of an emitting shell with constant velocity.

The dependence of the shape of the line profile in the optically thin dust case is described in Section 3.1. However, the density profile also plays a significant role where there is even a small amount of absorption. As previously discussed, at relatively small optical depths, a section of the flat-topped region is removed resulting in a peak at  $-V_{min}$ . The shape of the profile in this region is significantly affected by the density profile. Shallow density profiles (low  $\beta$ ) produce a virtually linear variation in flux between  $-V_{min}$  and  $+V_{min}$ . For a fixed dust optical depth, the steeper the distribution becomes, the more concave the profile becomes between  $-V_{min}$  and  $+V_{min}$ , ultimately resulting in a clear

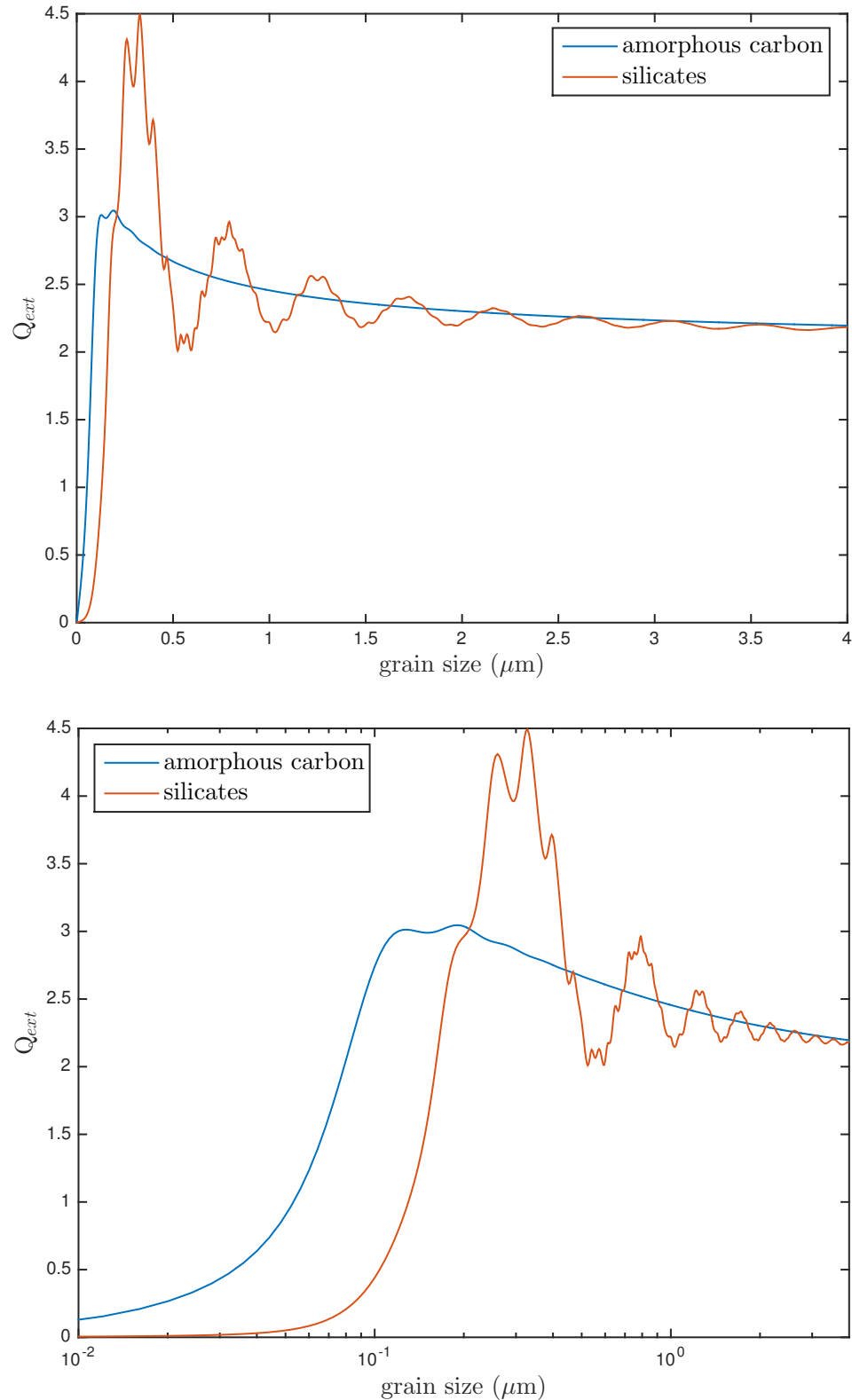


**Figure 4.3.** Variation of extinction efficiency ( $Q_{ext}$ ) with grain size for amorphous carbon and silicates using Mie theory at  $\lambda = 658\mu\text{m}$ . Optical constants are from Zubko et al. (1996) and Draine & Lee (1984). A linear scale is presented on the top and a log scale on the bottom.

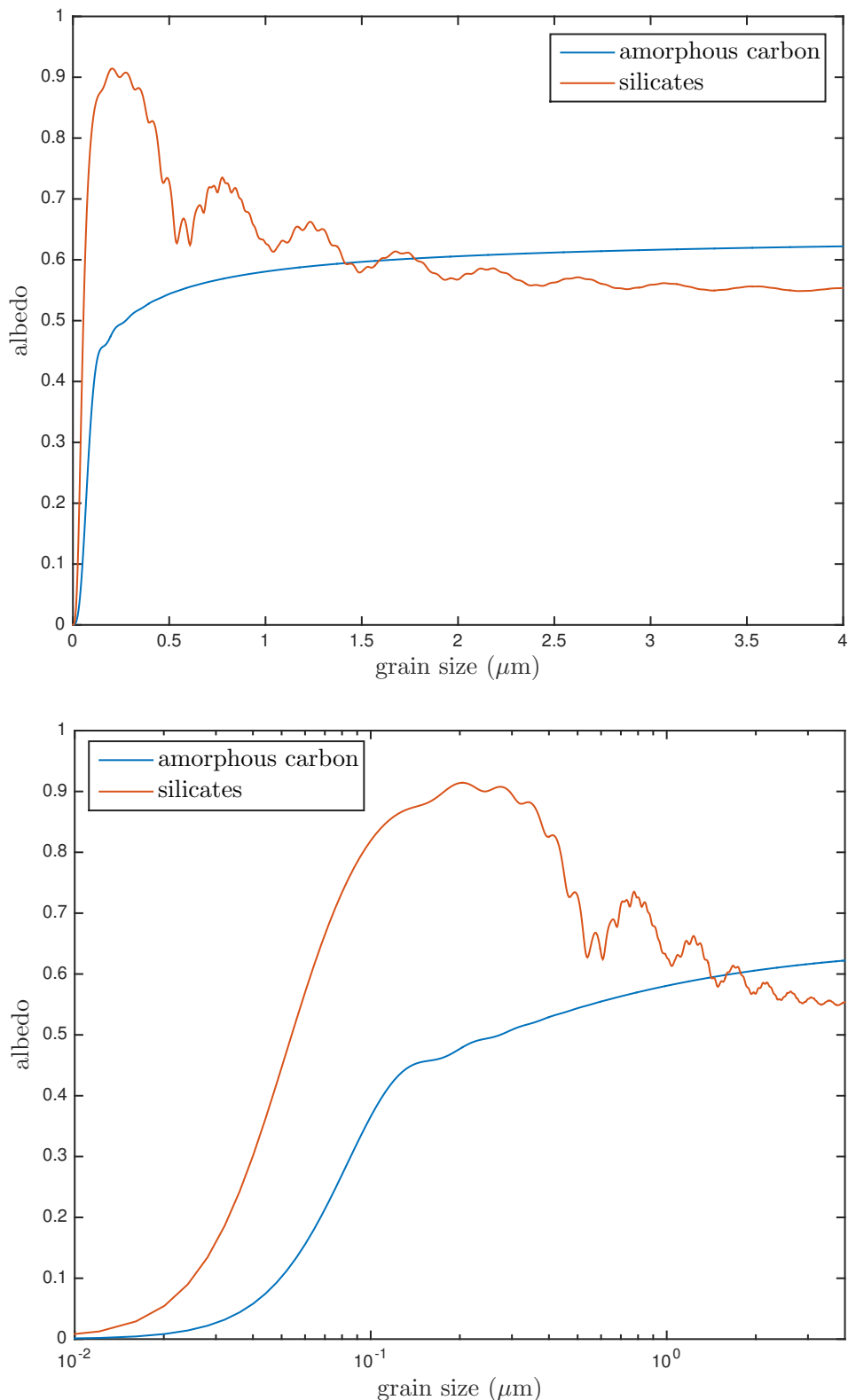


**Figure 4.4.** Variation of albedo with grain size for amorphous carbon and silicates using Mie theory at  $\lambda = 658\mu\text{m}$ . Optical constants are from Zubko et al. (1996) and Draine & Lee (1984). A linear scale is presented on the top and a log scale on the bottom.

shoulder to the profile at  $+V_{min}$ . For extremely steep density distributions this can result in a double peaked profile with trough to the red of  $V = 0$ . A illustration of the effects of variation of  $\beta$  with  $\tau$  on the profiles is shown in Figure 4.1.

## 4.6 Inferring properties of the dust from the models

The presence of an extended red wing at large positive velocities in combination with increased extinction on the red side at smaller positive velocities can allow the values of  $\tau$  and  $\omega$  to be well constrained. In this case it is possible to translate these values into a dust mass and average grain size respectively for a given species or combination of species using optical properties and Mie theory (see Figures 4.3 and 4.4). In fact, it is the dust mass and average grain size that is varied within the code for a specified species or combination of species i.e. the dust optical depth and grain size are not varied directly. It is therefore important to note that the use of different optical properties may substantially alter the inferred optical depths and albedos for a given species of specific grain size as has been noted previously (e.g. Owen & Barlow (2015)).

For amorphous carbon, the larger the grain size used the larger the albedo and the smaller the cross-section of absorption. Larger masses of dust are therefore required to fit the same degree of absorption if a larger grain size is used. This is in contrast to SED radiative transfer modelling where larger grain sizes generally result in less dust being required to fit the IR portion of the SED (W15). These two techniques in tandem may therefore give excellent limits on grain sizes for different species or combinations thereof.

## 4.7 Observable signatures of dust in line profiles

The greater the dust optical depth, the more attenuation of the line is observed. As expected, the red side of the profile suffers a greater degree of absorption than the blue side. The resulting asymmetry is somewhat more complex than perhaps previously thought however. Dust has repeatedly been cited as the agent responsible for the apparent blue-shifting of line profiles in supernovae in the manner of the profiles presented in Figure 3.2. That is, relatively high optical depths result in an overall shift of the entire profile towards the blue.

In practice a relatively large optical depth ( $\tau \approx 2$ ) is required to actively shift the peak of the profile bluewards of its natural  $V_{min}$  value corresponding to the velocity at the inner

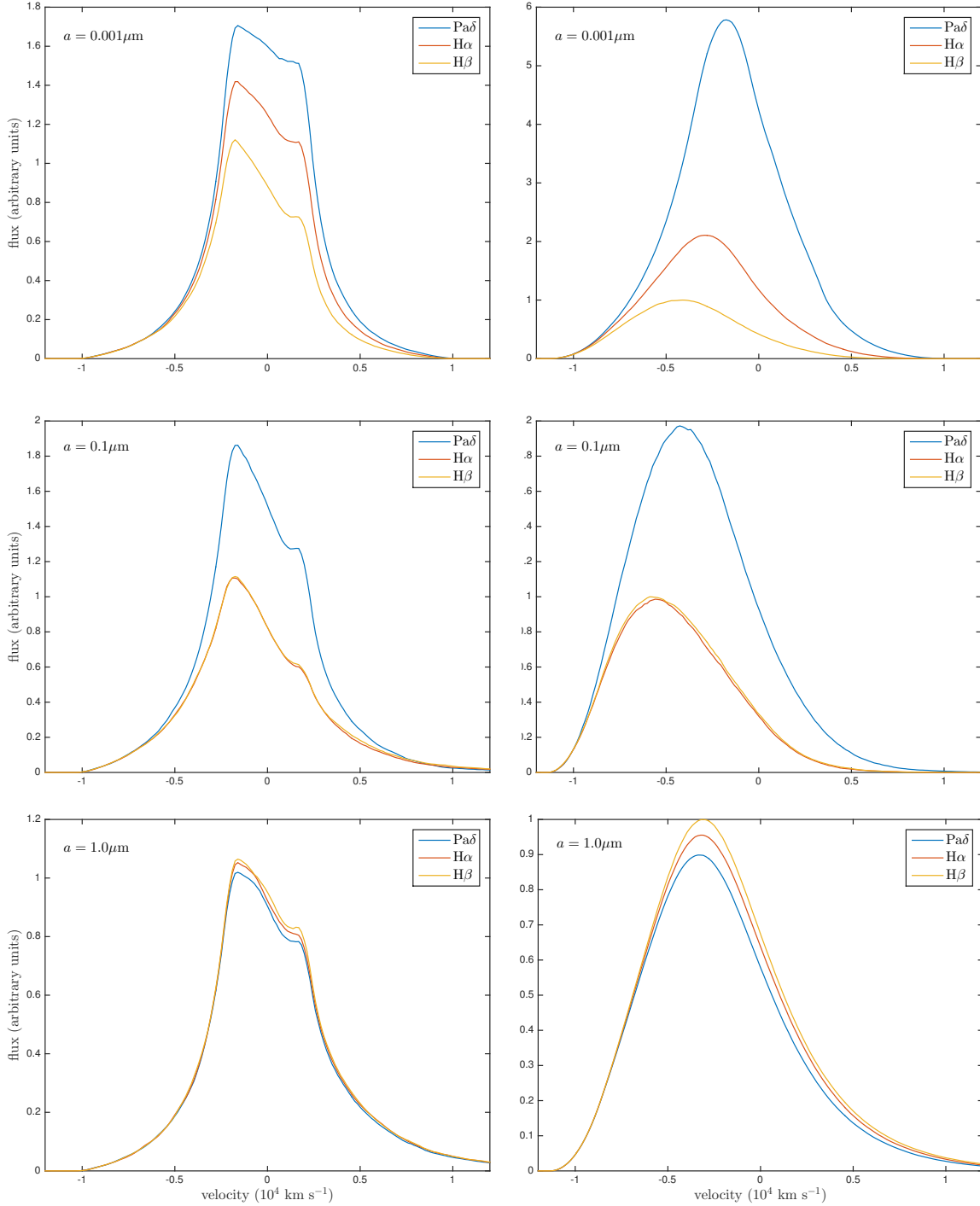


**Figure 4.5.** Model line profiles for H $\alpha$  (6563Å in red), H $\beta$  (4861Å in yellow) and Pa $\delta$  (10049Å in blue) for optically thin and optically thick cases on the left-hand side and right-hand side respectively. All models adopted density profile  $\rho(r) \propto r^{-4}$  (i.e.  $\beta = 2$ ), velocity profiles  $v(r) \propto r$  and radii ratio  $R_{in}/R_{out} = 0.2$ . The grain radii used were  $a = 0.001 \mu\text{m}$  (top),  $a = 0.1 \mu\text{m}$  (middle) and  $a = 1.0 \mu\text{m}$  (bottom). All the above models used amorphous carbon.

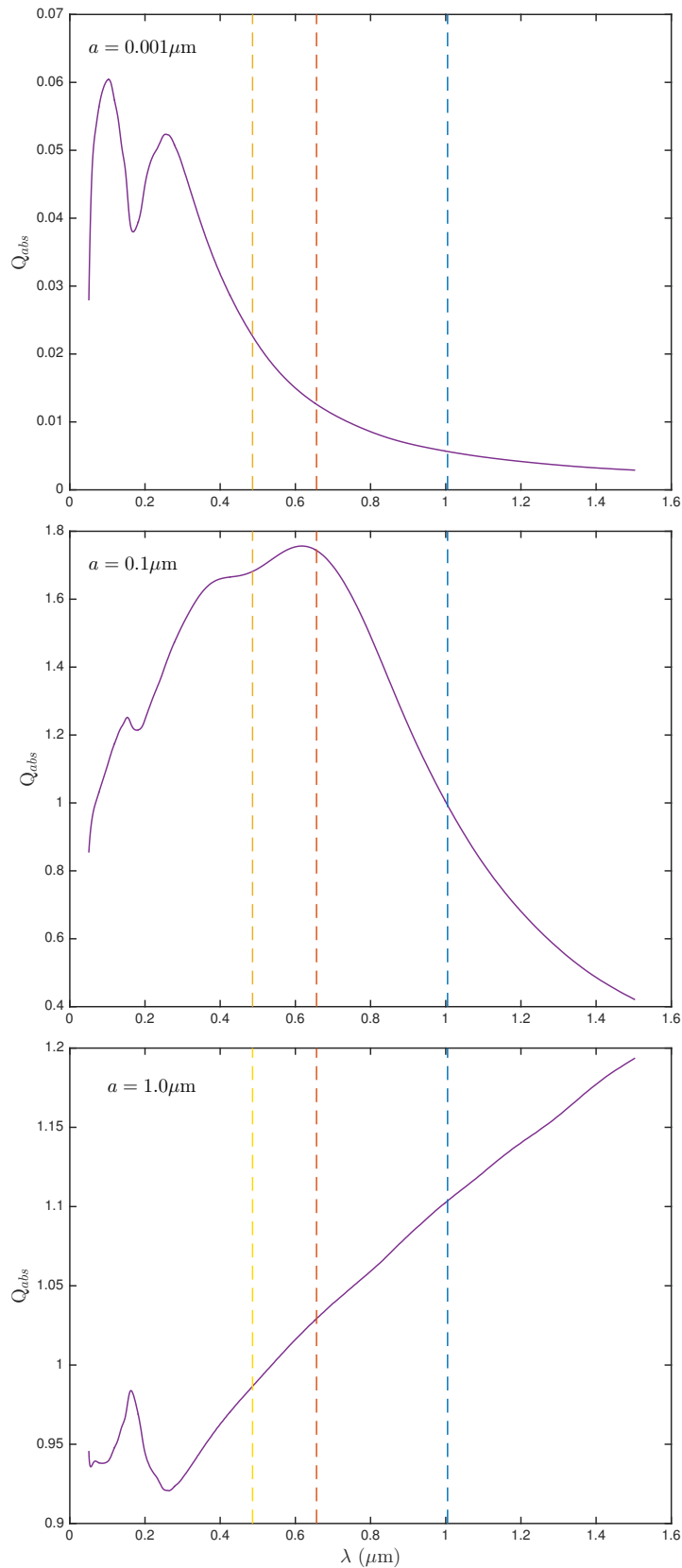


**Figure 4.6.** The variation of amorphous carbon dust absorption efficiency with grain size. The grain radii plotted are  $a = 0.001 \mu\text{m}$  (top),  $a = 0.1 \mu\text{m}$  (middle) and  $a = 1.0 \mu\text{m}$  (bottom). The vertical lines mark the wavelengths of H $\alpha$  (6563Å in red), H $\beta$  (4861Å in yellow) and Pa $\delta$  (10049Å in blue).

radius of the shell. In most cases it seems more likely that the dust may not be optically thick and the blue-shifting of the peak of the profile is likely a result of attenuation in the flat-topped section (close to  $R_{in}$ ). The peak would therefore tend to be located at  $-V_{min}$ .

Since dust absorption is wavelength dependent for  $2\pi a < \lambda$ , one might expect the position of the peak flux to be dependent on the wavelength of the line being considered. The relationship between the locations of the peaks of profiles and their wavelength has been discussed by several authors in relation to dust formation (Smith et al. 2012; Fransson et al. 2013; Gall et al. 2014). Whilst this may occur in cases of high dust optical depth, this is not necessarily likely to be seen in the ejecta of most supernovae. The wavelength-dependence of dust absorption instead can result in differing degrees of extinction in the flat-topped region of each profile but still leave the peak at its blue-shifted position of  $-V_{min}$ . Of course, the value of  $V_{min}$  may be different for different species. However, if this is the case then there would be no reason to expect a variation in the position of the peak of profiles to be correlated with the wavelength dependence of dust. Rather one would expect it potentially to trace the location of different ions within the ejecta. However, for lines from the same ion, for example the Balmer and Paschen lines of HI, we might expect to see peaks at the same position but differing degrees of absorption. At high resolutions, it might be possible to detect differences in the shape of the line profiles, particularly between  $-V_{min}$  and  $+V_{min}$  where the steepness of the incline traces the degree of dust absorption. This can be seen in Figure 4.5 where we illustrate the effects of the wavelength dependence of dust absorption for three lines, H $\alpha$  (6563Å), H $\beta$  (4861Å) and Pa $\delta$  (10049Å). All lines were modelled using three different grain sizes and in both optically thin and thick cases. We also show the variation of the absorption cross-section with wavelength at three different grain sizes in Figure 4.6.

The attenuation of the flat-topped region is often such that it can be hard to discern a difference in slope between the attenuated section between  $-V_{min}$  and  $+V_{min}$  and the slope of the wing for  $V > +V_{min}$ , particularly in circumstances where data is of poor resolution or has a poor signal-to-noise ratio. Even in the case of excellent data, it may be easy to overlook these particular features or to dismiss them as natural fluctuations in the geometry of the ejecta rather than that they may be a product of dust absorption effects.

The greater attenuation of radiation received from the receding portion of the ejecta results in an asymmetry of the line profile whereby the majority of the observed emission is located bluewards of the peak. However, the effects of repeated dust scattering events

within the ejecta can serve to counter this asymmetry. Even in the case of dust grains with a relatively low albedo, a surprisingly persistent wing on the red side of the profile is seen beyond the maximum theoretical velocity of the emitting region. For higher albedos this can actively result in a shift in the overall asymmetry of the profile, with the majority of the emission being emitted redwards of the peak, though the peak itself remains blue-shifted.

This effect is obviously analogous to that of electron scattering which also produces a significant red wing in line profiles (Hillier 1991; ?). This is an important consideration in both modelling and analysis of spectral line profiles. DAMOCLES has the capacity to include a basic electron scattering mechanism in order to assess the possibility that any observed red wing might be produced by electron scattering rather than dust scattering. The red wing observed in line profiles is an excellent diagnostic for determining the overall dust albedo and it is therefore important to establish whether this feature is due to electron or dust scattering or a combination of the two.

The combination of relatively low optical depths, initially flat-topped profiles, greater attenuation on the blue side with increased flux on the red side due to scattering can result in a profile that ends up appearing almost symmetrical, particularly if contaminants, such as narrow lines or blending with other broad lines, are present or if the resolution of the data is low. The potential for apparently symmetrical profiles that appear to have been uniformly blue-shifted should be noted (see Figures 4.1 and 4.2 for examples of this).

## 4.8 The effect of a grain size distribution

It is important to consider the potential effect on the dust mass of modelling a grain size distribution instead of a single grain size. For a grain size distribution the overall extinction cross section,  $C_{ext}$ , at a given wavelength is calculated as

$$C_{ext} = \int_{a_{min}}^{a_{max}} Q_{ext}(a)n(a)\pi a^2 da \quad (4.2)$$

where  $Q_{ext}(a)$  is the extinction efficiency for a grain size  $a$  and  $n(a)$  is the number of grains with size  $a$ . The overall extinction efficiency is then

$$Q_{ext} = \frac{C_{ext}}{\int_{a_{min}}^{a_{max}} n(a) \pi a^2 da} \quad (4.3)$$

The scattering cross-section  $Q_{sca}$  is similarly calculated. As a result of these calculations, there is rarely a single grain size that has the same albedo and extinction efficiency as a size distribution. Modelling a size distribution instead of a single grain size may therefore alter the deduced dust mass. Since models are only sensitive to the optical depth and the albedo, however, it is not possible to deduce the grain size range or distribution and only single grain sizes are investigated in the models that are presented in the following chapters.

Whilst this apparently limits the scope of these results, it is important to consider the extent to which considering grain size distributions would alter the derived dust masses. By considering a number of grain size ranges and adopting a power law distribution with a variable exponent, we may gain some insight into the effects of adopting a distribution rather than a single size. For the classical MRN power law ( $n(a) \propto a^{-3.5}$ ) with a wide grain size range ( $a_{min} = 0.001\mu\text{m}$  to  $a_{max} = 4.0\mu\text{m}$ ) the derived albedo of  $\omega = 0.001$  is much too small to reproduce the required wing seen at early epochs. We investigate this issue by adjusting the exponent of a distribution for a number of grain size ranges until the overall albedo is the same as that seen for the best fitting single grain size. We can then approximately calculate the required dust mass for a distribution of grain sizes from the properties of a single-size model by equating the optical depths. The optical depth for a single grain size is proportional to

$$\tau \propto Q_{ext}(a)\sigma(a)n_d \quad (4.4)$$

where  $n_d$  is the number density of dust grains,  $\sigma(a)$  is the cross-sectional area of a grain of radius  $a$  and  $Q_{ext}(a)$  is the extinction efficiency for a grain of radius  $a$ . On average, this gives

$$\tau \propto \frac{Q_{ext}(a)M\pi a^2}{\frac{4}{3}\pi a^3\rho V} \quad (4.5)$$

for a total dust mass  $M$ , total volume of the ejecta  $V$  and density of a dust grain  $\rho$ .

This simplifies to

$$\tau \propto \frac{Q_{ext}(a)M}{\frac{4}{3}a\rho V} \quad (4.6)$$

$$M_d = \frac{M_s Q_{ext,s}(a_s)}{a_s} \times \frac{\int_{a_{min}}^{a_{max}} n(a)a^3 da}{\int_{a_{min}}^{a_{max}} Q_{ext}(a)n(a)a^2 da} \quad (4.7)$$

where the subscript  $s$  represents the single grain size quantities and the subscript  $d$  represents quantities for the grain size distribution. This is only calculable for a specific wavelength and is therefore only an approximate conversion when performed at the rest-frame wavelength of the line in question. However, practically, the variation of extinction efficiency and albedo over the narrow wavelength ranges modelled within the code is not significant and so this method produces relatively accurate dust masses (as determined by running models with the new parameters).

## 4.9 The effect of different species

In the majority of the modelling that follows, a single species, amorphous carbon, is considered. A single species is used since the parameters that affect the quantity of dust required in the model are the albedo and the optical depth. There are therefore likely many possible combinations of species that may result in a good fit to the data. The choice of amorphous carbon is partly motivated by evidence that, for SN 1987A (which, as an incredibly well-observed and relatively typical core-collapse supernova, is an excellent test case) the fraction of silicates present in the dusty ejecta is limited to approximately 15% (W15, Ercolano, Barlow & Sugerman (2007)). It is also motivated by previously published SED models which generally employ amorphous carbon. This is because SED models frequently require far larger masses of silicate dust than amorphous carbon dust in order to produce similar levels of infrared flux and therefore amorphous carbon models are likely to produce the more conservative dust mass estimates. By modelling with amorphous carbon we may compare directly to these models where possible.

We consider the change in dust mass when a medium of 100% silicates is used instead

**Table 4.1.** Equivalent dust masses for the day 714 clumped models using grain size distributions and 100% amorphous carbon.  $f$  is factor of increase from the dust mass for the single size model ( $M = 7 \times 10^{-5} M_{\odot}$  with  $a = 0.6\mu\text{m}$ ) and  $p$  is the exponent of the grain size distribution  $n(a) \propto a^{-p}$ .

<i>carbon</i>			<i>silicates</i>		
<i>a</i>	$Q_{ext}$	<i>a</i>	$Q_{ext}$	$f = M_{sil}/M_{amc}$	
0.6	2.60633	0.0583	0.0772	5.37	
0.6	2.60633	4	2.1828	13	
3.5	2.2129	0.0641	0.10182	0.65	
3.5	2.2129	1.02	2.149	0.49	
3.5	2.2129	1.376	2.3514	0.61	

of amorphous carbon. We use optical constants presented in Draine & Lee (1984). In a similar manner to the approach detailed in Section 4.8, we may calculate the mass of silicates that is equivalent to a carbon mass for a single grain size. We consider the albedo at the original grain size, calculate the equivalent grain size for silicates that results in the same albedo and then calculate the new dust mass by considering the change in the extinction efficiency as

$$M_{sil} = M_{amc} \left( \frac{Q_{amc}}{Q_{sil}} \right) \left( \frac{a_{sil}}{a_{amc}} \right) \left( \frac{\rho_{sil}}{\rho_{amC}} \right) \quad (4.8)$$

Because of the nature of the variation of albedo with grain size for silicates (see Figure 4.4), there is often more than one silicate grain size that will give rise to the same albedo. We consider all the possibilities and the resulting mass conversion factors in Table 4.1. In our best fitting models for days 714 and 806, using any fraction of silicates of either grain size would serve to increase the dust mass. However, at later epochs, using some fraction of silicate dust would reduce the dust mass to potentially more than half of our estimated values. However, this is still within our predicted range and our minimum and maximum dust masses remain robust.

## 4.10 The velocity distribution

# Chapter 5

---

## SN 1987A

*QUOTE GOES HERE*

AUTHOR

### 5.1 Spectral Observations of SN 1987A

SN 1987A has been the most intensively observed supernova in history, with a wealth of both spectral and photometric data available to model. From the archives of a number of different telescopes we have collated optical spectra acquired over a wide range of epochs. At the earlier epochs we use spectra obtained with the Anglo-Australian Telescope (AAT) and Cerro Tololo Inter-American Observatory (CTIO) and at later epochs we use spectra from the archives of the Hubble Space Telescope (HST) and Very Large Telescope (VLT). An explosion date of 23 February 1987 is adopted throughout and epochs are measured relative to this date. Full details of all observations may be found in Table 5.1. The spectral resolutions of the grating spectrograph observations are listed in column 7, while column 8 lists the spectral resolving powers of the echelle spectrograph observations.

Wavelength ranges encompassing the H $\alpha$  line and [O I]  $\lambda\lambda 6300, 6363$  Å doublet were selected in order to trace their evolution from day 524, near the time of the first indications of dust formation (Wooden et al. 1993) to day 8020, near the current era. Optical spectroscopy obtained at the AAT using the Faint Object Red Spectrograph (FORS) during

**Table 5.1.** Details of the archival data for SN 1987A

Date	Age (days)	Telescope	Inst	$\lambda_{min}$ (Å)	$\lambda_{max}$ (Å)	Res. (Å)	Res. Power	Reference
31 Jul 1988	524	AAT	FORS	5500	10190	20		Spyromilio et al. (1991)
26 Oct 1988	611	AAT	UCLES	6011	7336		30000	Hanuschik et al. (1993); ?
27 Dec 1988	673	AAT	UCLES	5702	10190		30000	Hanuschik et al. (1993); ?
06 Feb 1989	714	CTIO-1.5m	Cass.	6420	10380	16		Phillips et al. (1990)
09 May 1989	806	CTIO-1.5m	Cass.	6430	10330	16		Phillips et al. (1990)
30 Mar 1992	1862	HST	STIS	4569	6818	4.4		Wang et al. (1996)
14 Mar 1993	2211	HST	STIS	4569	6818	4.4		Wang et al. (1996)
07 Jan 1995	2875	HST	STIS	4569	6818	4.4		Chugai et al. (1997)
23 Sep 1996	3500	HST	STIS	4569	6818	4.4		
05 Jan 1997	3604	HST	STIS	4569	6818	4.4		
10 Dec 2000	5039	VLT	UVES	4760	6840		50000	Grönningsson et al. (2006, 2008)
06 Oct 2002	5704	VLT	UVES	4760	6840		50000	Grönningsson et al. (2006, 2008)
21 Mar 2005	6601	VLT	UVES	4760	6840		50000	Grönningsson et al. (2006, 2008)
23 Oct 2007	7547	VLT	UVES	4760	6840		50000	Grönningsson et al. (2007)
07 Feb 2009	8020	VLT	UVES	4800	6800		50000	Tziampzis et al. (2010)

**Table 5.2.** Details of the parameters used for the best fitting smooth models with grain radius  $a = 0.35\mu\text{m}$ .

day	$V_{max}$ (km s $^{-1}$ )	$R_{in}/R_{out}$	$\beta$	$M_{dust}$ ( $M_{\odot}$ )	$a$ ( $\mu\text{m}$ )	$R_{out}$ (cm)	$R_{in}$ (cm)	doublet ratio [O I]	$\tau_{H\alpha}$	$\tau_V$	
H $\alpha$	714	3250	0.25	1.2	2.50E-05	0.35	2.00E+16	5.01E+15		0.61	1.23
H $\alpha$	806	4500	0.25	1.8	3.00E-05	0.35	3.13E+16	7.83E+15		0.30	0.60
H $\alpha$	1862	8500	0.15	1.9	6.00E-04	0.35	1.37E+17	2.05E+16		0.35	0.70
H $\alpha$	2875	9500	0.14	1.9	1.80E-03	0.35	2.36E+17	3.30E+16		0.36	0.72
H $\alpha$	3604	10250	0.13	1.9	5.00E-03	0.35	3.19E+17	4.15E+16		0.55	1.10
[O I]	714	5000	0.17	2.8	9.50E-05	0.35	3.08E+16	5.24E+15	2.9	1.09	2.19
[O I]	806	6000	0.15	2.7	1.60E-04	0.35	4.18E+16	6.27E+15	2.7	0.97	1.95

the first two years after outburst was kindly supplied by Dr Raylee Stathakis (Spyromilio et al. 1991; ?; Hanuschik et al. 1993).

The evolution of the H $\alpha$  line profile is presented in Figures ?? and ???. At later epochs, the broad profile emitted by the ejecta becomes contaminated by narrow line emission from the equatorial ring. These lines have been removed for the purposes of modelling the broad line. A continuum fit has been subtracted from each spectrum and a velocity correction has been applied for a recession velocity of 287 km s $^{-1}$  (Grönningsson et al. 2008).

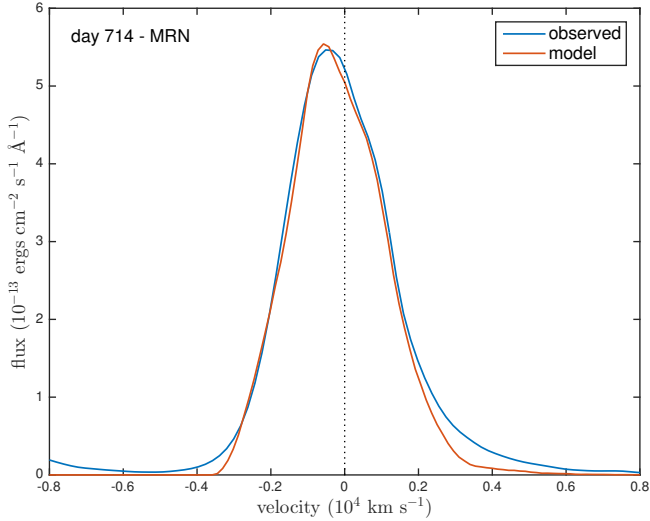


**Figure 5.1.** Conservative dust mass fit to the day 714 H $\alpha$  line of SN 1987A illustrating the underestimation of the red scattering wing for small grain sizes. Model parameters are the same as the conservative fit to day 714 except for the grain size distribution and dust mass:  $V_{max} = 3250 \text{ km s}^{-1}$ ,  $R_{in}/R_{out} = 0.25$ ,  $\beta = 1.2$ ,  $M_{dust} = 8.0 \times 10^{-6} M_{\odot}$ ,  $a_{min} = 0.005 \mu\text{m}$ ,  $a_{max} = 0.25 \mu\text{m}$  and  $n(a) \propto a^{-3.5}$ .

## 5.2 Modelling SN 1987A

We model the H $\alpha$  line of SN 1987A at days 714, 806, 1862, 2875 and 3604 and the [O I]  $\lambda 6300, 6363 \text{ \AA}$  doublet at days 714 and 806. After this epoch the profile begins to become dominated by emission from the reverse shock and the structure of the emitting region may no longer be approximated by a single shell model as we do here (Fransson et al. 2013). We continue to adopt a velocity profile  $V(r) = \frac{V_{max}}{R_{max}}r$  and treat the variable parameters listed in Section ???. Whilst the albedo and optical depth are not varied directly, they are altered by adjusting the dust mass,  $M_{dust}$ , and the grain size,  $a$ , which will together determine the albedo and optical depth via a Mie scattering approximation and the optical properties of the dust.

In all models, the ejecta occupies a shell with inner radius  $R_{in}$  and outer radius  $R_{out}$ . Packets are emitted according to a smooth density profile assuming recombination such that  $i(r) \propto \rho(r)^2 \propto r^{-2\beta}$ . Initially the dust is considered to have a smooth density distribution and is assumed to be coupled to the gas to follow the same radial profile. A clumped distribution of dust is considered later (see Section 5.2.2). We do not include electron scattering in these models since we find that the electron scattering optical depth is not high enough to affect the line profiles in any discernible fashion *references*.

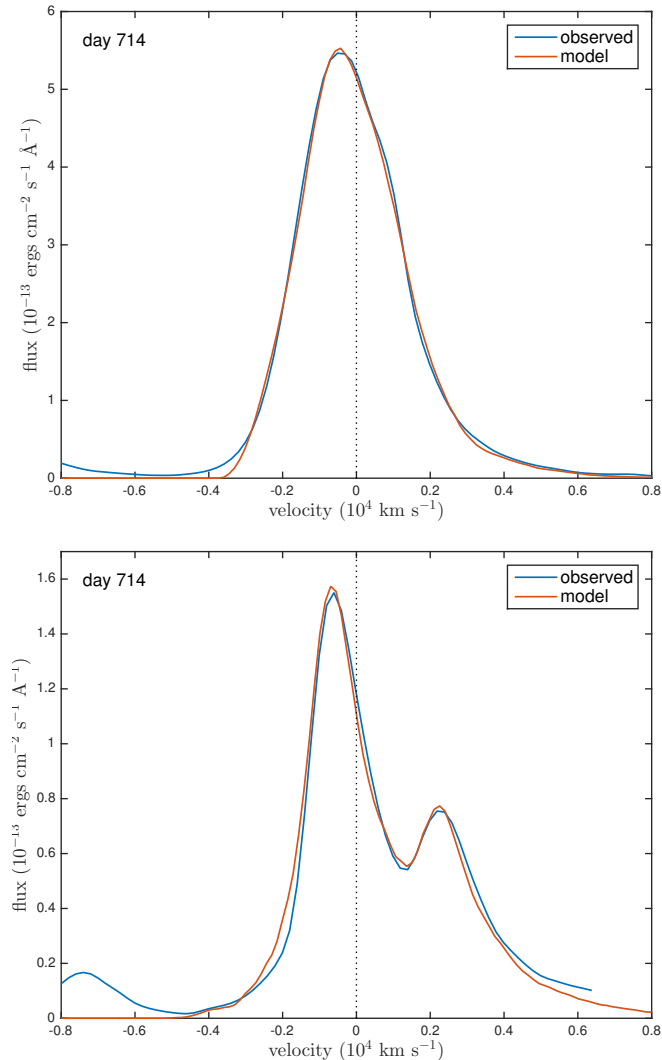


**Figure 5.2.** Best smooth fit to the day 714 H $\alpha$  line (left) and [O I]  $\lambda$ 6300,6363 Å doublet (right) as per parameters detailed in Table 5.2.

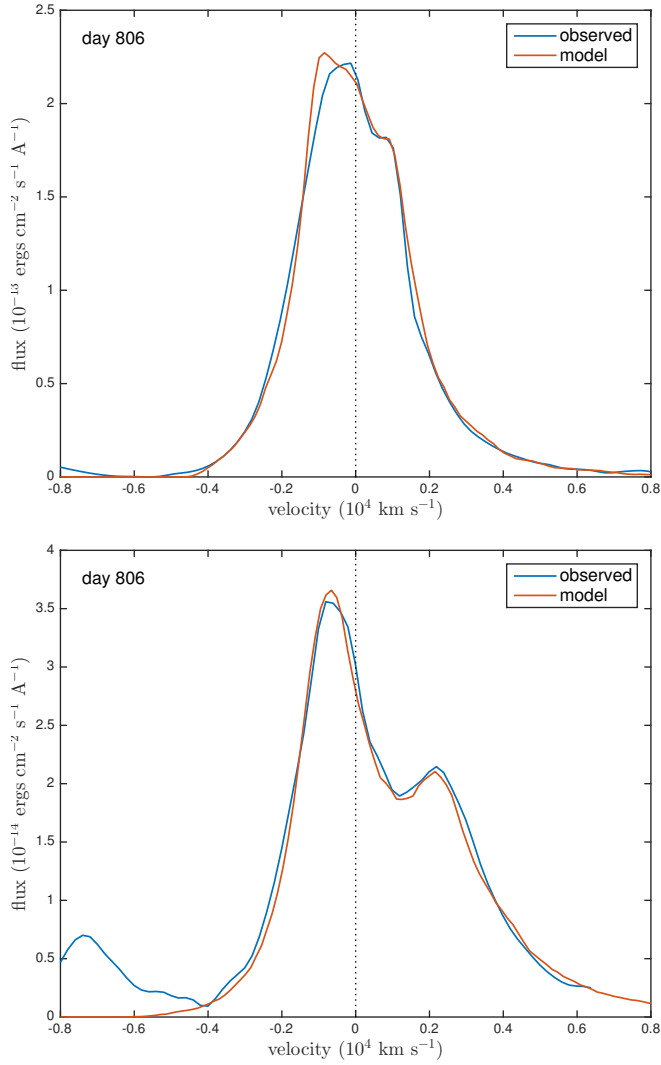


**Figure 5.3.** Best smooth fit to the day 806 H $\alpha$  line (left) and the [O I]  $\lambda 6300, 6363$  Å doublet (right) as per parameters detailed in Table 5.2.

There is rarely a unique set of parameters that best fit the data. However, the majority of the parameters of interest can be well constrained by our modelling by considering different elements of the shape of the profile. In particular, by constructing good fits to the data using both conservative and optimistic estimates of the grain size, credible lower and upper bounds on the possible dust mass formed within the ejecta may be derived. We present here reasonable fits to the data obtained using both small and large values of the grain radius  $a$ , since it is the grain size which has the most significant effect on the overall dust mass required to reproduce the profile (see Section ??). We use pure amorphous carbon dust and use the optical constants from the BE sample presented in Zubko et al.

(1996). Previous SED modelling of SN 1987A has limited the fraction of silicates present in the dusty medium to a maximum of 15% (Ercolano, Barlow & Sugerman 2007; Wesson et al. 2015). Amorphous carbon is the most conservative choice of grain type since the inclusion of even a small fraction of silicates increases the dust mass required.

For each profile, the maximum velocity is identified from the data as the point where the line vanishes on the blue side. The equivalent point on the red side is indeterminate from observations due to the effects of dust scattering. Similarly, the “corner” of the flat topped section of the profile on the blue side allows the minimum velocity at radius  $R_{in}$  to be ascertained. As discussed in Section ??, this allows the ratio of the inner and outer radii of the supernova ejecta to be determined since  $R_{in}/R_{out} = V_{min}/V_{max}$ . The outer radius is calculated from the epoch and maximum velocity.

The only parameters that then remain to be determined are the exponent of the density profile  $\beta$ , the mean grain size radius and the total dust mass. The shape of the blue wing is solely a product of the density profile and the dust mass; the height and shape of the red wing is a product of these and also of the scattering efficiency of the grains (the albedo  $\omega$ ); and the extent and shape of the asymmetry in the flat-topped portion of the profile is a result of only the total dust optical depth determined by the dust mass and the grain size. By iterating over these three parameters therefore, an excellent fit to the data can usually be obtained.

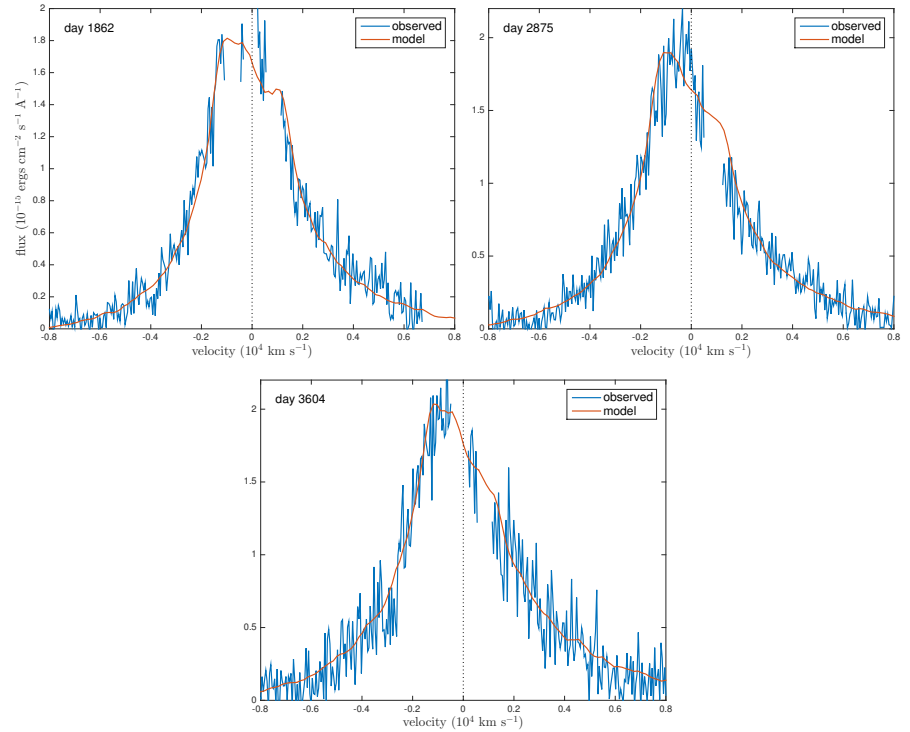
Models are produced in the same manner for the [O I]  $\lambda\lambda 6300,6363$  Å doublet as for a single line, with each component of the doublet being modelled independently and the resulting profiles added according to a specified ratio. Although the theoretical intrinsic flux ratio is 3.1 for optically thin emission, the actual ratio between the two components can be affected by self-absorption (*reference*) and we therefore left it as a free parameter. [O I]  $\lambda\lambda 6300,6363$  Å exhibits a clear blueshift as early as day 611 and provides another diagnostic for determining the dust mass. By day 1862 the doublet is no longer strong enough to usefully modelled (see Figure ??).

### 5.2.1 Smooth Density Models for SN 1987A

Even at the earliest epochs there is a substantial wing on the red of the H $\alpha$  line profile that cannot be fitted by scattering from moving grains with a small albedo. The minimum required albedo is approximately  $\omega \approx 0.5$ . The larger the grain size the larger the mass of dust required to reproduce the same optical depth (since the optical depth is dependent

**Table 5.3.** Details of the parameters used for the best fitting clumped models with  $a = 0.6\mu\text{m}$ .

	day	$V_{max}$ (km s $^{-1}$ )	$R_{in}/R_{out}$	$\beta$	$M_{dust}$ ( $M_{\odot}$ )	$a$ ( $\mu\text{m}$ )	$R_{out}$ (cm)	$R_{in}$ (cm)	doublet ratio
H $\alpha$	714	3250	0.25	1.2	7.00E-05	0.6	2.00E+16	5.01E+15	
H $\alpha$	806	4250	0.25	1.9	1.00E-04	0.6	2.96E+16	7.40E+15	
H $\alpha$	1862	8500	0.14	1.9	1.65E-03	0.6	1.37E+17	1.91E+16	
H $\alpha$	2875	9500	0.12	2	1.00E-02	0.6	2.36E+17	2.83E+16	
H $\alpha$	3604	10250	0.12	2	2.30E-02	0.6	3.19E+17	3.83E+16	
[O I]	714	5000	0.17	2.8	2.70E-04	0.6	3.08E+16	5.24E+15	2.6
[O I]	806	6000	0.15	2.7	6.00E-04	0.6	4.18E+16	6.27E+15	2.4

**Figure 5.4.** Best smooth fit to the H $\alpha$  line at days 1862, 2875 and 3604 as per parameters detailed in Table 5.2.

only on the cross-sectional area of the grains). Figure 5.1 illustrates the a fit for the day 714 H $\alpha$  profile for the case where a classical MRN grain size distribution is adopted, with  $a_{min} = 0.005\mu m$ ,  $a_{max} = 0.25\mu m$  and  $n(a) \propto a^{-3.5}$ . It can be seen clearly that the extended red wing is significantly underestimated. Since the albedo of pure amorphous carbon grains varies significantly with grain radius (see Figure 4.4) we can establish a strong lower bound to the mean dust grain radius, which we estimate to be  $a \geq 0.35\mu m$ . This is the smallest grain size that is still capable of reproducing the red scattering wing at all epochs and we therefore use this value throughout our smooth density modelling.

The ejecta inner and outer radii are calculated at each epoch from the maximum velocity used, the day number and the specified ratio  $R_{in}/R_{out}$ . The radii generated are consistent with those used in previous models of SN 1987A (Ercolano, Barlow & Sugerman 2007; Wesson et al. 2015). Figures 5.2 to 5.4 show the best fits to the data for days 714 to 3604 whilst Table 5.2 details the parameters used.

It can be seen that, in order to reproduce the blueshifts seen in the [O I]  $\lambda 6300, 6363\text{ \AA}$  doublet, considerably larger dust masses are required than to fit the H $\alpha$  line. However, larger maximum velocities are also required to fit the wings and a significantly steeper density profile is required. The inner radii remain approximately similar in both the H $\alpha$  and [O I]  $\lambda 6300, 6363\text{ \AA}$  models whilst the outer radii are significantly different. This may indicate why a greater dust mass is required in order to fit the [O I] doublet; the doublet traces the dust to a wider radius than the H $\alpha$  line.

### 5.2.2 Clumped Models for SN 1987A

It has been shown through the modelling of optical-IR SEDs that when dust is assumed to have a clumped distribution the derived masses can be significantly larger than if the dust is distributed smoothly between the inner and outer radii. We present two sets of fits to the line profile based on the clumped dust modelling of Wesson et al. (2015). Each fit is derived from the best fitting smooth model such that the photon packets are emitted assuming a smooth radial density profile. However, the dust is no longer coupled to the gas but instead is located entirely in clumps of size  $R_{out}/30$ . The clumps are distributed stochastically between  $R_{in}$  and  $R_{out}$  with the probability of a given grid cell being a clump proportional to  $r^{-\beta}$  where  $i(r) \propto r^{-2\beta}$ . The number of clumps used is determined by the clump filling factor  $f$  which is kept constant at  $f = 0.1$ . All properties are fixed from the smooth models with the exception of the grain radius and total dust mass.

**Table 5.4.** Details of the parameters used for the best fitting clumped models with  $a = 3.5\mu\text{m}$ .

day	$V_{max}$ (km s $^{-1}$ )	$R_{in}/R_{out}$	$\beta$	$M_{dust}$ ( $M_{\odot}$ )	$a$ ( $\mu\text{m}$ )	$R_{out}$ (cm)	$R_{in}$ (cm)	$\tau_{H\alpha}$	$\tau_V$	Figure
1862	8500	0.14	1.9	2.00E-02	3.50	1.37E+17	1.91E+16	0.85	1.70	5.8
2875	9500	0.12	2	8.00E-02	3.50	2.36E+17	2.83E+16	1.15	2.30	5.8
3604	10250	0.12	2	1.70E-01	3.50	3.19E+17	3.83E+16	1.33	2.67	5.8

As in the case of SED radiative transfer models, the dust masses required to reproduce the observations in the clumped case are considerably higher than for the smooth case. However, it is also necessary to have a slightly larger albedo in order to reproduce the red side of the profiles. This is because when the dust is located in clumps the radiation is subject to less scattering as well as to less absorption. The reduction in scattering appears not to be compensated for by the increased dust mass and a larger grain radius is therefore required, particularly at day 714. A grain radius of  $a = 0.6\mu\text{m}$  is therefore used throughout the clumped models as the smallest possible grain size capable of reproducing the observed profiles. Full details of all parameters used for these models may be found in Table 5.3 and the fits are presented in Figures 5.5 to 5.7.

Since these models also utilise the smallest possible grain size and therefore represent a minimum dust mass in the case of clumped distributions of amorphous carbon grains, we have also investigated the potential for this method to derive an upper bound on the dust mass. By steadily reducing the grain size from an initial value of  $5\mu\text{m}$  (motivated by the maximum possible grain size derived by W15 for their day 8515 model), we produce a set of models representing a theoretical maximal dust mass. Throughout the course of our modelling it transpired that the grain size used for the minimum models at days 714 and 806 ( $a = 0.6\mu\text{m}$ ) in fact represents the best fit to the data and even a small fluctuation in  $a$  in either direction results in a significantly poorer fit, either over- or underestimating the red wing and the trough in the doublet. We therefore conclude that the dust mass estimates produced at days 714 and 806 for a grain radius of  $a = 0.6\mu\text{m}$  are the best estimates of the dust mass at this epoch. At later epochs however we find that equally good fits may be generated by substantially larger grains, with grain radii up to  $a = 3.5\mu\text{m}$  (see Figure 5.8). Details of the parameters used in these models presented in Table 5.4.

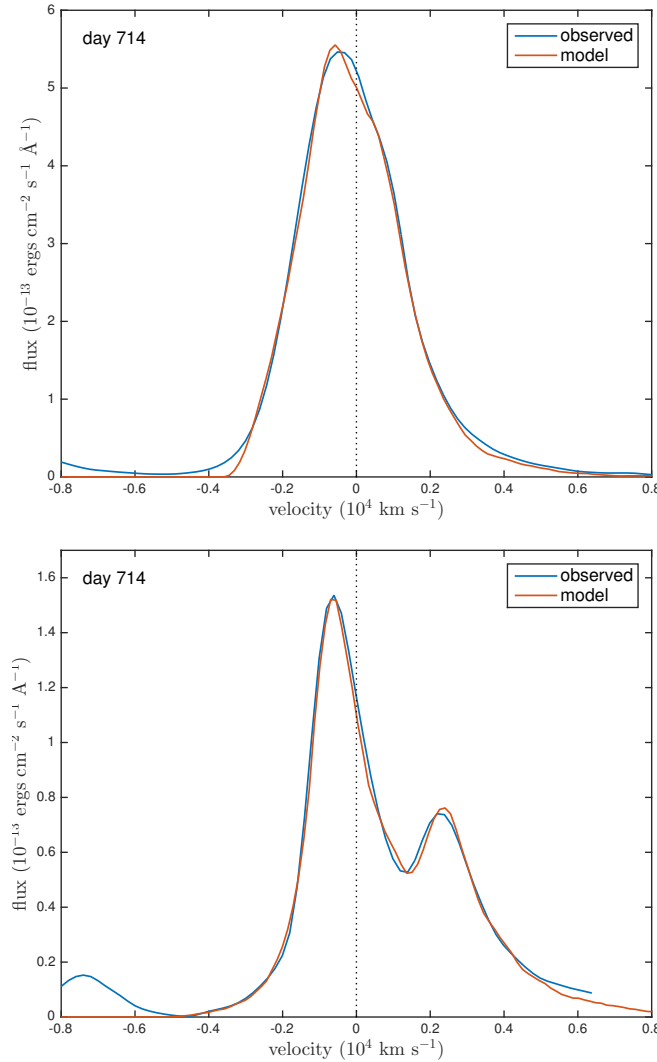


**Figure 5.5.** Best clumped fit to the day 714 H $\alpha$  line and [O I]  $\lambda 6300, 6363 \text{ \AA}$  doublet as per parameters detailed in Table 5.3.

### 5.2.3 Grain size distributions and species conversions...

We calculate the required dust masses for the clumped model on day 714 for a selection of distributions with varied  $a_{min}$ . These are presented in Table 5.5. It can be seen that in all cases, a larger dust mass is required in order to reproduce the same conditions as a single grain size. The conversion factors presented in the table are valid for any model with grain size  $a = 0.6 \mu\text{m}$  and may therefore also be applied to the models for day 806. We repeated the process for  $a = 3.5 \mu\text{m}$  but found that, in order to reproduce the required albedo, the distribution had to be heavily weighted towards the larger grains and that the value of  $a_{min}$  had no effect of the required dust mass. Increasing the value of  $a_{min}$  to larger values

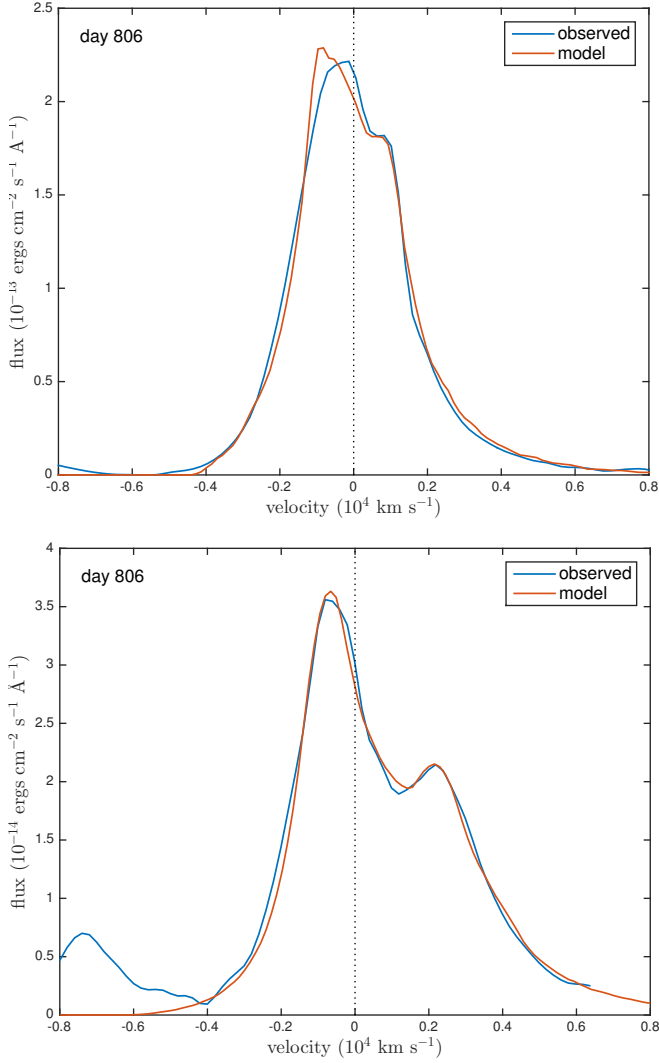


**Figure 5.6.** Best clumped fit to the day 806 H $\alpha$  line and [O I]  $\lambda$ 6300,6363  $\text{\AA}$  doublet as per parameters detailed in Table 5.3.

( $\lambda 2\mu\text{m}$ ) does not have a significant effect either. This is because both extinction efficiency and albedo tend to a constant value with increasing grain radius and the adoption of different grain size ranges and distributions above a certain threshold therefore results in only insignificant variation in these quantities.

This calculation in equation 4.7 holds only for a single wavelength and therefore is not exact for our models which obviously transport radiation over a range of wavelengths. However, the dust masses derived using the above formula produce almost identical fits to the data as for the single grain size and therefore give an excellent suggestion of the approximate dust mass required when using a distribution.

**Table 5.5.** Equivalent dust masses for the day 714 clumped models using grain size distributions and 100% amorphous carbon.  $f$  is factor of increase from the dust mass for the single size model ( $M = 7 \times 10^{-5} M_{\odot}$  with  $a = 0.6 \mu\text{m}$ ) and  $p$  is the exponent of the grain size distribution  $n(a) \propto a^{-p}$ .

$a_{min}$ ( $\mu\text{m}$ )	$a_{max}$ ( $\mu\text{m}$ )	$p$	$M$ ( $M_{\odot}$ )	$f$
0.001	4	2.45	1.93E-04	2.76
0.01	4	2.45	1.93E-04	2.76
0.05	4	2.52	1.84E-04	2.62
0.1	4	2.72	1.61E-04	2.3
0.5	4	8.2	7.23E-04	1.03

### 5.2.4 Contamination of the the H $\alpha$ profiles at days 714 and 806

The profile at day 714 (Figure 5.2) exhibits several of the features discussed above. There is an increase in flux to the red side of  $2000 \text{ km s}^{-1}$  as a result of a dust scattering reprocessing radiation to the red. There is also an approximately linear section between the peak at  $V = -420 \text{ km s}^{-1}$  and the very slight corner visible at  $V_{min}$ . The profile at day 806 (Figure 5.3) has similarly identifiable features with a noticeable wing on the red side extending out to nearly  $V = 8000 \text{ km s}^{-1}$ . It also exhibits a definite shoulder reaching to  $V \approx 900 \text{ km s}^{-1}$  which we assume to be the value of  $V_{min}$ . In both these cases, with both smooth and clumped models, we struggle slightly to fit both the corner and the peak of the profile. In both instances, accurately fitting the corner results in a peak that is slightly further towards the blue than is seen in the observations. We suggest that this discrepancy, which is more noticeable at day 806 because of the more distinctive shape of the profile, is likely a result of the increased flux produced by a clump at  $V = -360 \text{ km s}^{-1}$ . This clump, clearly visible in the line profile at day 673 and identified as such in the literature (?Hanuschik et al. 1993), is likely contaminating the position of the peaks of the profiles at days 714 and 806. The clump is perhaps not so clearly discernible at these epochs as a result of the poor resolution of the CTIO spectra but is known to have persisted until around day 900 (Hanuschik et al. 1993).

### 5.2.5 The red shoulder in the H $\alpha$ line profile at day 806

The shoulder in the H $\alpha$  line profile at day 806 has previously been attributed to an unresolved [NII]  $\lambda 6583 \text{ \AA}$  line at  $V = 933 \text{ km s}^{-1}$  (?). Narrow [N II] lines at  $\lambda = 6583 \text{ \AA}$

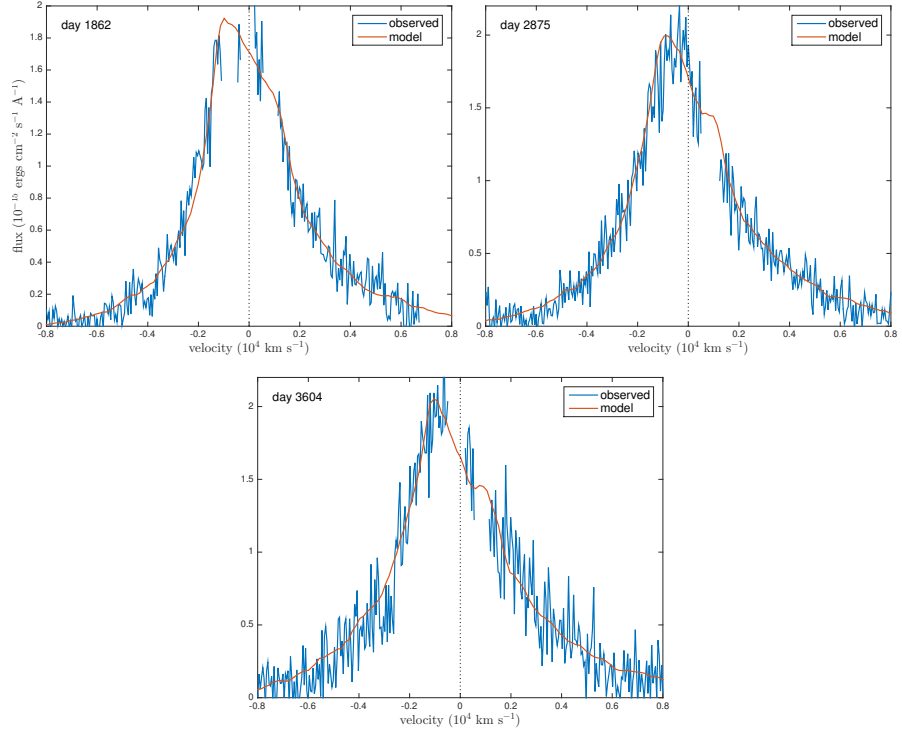


**Figure 5.7.** Best clumped fit to the H $\alpha$  line at days 1862, 2875 and 3604 as per parameters detailed in Table 5.3 with  $a = 0.6\mu\text{m}$ .

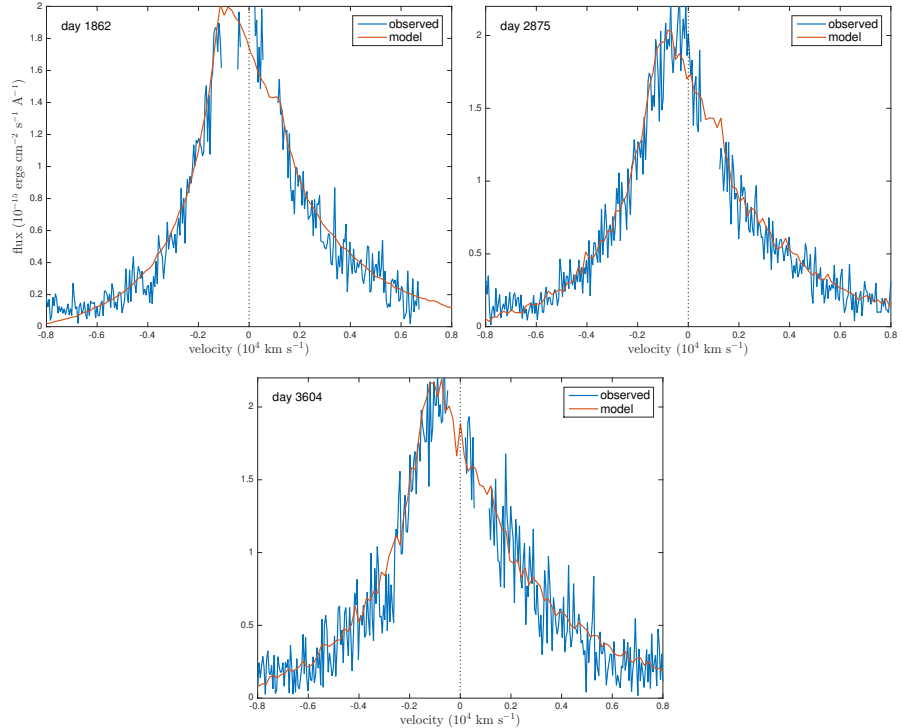


**Figure 5.8.** Best clumped fit to the H $\alpha$  line at days 1862, 2875 and 3604 as per parameters detailed in Table 5.4 with  $a = 3.5\mu\text{m}$ .

and  $\lambda = 6548 \text{ \AA}$  either side of the H $\alpha$  rest frame velocity at  $6563 \text{ \AA}$  are certainly seen by day 1862 and have to be removed in order to consider the evolution of the broad H $\alpha$  profile. It is somewhat unfortunate that the theoretical minimum velocity falls at a similar velocity to this line as it makes it difficult to distinguish the two features. We postulate however that this feature may in fact be a product of a relatively steep density profile and the formation of dust within the ejecta as demonstrated in both our fits (see Figures 5.3 and 5.6) and our investigation of the parameter space (see Figures 4.1 and 4.2).

It is a general challenge inherent in the nature of this modelling that interesting features that are present in line profiles are not necessarily easily identifiable. In particular, the effects of clumping and asymmetrical distributions in the ejecta may cause fluctuations that are hard to distinguish from the potential signatures of dust formation discussed in Section ???. Key indicators such as symmetry in the location of discontinuities on the red and blue side, typical dust profile signatures and the presence of a red scattering wing should be considered.

### 5.2.6 Potential challenges at later epochs: days 1862, 2875 and 3604

At later epochs, even very tiny fluctuations in adopted value of the continuum level can have a substantial effect on the fit of the resulting profile. Since it is not feasible to establish the level of the continuum so precisely, the value of the continuum has been left as a free parameter that may be adjusted (to within sensible margins) in order to allow for the widest possible dust mass range to be determined. We generally find it is necessary to assume a continuum level that is slightly lower where the adopted dust mass is higher.

The line profiles at these later epochs are relatively noisy and have had substantial sections of the profile removed as a result of contamination by the H $\alpha$  and [NII] narrow lines. Unfortunately, this removes a critical section of the line ( $500 \text{ km s}^{-1} < v < 1500 \text{ km s}^{-1}$ ) that would be potentially informative about  $V_{min}$ . However, we do achieve good fits to the line profiles at these epochs.

## 5.3 The evolution of dust formation in SN 1987A

We have collated a range of archival spectral data in the optical and IR and, by modelling the evolution of the H $\alpha$  and [O I]  $\lambda 6300, 6363 \text{ \AA}$  lines, have placed constraints on the evolution of newly formed dust in SN 1987A. We have done this using Monte Carlo models

that consider both the absorbing and scattering effects of dust. We find dust masses that are in good agreement with those previously found at similar epochs. We obtain large dust masses at just a few thousand days in agreement with the very large mass of dust deduced by from their observations at long wavelengths using Herschel (Matsuura et al. 2011). We compare our dust masses directly with those obtained by W15 and by ? in order to compare both their magnitude and evolution (see Figure 5.9).

### 5.3.1 Dust masses from other line profile models

? analysed the [O I] $\lambda 6300$  Å line for SN 1987A and found optical depths for a range of epochs. They translated these into dust masses for day 775 only. For our smooth modelling of [O I] we obtain  $\tau_V = 2.19$  at day 714 and  $\tau_V = 1.95$  at day 806. These values are somewhat higher than the values given by ? at similar epochs. At day 725, they cited a value of  $\tau_V = 1.19$  and at day 775 a value of  $\tau_V = 1.25$ . The primary reason for the discrepancy in these values is the assumed albedo. ? considered line profiles before and after dust condensation and concluded that any evidence of an extended red scattering wing was unconvincing. Accordingly, they adopted a model with perfectly absorbing dust ( $\omega = 0$ ). For our amorphous carbon models of [O I] $\lambda 6300, 6363$  Å with grain radius  $a = 0.35\mu\text{m}$ , we obtain an albedo of approximately  $\omega = 0.5$  at  $\lambda = 6300$  Å. The total optical depth to absorption is therefore very similar comparing our model at day 714 to their results at day 725. There is slightly more discrepancy between our model at day 806 and their model at day 775.

However, ? noted that the dust optical depth increased rapidly after day 580 and then the rate of increase of the dust optical depth appeared to slow after day 670. Our results, for both clumped and smooth models, suggest that the dust optical depth actually drops between day 714 and day 806 before starting to increase again at later epochs. This is consistent with the results of ? where the slowing rate of increase of dust optical depth could imply an impending turning point subsequent to day 775. If a turnover did in fact occur at this time then it could explain the difference in our values.

Finally, the dust masses derived by ? at day 775 ( $M_{dust} = 4.4 \times 10^{-6} M_\odot$  for amorphous carbon) are significantly different to those obtained from our smooth modelling of the [O I] $\lambda 6300, 6363$  Å doublet at day 806 ( $M_{dust} = 1.6 \times 10^{-4} M_\odot$  for amorphous carbon). There are three main reasons for the discrepancy. Firstly, the albedo is significantly larger in our modelling as already discussed so a larger dust mass is required to produce the same

amount of absorption. Secondly, the grain size is considerably larger which reduces the total cross-section of interaction, and finally, the adopted maximum velocity ( $6000 \text{ km s}^{-1}$ ) in our model is larger than the value adopted by ? ( $1870 \text{ km s}^{-1}$ ). This increases the total volume of the ejecta significantly and therefore significantly more dust is required to produce the same optical depth.

### 5.3.2 Dust masses and properties from SED models

Considering now the results of W15, we find that at all epochs we obtain slightly smaller dust masses than those of W15 although our values are still generally within the error bars placed on their values. There may be a number of different reasons for this. Firstly, our modelling is somewhat more conservative in its estimates since we use amorphous carbon whereas the models presented by W15 use a silicate fraction of 15% which is likely to increase the overall mass of dust required to produce the same observations, both in the case of radiative transfer SED modelling and line profile modelling. Secondly, we use different sets of optical constants; we have used the optical constants derived by Zubko et al. (1996) from their BE sample where W15 use constants from Hanner (1988). They state that in order to fit their data at early epochs (day 615) with the Zubko ACH2 sample smaller inner and outer radii are needed and half as much dust ( $5.0 \times 10^{-4} M_{\odot}$ ) is required. This is considerably closer to the values we derive at similar epochs.

The other significant difference between our models is the adopted grain size distribution. W15 generate fits to their ealy data using an MRN distribution between  $0.005 \mu\text{m}$  and  $0.25 \mu\text{m}$  in size. They cannot obtain a fit with grains of  $\sim 1.0 \mu\text{m}$  in size at early epochs. However, they do not consider values in between these size point as we conclude is likely the case with grain sizes of  $a \approx 0.6 \mu\text{m}$ . For SED modelling it is generally the case that the larger the grain size used, the less dust is required to produce the same level of flux and it may therefore be this difference that is generating the discrepancy in our results. W15 use this property to derive a maximum possible grain size at late epochs as well and conclude that grains cannot be larger than  $\sim 5 \mu\text{m}$  by day 8515. This is directly in line with the maximum grain sizes we derive at slightly earlier epochs. We find that the grain size likely cannot have exceeded  $\sim 3.5 \mu\text{m}$  at day 3604 and the dust masses that we generate using this value are very similar to the value of the W15 sigmoid fit at this epoch.

Determining the relationship between the size of dust grains in the ejecta and the

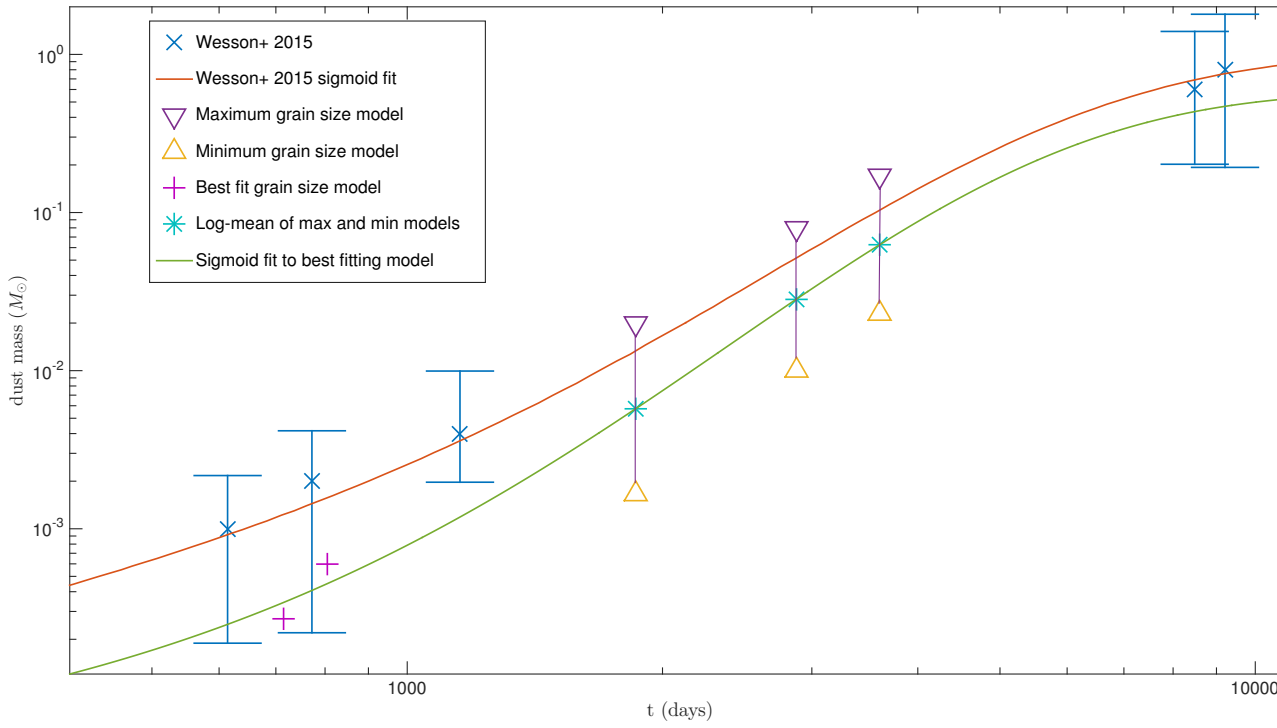


**Figure 5.9.** Purple and yellow triangles - Maximum ( $a = 3.5\mu\text{m}$ ) and minimum ( $a = 0.6\mu\text{m}$ ) dust masses respectively. Values are from the later epoch ( $t > 1862$  days) clumped models of H $\alpha$ . Pink crosses - Predicted dust masses (clumped models of the [O I]  $\lambda 6300, 6363$  Å doublet with grain size  $a = 0.6\mu\text{m}$ ). Turquoise stars - Predicted dust masses calculated as a log average of the maximum and minimum values. Green - Sigmoid fit to our predicted dust masses. Blue - dust masses derived by W15 in their photometric modelling of SN 1987A. Red - sigmoid fit to the W15 values.

time post-explosion is important for understanding the likelihood of dust surviving the passage of the reverse shock travelling back through the ejecta. By the time the reverse shock begins to appear in the line profiles (around day 5000), our models predict that the grains could already be as large as several microns in radius but are certainly larger than  $\sim 0.6\mu\text{m}$ . Grains larger than  $\sim 0.2\mu\text{m}$  are likely to survive and thus the majority of the dust produced is likely to survive (remembering that our modelling only considers an average grain size and makes no comment about the grain size distribution). It has recently been suggested that very large grains (up to  $4.2\mu\text{m}$ ) may have formed in the ejecta of SN 2010jl very soon after the explosion (a few hundred days) Gall et al. (2014). Whilst the values we suggest are not as high that postulated by Gall et al. (2014), they maintain a distribution that remains steeped towards the smaller end of the scale and

thus, as our models only treat a single, average grain size, these values may not be at odds. Certainly, both results suggest that grains large enough to survive the destructive force of the reverse shock have formed by a few hundred days post-explosion.

There is now a firm consensus that a very large quantity of dust has formed in SN 1987A between the time of the original explosion and the present day. Perhaps more important therefore is the manner of its evolution. We have shown that dust masses have reached the order of  $0.1M_{\odot}$  by day 3604. However, it is known that values several times as large as this are ultimately expected and thus a substantial fraction of the dust is likely to form after this epoch. This is in strong agreement with the results produced by W15. They derive a sigmoid fit to their dust mass evolution of the form

$$M_d(t) = ae^{be^{ct}} \quad (5.1)$$

where they obtain values of  $a = 1.0M_{\odot}$  (representing the maximum dust mass),  $b = -8.53$  and  $c = -0.000366$ . Both their dust masses and this sigmoid fit are shown in Figure 5.9. This exhibits an initial period of slow growth followed by an intermediary period of acceleration followed by another slowing until a plateau is ultimately reached. In this sense it may be relatively representative of the process of dust formation whereby initial conditions appropriate for grain growth gradually develop until optimal conditions are reached at an intermediate epoch when grain growth is at its fastest before conditions once again deteriorate and the rate slows again (as discussed by W15). Performing a least-squares regression to this function using our predicted dust masses, we derive a sigmoid fit with coefficients  $a = 0.58M_{\odot}$ ,  $b = -10.02$  and  $c = -0.000416$ . These values are remarkably similar to those derived by W15 although the final predicted dust mass is slightly smaller in our case. This sigmoid fit is also plotted in Figure 5.9.

Our modelling concurs with the suggestion of W15 that even after  $\sim 3000$  days the dust mass is only a very small fraction of its final value. This is in contrast to Sarangi & Cherchneff (2015) whose chemistry models predict that the evolution of dust formation will have reached its plateau by around 5 years after the explosion first occurred.

Ideally, our models would cover the entire evolution of SN 1987A right up to the present day. However, the excitation of gas in the outer edges of the ejecta by the reverse shock after  $\sim$  day 500 results in a significant, broad and asymmetric flux that dominates the

original line profile. In addition to this, the narrow lines from the ring start to become so significant relative to the original broad H $\alpha$  profile that, post-removal, there is not enough of the broad profile remaining to be able reliably infer information from its features. These are factors that are likely to be common to most core collapse supernovae and thus are likely to have an impact on the wider applicability of this particular technique at later epochs. Care should also be taken in the future to ensure that the line profiles are the temporally appropriate profile and not in fact a product of a light echo representing the state of the ejecta at some previous epoch. Nonetheless, this technique has proved effective in determining dust masses formed in core-collapse supernovae through the detailed modelling of asymmetric line profiles and clearly has wider application to multiple supernovae and supernova remnants.

This page was intentionally left blank

## Chapter 6

---

### SN 2010jl and Other Supernovae

*QUOTE GOES HERE*

AUTHOR

FIRST PARAGRAPH

THE REST FOLLOW HERE.

This page was intentionally left blank

## Chapter 7

---

### Conclusions and Future Work

*QUOTE GOES HERE*

AUTHOR

FIRST PARAGRAPH

THE REST FOLLOW HERE.

This page was intentionally left blank

# Bibliography

- Andrews J. E. et al., 2010, ApJ, 715, 541
- Barlow M. J. et al., 2010, A&A, 518, L138
- Bertoldi F., Carilli C. L., Cox P., Fan X., Strauss M. a., Beelen A., Omont A., Zylka R., 2003, A&A, 406, L55
- Cernuschi F., Marsicano F., Codina S., 1967, Annales d'Astrophysique, 30, 1039
- Cherchneff I., Dwek E., 2009, ApJ, 703, 642
- Cherchneff I., Dwek E., 2010, ApJ, 713, 1
- Chugai N. N., Chevalier R. a., Kirshner R. P., Challis P. M., 1997, ApJ, 483, 925
- Draine B. T., Lee H. M., 1984, ApJ, 285, 89
- Dwek E., Galliano F., Jones A. P., 2007, ApJ, 662, 927
- Ercolano B., Barlow M. J., Sugerman B. E. K., 2007, MNRAS, 375, 753
- Fabbri J. et al., 2011, MNRAS, 418, 1285
- Fransson C. et al., 2013, ApJ, 768, 88
- Gall C. et al., 2014, Nature, 511, 326
- Gerasimovic B., 1933, Zeitschrift für Astrophysik, 7, 335
- Gomez H. L. et al., 2012, MNRAS, 420, 3557
- Gröningsson P. et al., 2008, A&A, 479, 761
- Gröningsson P. et al., 2007, A&A, 491, 19

- Grönningsson P., Fransson C., Lundqvist P., Nymark T., Lundqvist N., Chevalier R., Leibundgut B., Spyromilio J., 2006, A&A, 5325, 11
- Hanner M. S., 1988, NASA Conf. Publ., 3004, 22, NASA, Washington DC
- Hanuschik R. W., Spyromilio J., Stathakis R., Kimeswenger S., Gohermann J., Seidensticker K. J., Meurer G., 1993, MNRAS, 261, 909
- Hillier D. J., 1991, A&A, 247, 455
- Hoyle F., Wickramasinghe N. C., 1970, Nature, 226, 62
- Kotak R. et al., 2009, ApJ, 704, 306
- Kozasa T., Hasegawa H., Nomoto K., 1989, ApJ, 344, 325
- Kozasa T., Hasegawa H., Nomoto K., 1991, Formation of dust grains in the ejecta of SN 1987A
- Li A., Greenberg J. M., 2003, in Solid State Astrochemistry, Pirronello V., Krelowski J., Manicò G., eds., pp. 37–84
- Lucy L., Danziger I., Gouiffes C., Bouchet P., 1989, in IAU Colloq. 120: Structure and Dynamics of the Interstellar Medium, Lecture Notes in Physics, Tenorio-Tagle G., Moles M., Melnick J., eds. No. 350, Berlin Springer Verlag, p. 164
- Mathis J. S., Rumpl W., Nordsieck K. H., 1977, ApJ, 217, 425
- Matsuura M. et al., 2011, , 333, 1258
- Meikle W. P. S. et al., 2007, ApJ, 665, 608
- Morgan H. L., Edmunds M. G., 2003, MNRAS, 343, 427
- Nozawa T., Kozasa T., Umeda H., Maeda K., Nomoto K., 2003, ApJ, 598, 785
- Omont A., Cox P., Bertoldi F., McMahon R. G., Carilli C., Isaak K. G., 2001, A&A, 374, 371
- Owen P. J., Barlow M. J., 2015, ApJ, 801, 141

- Phillips M. M., Hamuy M., Heathcote S. R., Suntzeff N. B., Kirhakos S., 1990, An optical spectrophotometric atlas of supernova 1987A in the LMC. II - CCD observations from day 198 to 805
- Sarangi A., Cherchneff I., 2013, ApJ, 776, 107
- Sarangi A., Cherchneff I., 2015, Astronomy & Astrophysics, 575, A95
- Schneider R., Ferrara A., Salvaterra R., 2004, MNRAS, 351, 1379
- Smith N., Silverman J. M., Filippenko A. V., Cooper M. C., Matheson T., Bian F., Weiner B. J., Comerford J. M., 2012, AJ, 17, 6
- Spyromilio J., Stathakis R., Cannon R., Waterman L., Couch W., Dopita M., 1991, MNRAS, 248, 465
- Sugerman B. E. K. et al., 2006, , 313, 196
- Todini P., Ferrara A., 2001, MNRAS, 325, 726
- Trumpler R. J., 1930, PASP, 42, 214
- Tziampzis a., Lundqvist P., Groningsson P., Nasoudi-Shoar S., 2010, A&A, 515, 15
- Wang L. et al., 1996, ApJ, 466, 998
- Watson D., Christensen L., Knudsen K. K., Richard J., Gallazzi A., Michaowski M. J., 2015, Nature, 519, 327
- Wesson R., Barlow M. J., Matsuura M., Ercolano B., 2015, MNRAS, 446, 2089 (W15)
- Zubko V. G., Mennella V., Colangeli L., Bussoletti E., 1996, MNRAS, 282, L1321



*“YOUR QUOTE GOES HERE”*

AUTHOR OF QUOTE

